

VARIABLE PATHLENGTH CAVITY SPECTROSCOPY

DEVELOPMENT OF AN AUTOMATED PROTOTYPE

by

Ryan Andrew Schmeling

A Dissertation Submitted in
Partial Fulfillment of the
Requirements for the Degree of

Doctor of Philosophy
in Chemistry

at

The University of Wisconsin-Milwaukee

May 2016

ABSTRACT

VARIABLE PATHLENGTH CAVITY SPECTROSCOPY DEVELOPMENT OF AN AUTOMATED PROTOTYPE

by

Ryan Andrew Schmeling

The University of Wisconsin-Milwaukee, 2016
Under the Supervision of Professor Joseph H. Aldstadt III

Spectroscopy is the study of the interaction of electromagnetic radiation (EMR) with matter to probe the chemical and physical properties of atoms and molecules. The primary types of analytical spectroscopy are absorption, emission, and scattering methods. Absorption spectroscopy can quantitatively determine the chemical concentration of a given species in a sample by the relationship described by Beer's Law. Upon inspection of Beer's Law, it becomes apparent that for a given analyte concentration, the only experimental variable is the pathlength. Over the past ~75 years, several approaches to physically increasing the pathlength have been reported in the literature. These have included not only larger cuvettes and novel techniques such as Differential Optical Absorption Spectroscopy, but also numerous designs that are based upon the creation of an optical cavity in which multiple reflections through the sample are made possible. The cavity-based designs range from the White Cell (1942) to Cavity Ring-Down Spectroscopy (O'Keefe and Deacon, 1998). In the White Cell approach, the incident beam is directed off-axis to repeatedly reflect concave mirror surfaces. Numerous variations of the White Cell design have been reported, and it has found wide application in infrared absorption spectroscopy in what have become to be known as "light pipes". In the CRDS design, on the other hand, highly reflective dielectric mirrors situated for on-axis reflections result in

the measurement of the exponential decay of trapped light that passes through the exit mirror. CRDS has proven over the past two decades to be a powerful technique for ultra-trace analysis ($< 10^{-15}$ g), with practical applications ranging from atmospheric monitoring of greenhouse gases to biomedical “breath screening” as a means to identify disease states.

In this thesis, a novel approach to ultra-trace analysis by absorption spectroscopy is described. In this approach known as Variable Pathlength Cavity Spectroscopy (VPCS), a high finesse optical cavity is created by two flat, parallel, dielectric mirrors — one of which is rotating. Source light from a pulsed dye laser (488 nm) enters the optical cavity in the same manner as in Cavity Ring-Down Spectroscopy (CRDS), i.e., by passing through the cavity entrance mirror. However, unlike CRDS in which the mirrors are fixed, concave, and mechanically unaltered, the cavity exit mirror contains a slit (1.0 mm diameter) that is rotated at high speed on an axle, thereby transmitting a small fraction of the trapped light to a photomultiplier tube detector. In this approach, unlike CRDS, absorbance is measured directly. In previous prototype designs of the VPCS instrument, instrument control (alignment) and data acquisition and reduction were performed manually; these functions were both inefficient and tedious.

Despite this, the VPCS was validated in “proof of concept” testing, as described with a previous prototype (Frost, 2011). Frost demonstrated that the pathlength enhancement increased 53-fold compared to single-pass absorption measurements in monitoring NO_2 (g) at part-per-billion levels. The goal of the present work is to improve upon the previous prototype (“P4”) that required manual alignment, data collection, and data reduction by creating a completely automated version of VPCS — i.e., the “P5” prototype. By developing source code in

LabVIEW™, demonstration that the VPCS can be completely controlled in an automated fashion is described. Computationally, a Field-Programmable Gate Array is used to automate the process of data collection and reduction in real-time. It is shown that the inputs and outputs of the P5 instrument can be continuously monitored, allowing for real-time triggering of the source laser, collection of all data, and reduction of the data to report absorbance.

Furthermore, it is shown that the VPCS can be automatically aligned — also in real-time on the order of microseconds — to a high degree of precision by using servo-actuators that adjust the beam position based upon the input from a sensitive CCD camera. With the implementation of this hardware and LabVIEW code, more precise data collection and reduction is done. With this new fully automated design, the instrument characteristics (e.g., to include factors such as rotation speed, off-set angle, and pathlength variation) can improve the enhancement by ~130-fold vs. single-pass absorption measurements.

© Copyright by Ryan Andrew Schmeling, 2016
All Rights Reserved.

TABLE OF CONTENTS

1. Absorption Spectroscopy.....	1
LITERATURE CITED	18
2. Variable Pathlength Cavity Spectroscopy	21
LITERATURE CITED	48
3. Experimental.....	49
Literature Cited.....	59
4. Results and Discussion.....	60
LITERATURE CITED	122
5. Future Work.....	123
LITERATURE CITED	132
CURRICULUM VITAE.....	133

LIST OF FIGURES

Figure 1-1. The absorption process. Radiation of incident radiant power P_0 can be absorbed by the analyte, resulting in a transmitted beam of lower power (P). For absorption to occur, the energy of the incident beam must correspond to one of the energy differences shown in (b). The resulting spectrum is shown in (c). Figure taken from Reference 1.....	2
Figure 1-2 The basic experimental setup in molecular absorption spectroscopy.....	4
Figure 1-3. DOAS systems can be either active or passive depending on the source of radiation used. Image taken from Reference 4.	7
Figure 1-4. A typical response in DOAS. The absolute incident intensity (I_0) is not of importance, primarily because of the scattering losses that occur. (I_0') is interpolated from the intensity that is observed on either side of the narrow absorption line of the species. Image taken from Reference 4.	8
Figure 1-5. Schematic diagram of the White Cell. The distance from mirror A/A' to mirror B is equal to their radius of curvature as a means to establish conjugate foci on the surface of the mirrors. Image taken from Reference 14.....	10
Figure 1-6. An example of the order of the spots position on the mirror. Image taken from Reference 17.	11
Figure 1-7. Cross section of the optical cavity showing the “perturber mirror” position. Image taken from Reference 17.....	12
Figure 1-8. Illustration of sputter-coated layers of alternating refractive indices with an incident light striking the mirror and Fresnel reflections occurring at the point where the refractive index changes. (Diagram compliments of Dr. Paul Henning)	13
Figure 1-9. CRDS response showing the observed detector response (thin pulsing line), and the fitted decay curve. Image taken from Reference 19.....	15
Figure 1-10. Experimental set-up for cavity ring-down absorption spectroscopy. The sample is contained in the cavity with length L and mirror reflectivity R . Image taken from Reference 21.	16
Figure 1-11. Schematic diagram of the Brewster's-angle flow cell. The refractive index is 1.46 for fused silica and 1.33 for water, the optimal wedge angle, e , is 7.9° . With this configuration the cell should be tilted so that the angle of light incidence, a , is 55.6° . The light refracts through the cell, hitting each surface at the appropriate angle for minimum reflection. These Brewster’s angles are $b = 34.4^\circ$, $c = 42.3^\circ$, and $d = 47.7^\circ$. Image taken from figure 37.....	17
Figure 2-1. Schematic representation of the design of the variable pathlength cavity spectrometer beam path using a cw source and a rotating entrance and exit mirror. The four mirrors used to create the delay loop inside the cavity have been omitted for clarity. Image taken from Reference 1.	22

Figure 2-2. Schematic representation of the rotating mirror. Angle θ is defined as the angle between the center of the projected beam spot and the leading edge of the exit slit. It should be noted that while two slits are necessary for mirror balance, only one is utilized for the measurement. Image taken from Reference 2. 24

Figure 2-3. Theoretical relationship between the light transmittance (T) and the pathlength enhancement (b^*) that could be realized at an angular offset of 15 degrees and a physical pathlength of 0.01 m. Image taken from Reference 1..... 27

Figure 2-4. Original dielectric mirror specifications for the P1 VPCS. 29

Figure 2-5 Axle and mount assembly of the P1 prototype. A (axle), M (mirror), MB (mount base), N (nut), NW (neoprene washer), P (brass drive pulley), SW (steel washer). Image taken from Reference 1..... 30

Figure 2-6. P1 VPCS optical layout. DM (drive motor), F (filter), M (mirror), PMT (photomultiplier tube), RM (rotating mirror), S (source). Image taken from Reference 1..... 31

Figure 2-7. P2 VPCS optical layout. DM (drive motor), F (filter), M (mirror), PMT (photomultiplier tube), RM (rotating mirror), S (source). Image taken from Reference 1..... 32

Figure 2-8. Specification for the hubs used for aligning the rotating mirrors. Three set-screws were used to hold the Delrin hubs against the axle. The other three set-screws were nylon-tipped because they were in contact with the mirrored surfaces. Image taken from Reference 1..... 33

Figure 2-9 The P2 axle mount assemble. The unsupported axle, the weak “L-shaped” axle mounts, and the drive band not being separated from the mirrors lead to observable vibrations. Image taken from Reference 1..... 35

Figure 2-10 Schematic diagram of the assembly of the P3 prototype axle mount from the side view (top) and end view (bottom). A (axle), BH (bearing hole), DAH (Delrin alignment hub), MB (mount base), M (mirror), MB (mirror bushing), N (nut), NW (neoprene washer), P (brass drive pulley), SH (source hole), SW (steel washer). Image taken from Reference 1..... 36

Figure 2-11 Ray diagram of the optical cavity using flat steering mirrors. If only flat mirrors were used the beam quickly "walked out" of the cavity. Image taken from Reference 1..... 37

Figure 2-12 Ray diagram of the optical cavity using concave (ROC = 1 m) steering mirrors. The divergence of the beam within the cavity was negligible. Image taken from Reference 1..... 38

Figure 2-13. Electron micrograph of a slit in a dielectric mirror (30-fold magnification). Image taken from Reference 1..... 39

Figure 2-14. Schematic diagram of the P4 prototype. CM (concave mirror), DG (delay generator), EM (entrance mirror), G (diffraction grating), M (mirror), OS

(oscilloscope), PD (photodiode), D (photomultiplier tube), PS (processed signal), RM (rotating mirror), RS (raw signal). Image taken from Reference 1.....	40
Figure 2-15 The dependence of the cavity transmittance on the angular off-set. Negative values are those in which the exit slit has already passed the beam position and no trapping is possible. Image taken from Reference 1.	41
Figure 2-16. VPCS response profiles at 10 (▪) and 15 (•) krpm showing the shifting of the curves to higher angular off-sets. Image taken from Reference 1.....	43
Figure 2-17 Photograph of the gas introduction jet. The NO _{2(g)} entered from the top of the jet and the sweep gas (air) entered from the tube protruding from the side. The NO _{2(g)} passed through the optical path of the VPCS and then was collected by the white funnel positioned under the beam path (which was under a slight vacuum). Image taken from Reference 1.....	44
Figure 2-18 Transmittance at 488 nm of the P4 prototype VPCS response with and without NO _{2(g)} present as a function of angular off-set. Data was collected as a constant rotational speed of 10 krpm.....	45
Figure 2-19 An example of the VPCS absorption as a function of angular off-set calculated from the fitted regression curve at 10 and 15 krpm.....	46
Figure 2-20 Enhancement factor as a function of increasing rotational speed and angular off-sets.....	47
Figure 3-1. Schematic diagram of the Nitrogen Dioxide generator. The VPCS is depicted at left (M = fixed flat mirror, RM = rotating mirror, CM = fixed concave mirror, PMT = photomultiplier tube detector).	50
Figure 3-2. Schematic diagram of the Agilent Photodiode Array Spectrophotometer. Diagram taken from Reference 2.....	51
Figure 3-3. Optical performance of the CCD camera. Image taken from Reference 8.....	58
Figure 4-1 Description of oscilloscope channel signals and the selection of the data points relevant to the calculations. Image taken from Reference 1.....	64
Figure 4-2 Example of a PXIe system with the PXIe NI-1071 chassis. Image taken from National Instruments.	70
Figure 4-3 Hardware-level processing allows for high amounts of reliability as well as low response times versus trying to carry out the same functionality through an operating system. ³ With FPGA there are not the layers of software that the code and data travels through so there is much faster processing. Image taken from National Instruments.....	71
Figure 4-4 The different parts of an FPGA ³ with the center of the image being the FPGA chip, the other three main components are illustrated as to their location and interaction with each other. Image taken from National Instruments.	72
Figure 4-5 NI PXIe-7965R. Image taken from National Instruments.	73

Figure 4-6 NI 5761 Adapter Module used in prototype 5. Image taken from National Instruments.	74
Figure 4-7 Electrical schematic for voltage buffer built to increase the CMOS signal to trigger the Nitrogen laser.	75
Figure 4-8 Diagram of P5 instrument. (EG, Grating; EM, Entrance Mirror; CM 1, Concave Mirror 1; CM 2, Concave Mirror 2; RM, Rotating Mirror; PMT, Photomultiplier Tube Detector; PD, Photodiode Detector; Cam, Allied Technologies Camera; 532 nm, CW Alignment Laser; Secondary Laser, 633 HeNe) Initially the camera was placed behind CM-1, however inadequate images were obtained so the current design was implemented with the camera locate behind CM 2 to image CM 1. CM 2 has the piezoelectric motors attached to the mount.	78
Figure 4-9 Image of CM-1 face with the LED's off (left) as they would be during a measurement, and on (right) as they would be during the automated alignment process.	79
Figure 4-10 Example of an image taken by the Allied Technologies camera; this image is processed through an algorithm to triangulate the center of the mirror.	80
Figure 4-11 The images were captured by Allied Technologies camera. This is a comparison of the aligned (left image) vs. misaligned (right). Two spots are observed as one is the incident light and the second spot is the light returning to the entrance Mirror	81
Figure 4-12 Step 1 of the alignment process involves locating the LED's and overlaying the crosshairs based on the midpoints between the points.	82
Figure 4-13 Step 2 of the alignment process is to locate the incident beam and confirm that it is striking the center of the mirror.	83
Figure 4-14 Step 3 of the alignment process is locating the position of the reflected beam after making a pass through the cavity, striking the rotating mirror, and returning to the entrance mirror.	84
Figure 4-15 The operator can adjust the position of CM 2 by pressing the "Jog" arrow or by double-clicking the position and inputting a value for a smaller adjustment.	85
Figure 4-16 Updated image of the new position of the beam based on the adjustments made to the vertical position change. If the operator selects "Yes", the VI proceeds to aligning the horizontal position; if "No" is selected the control menu is displayed to continue adjusting the vertical position.....	86
Figure 4-17 An example VI showing the block diagram (left) and front panel (right) for the addition and subtraction of X and Y.....	88
Figure 4-18 While Loop structure. The loop will continuously run until the Boolean value (right, "stop if true" icon) is met. The box (left) with the "i" is number of iterations.	89
Figure 4-19 The While Loop will run continuously perform the data reduction until the stop button is clicked on the front panel.	90

Figure 4-20 For Loop executes n iterations, where n is wired to the input on the upper left hand corner.	91
Figure 4-21 A for loop used to increment an input value "x" by "y", for 10 iterations. The result of the loop is stored on the shift register to be used for the mathematical operation in the subsequent iteration.....	92
Figure 4-22 Sequence structure controls the order in which subdiagrams occur, starting on the left and working toward the right.	93
Figure 4-23 Example of the use of a sequence structure. This controls the order in which the subdiagrams will execute. Once all data is at the terminals then the second frame can execute.....	94
Figure 4-24 Case structure, with the true case showing. The selector terminal is the question mark (?) on the left side of the structure and is used to select the case that will be executed.	94
Figure 4-25 Case structure where the input to the selector terminal is true, causing the true case to be executed and lighting up the "Greater Than 0" Boolean on the front panel.	95
Figure 4-26 Case structure where the input to the selector terminal is false, causing the false case to be executed and lighting up the "Less Than 0" Boolean on the front panel.....	96
Figure 4-27 Structure of a Producer-Consumer architecture. The upper loop is producing the data and saving it to a queue, while the consumer loop reads the data from the queue and performs the data reduction.....	97
Figure 4-28 Flow chart for a simple state machine. Flow chart describing temperature monitoring. The VI is initialized, with setting the threshold and maximum temperature values.	100
Figure 4-29 Example of how a state machine looks programmatically. It is a case structure that is in a while loop. Shift registers are used on the while loop to carry over the data to set the state of the case structure. Figure taken from National Instruments...	101
Figure 4-30 Common software architecture for control and monitoring applications. There is the User Interface, the Real-Time® VI or Host VI, and the FPGA VI or Target.	102
Figure 4-31 Flow diagram of VPLS State Machine	104
Figure 4-32 Diagram of the three signal responses and an example calculation using the data obtained.	107
Figure 4-33 Comparison of the data collected by the oscilloscope (top) and NI hardware (bottom). The mirror was set to rotate at 1000 RPM. The oscilloscope averaged 300 sweeps, and the NI data from a single curve of 300 measurements collected by the oscilloscope.	109
Figure 4-34 Full response curve overlay at 5, 10, 15, and 20 kRPM. The asymmetry on the negative angular offsets indicates trapping is occurring. Each point is an average of	

10 measurements recorded at each programmed delay. The angular offset does not take into consideration the jitter in the dye laser firing.....	111
Figure 4-35 Data collected after programming a delay corresponding to an angular offset of 540 degrees, fitted to a third order polynomial to better illustrate the shape of the curve. Each point is an average of 10 measurements at each programmed delay. The angular offset does not take into consideration the jitter in the dye laser firing.	113
Figure 4-36 Picture of the jet that delivers the NO ₂ across the beam path. The NO ₂ enters through the back of the jet, while house air is used to prevent the gas from dispersing after leaving the jet nozzle before being collected by the funnel connect to a vacuum line.	115
Figure 4-37 The top curve (squares) is the data obtained with no gas present while the lower curve (circles) is with the gas present. The y-axis is the PMT voltage observed for each angular offset, and each point is an average of 10 measurements at the programmed delay. The angular offset does not take into consideration the jitter in the dye laser firing.....	116
Figure 4-38 Optics lab simulation of the P5 version with the second folding mirror being replaced by a concave mirror. CM 1 (concave mirror 1), EM (entrance mirror), RM (rotating mirror), CM 2 (concave mirror 2)	119
Figure 4-39 Looking at the angle of incidence of folding mirror 1 (left) and folding mirror 2 (right).....	120
Figure 4-40 Data from LGR showing the relationship between mirror reflectivity and the incident angle of the light. Greater reflectivity corresponds to less light passing through the mirror, resulting in a greater number of theoretical trips through the cavity.....	121
Figure 5-1 VPCS single mirror design. CM (concave mirror), M (flat mirror), RM (rotating mirror), S (source), PMT (photomultiplier tube).....	123
Figure 5-2 Magnified image of a slit in a dielectric mirror (30-fold magnification)	125
Figure 5-3 SEM micrograph of dielectric mirror following ablation with a single laser pulse. Figure take from Reference 5.....	127
Figure 5-4 Schematic diagram of the Brewster's-angle flow cell. Figure taken from Reference 6.	129
Figure 5-5 Schematic representation of a dove prism. The Evanescent waves propagate out a small distance to probe any sample in contact with the dove prism.	130

LIST OF TABLES

Table 2-1 Theoretical calculation of pathlength enhancement for an idealized VPCS experiment.	25
Table 3-1. Specifications of the Agilent Photodiode Array Spectrophotometer. ²	51
Table 3-2. The key specifications for the Nitrogen Laser Model GL-3300. ³	52
Table 3-3. Key specifications of the HeNe used to monitor the rotational speed of the mirror. ⁴	54
Table 3-4. Hardware specifics of the NI-5761 Digitizer. ⁵	55
Table 3-5. Key Specifications for NI 7965R FPGA Module. ⁶	55
Table 3-6. Specifications for PXIe-8108 controller for the VPCS system. ⁷	56
Table 3-7. Prosilica GC camera specifications. ⁸	57
Table 4-1 Operating settings of the two oscilloscopes utilized by the P4 PTS prototype	62
Table 4-2 The Displayed rotational speed is the value recorded from the digital screen of the motor. The Scope data was the calculated rotational speed from an average of 300 sweeps. The LabVIEW values were collected from a single run, with the rotational speed being calculated for 10 consecutive rotations.	110
Table 4-3 Calculated number of maximum trips through the cavity at each rotational speed tested.....	117

ACKNOWLEDGEMENTS

This work has been supported by University of Wisconsin-Systems (WiSys) Applied Research Grant Program and Kettle Moraine Analytical.

I would like to thank my advisor Dr. Joseph H. Aldstadt III. Without his patient guidance and mentorship, has made me the scientist I am today. I have learned many things from you and will carry these skills and attitude towards science as I move forward.

I would like to thank the members of my thesis committee, Dr. Mark Dietz, Dr. Peter Geissinger, Dr. Robert Olsson, and Dr. Jörg Woehl, your guidance has been invaluable over the past several years.

To Kamal Gupta of Sentient Revolution LLC. I thank you for taking the time to initially come in and share your knowledge and to then help out to the extent you have. I have learned a lot from you and cannot thank you enough. This work would not have been possible without your expertise.

The support from those at the University of Wisconsin-Milwaukee have been phenomenal. First Dr. Paul Henning, you are a wealth of knowledge and with any issue that I was having you had a sound explanation, or could point me in the right direction. Dan Shurilla, with the scope of this work you have had a hand in. The knowledge and skills you possess are second to none.

Over the course of my time the many peers that have helped me along the way. Dr. John Frost, I stand on your shoulders and the work that you have done, thank you for taking me under your wing. Liv Heidenreich, Brad Moran, Heather Adams, James Wankowski, Hannah Waige,

Lisa Kendhammer, Steve Kopitzke, Kelsey Hobart, Marie Nider, it has been a pleasure working with all of you.

The department staff, Elise Nicks, Shelly Harrington, Wendy Grober, and Kevin Blackburn. Thank you for all that you do to keep the department running.

To my friends and family, you were always there to provide support and words of encouragement. To Heather, who I have learned much from, but most importantly it is not about the destination, but the journey. My grandparents that have always been there to lend a helping hand.

My brother Kyle, one of the hardest working people that I know. I will always look up to you. Last but not least, my parents Andy and Kim. They have always been there and have supported all of my endeavors. I would not be what I am today if not for your guidance.

1. Absorption Spectroscopy

This chapter will discuss topics pertaining to absorption spectroscopy. First, the quintessential relationship that is the cornerstone of absorption spectroscopy measurements, the Beer-Lambert-Bouguer Law will be covered. Then various methods for improving detection limits in absorption spectroscopy, including several key techniques that have led to the development of the Variable Pathlength Cavity Spectrometer, will be discussed.

1.1. Background

In general, spectroscopy is the study of the interaction of electromagnetic radiation (EMR) with matter to probe the chemical and/or physical properties of atoms and molecules. There are several different types of analytical spectroscopy that include absorption, emission, luminescence, and scattering methods.¹ These techniques involve interactions of photons with electrons in either atomic or molecular species, the differences in these techniques being the response that is generated.

In the most common absorption spectroscopic measurements, light is absorbed from the ultraviolet (UV) (10-180 nm), visible (VIS) (180-780 nm), or infrared (IR) (0.78-300 μm) regions.¹ These different ranges of wavelengths probe different energy level transitions in atoms or molecules. For example, in the UV-VIS region the energetic interactions involve valence electronic transitions, while IR energies correspond to the rotation and the vibrations of atoms within molecules. Figure 1-1 represents the process that occurs at the atomic level. Part (a) of the diagram illustrates that there is incident radiation that is interacting with the

species of interest. This sample is placed in the path of incident radiation, and if the frequency of the radiation corresponds to the energy required to excite, the sample energy is absorbed and the power of the transmitted radiation is lower than the incident radiation. In this diagram, the valence electrons are located initially in the ground state and if the incident radiation's energy is equal to the exact difference between quantized transitions, then the electrons can be excited to the higher energy state, as shown in Figure 1-1(b). These transitions are specific to the atom or molecule resulting in a characteristic absorption profile for a given species.

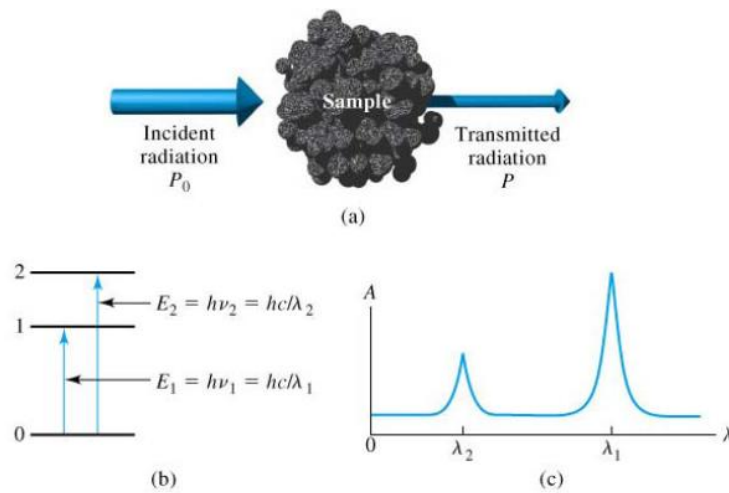


Figure 1-1. The absorption process. Radiation of incident radiant power P_0 can be absorbed by the analyte, resulting in a transmitted beam of lower power (P). For absorption to occur, the energy of the incident beam must correspond to one of the energy differences shown in (b). The resulting spectrum is shown in (c). Figure taken from Reference 1.

1.2. Beer-Lambert-Bouguer Law

The absorption of EMR by a chemical species can be used to quantitatively determine the chemical concentration of that species in a sample. Consider a spectroscopic experiment based on the absorption of VIS light by an aqueous solution. If the aqueous sample solution contains a generic molecule (X-Y) that can absorb EMR at a particular wavelength range in the VIS region, a fraction of the incident light power will not be transmitted to the detector. That is to say, the transmittance (T) – the ratio of the transmitted light power (P) to the incident light power (P_0) – will decrease as the absorbance increases.

$$T = P / P_0 \quad [1.1]$$

The absorbance (A) of a medium is defined by

$$A = -\log_{10} T = \log (P_0 / P) \quad [1.2]$$

Ideally, the amount of VIS light that is absorbed by X-Y is directly proportional to the concentration of X-Y in the sample, as described by the well-known Beer-Lambert-Bouguer Law (or more simply known as “Beer’s Law”):

$$A = \epsilon b C \quad [1.3]$$

where A is the absorbance – the negative of the base-10 logarithm of the transmittance (unitless), ϵ is the molar absorptivity of X-Y, which is a probabilistic function of chemical structure (liters per mole-cm), b is the pathlength of light – the distance the light travels through the sample compartment (cm), and C is the concentration of X-Y in the sample (moles per liter).

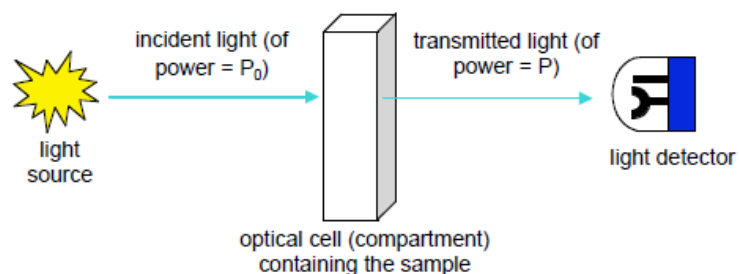


Figure 1-2 The basic experimental setup in molecular absorption spectroscopy

Visible absorbance spectroscopy based on Beer's law is one of the most widely used measurements in chemical analysis. It is estimated that there are greater than one million measurements of this type per day in the U.S., particularly in clinical, forensic, environmental, and industrial laboratories¹. Other interactions of EMR with matter, e.g., the emission and scattering of light, are also widely measured, although the theoretical relationships between the EMR and emission or scattering phenomena are expressed differently than described above for absorbance measurements.

There are several assumptions that are made during the derivation of Beer's Law. The incident radiation is monochromatic; the absorbing species act independent of each other; the incident radiation consist of parallel rays that are traveling perpendicular to the surface of the absorbing medium; the pathlength traversed is uniform over the cross section of the beam, (i.e., all the rays traverse an equal distance through the sample); the absorbing medium is

homogeneous and does not scatter the radiation; and finally, the incident power is not too large so as to cause a saturation effect.²

1.3. Methods for Increasing Pathlength

Upon inspection of Beer's Law, it is obvious that A is directly proportional to b – which is the only experimental variable (ϵ is a constant for a given chemical structure at a given energy). Therefore, one would expect that a lower concentration of a molecule such as X-Y could be measured simply by increasing b .

Commercially available cuvettes are available in different size ranges. At the smaller end, the pathlengths range from 1 mm to 5 cm, and at the larger end of the range, pathlengths can be up to 10 cm. While increasing the pathlength allows for lower detection limits, there are downfalls to selecting to larger cuvettes because the larger the cuvette, the more sample required. If more sample is required to fill the cuvette, then there will be increased light losses that are possible because of the greater distance which the light has to traverse.

While detection limits depend on several conditions, i.e., the instrument (e.g., wavelength, slit width, etc.) and analyte (e.g., molar absorptivity), the values observed ideally fall between 10^{-3} and 10^{-5} absorbance units (A.U.). As the matrix becomes more complex, detection limits may rise to 10^{-2} A.U. or higher, corresponding to concentrations in the micromolar range.²

There are three general approaches that will be discussed for increasing pathlength: various atmospheric measurement techniques, Differential Optical Absorption Spectroscopy, multi-pass techniques, and cavity-based techniques.

1.3.1. Differential Optical Absorption Spectroscopy

Atmospheric measurements must satisfy two main requirements. First, they must be able to detect species at their ambient levels, which can be as low as the parts-per-trillion (pptr) and parts-per-billion (ppb) range.³ Second, the measurement must be selective because interference rejection is crucial. Conventional absorption measurements cannot measure to the trace levels that are required.^{1-2, 4}

Differential Optical Absorption Spectroscopy (DOAS), developed in 1978, revolutionized atmospheric monitoring instruments by increasing the pathlength to 600 m.⁵ This was accomplished by using a broadband source that was directed to a distant mirror for reflection back to a detector that was located near the source. The key to this method was that rapid measurements of the observed intensity were possible (i.e., to monitor changes in the level of a given analyte). Atmospheric processes can occur over short time scales due to processes such as turbulence, Rayleigh scattering, and Mie scattering.⁶⁻⁷

DOAS can be categorized into two distinct methods: active and passive.³ As shown in Figure 1-3, the passive method uses light sources that originate outside the atmosphere, e.g., the Sun, other stars, or the Moon. Active methods require a light source that originates in the

atmosphere, has high intensity, and transmits radiation over a wide spectral range. A source that is commonly used is the Xenon Arc Lamp.³

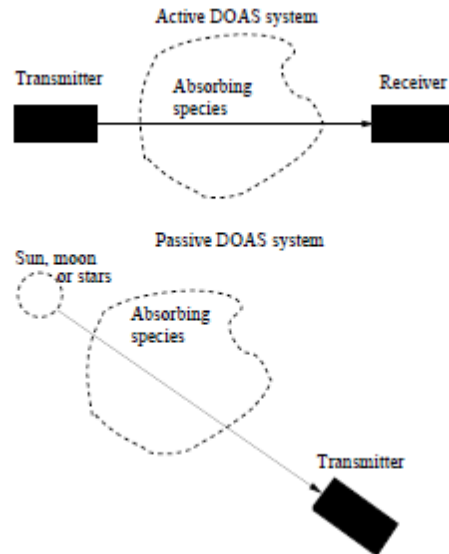


Figure 1-3. DOAS systems can be either active or passive depending on the source of radiation used. Image taken from Reference 4.

Figure 1-4 demonstrates that the absolute intensity (I_0) is irrelevant for the determination of the unknown. Because the region of the spectrum where the absorption process is monitored is narrow relative to other atmospheric interactions mentioned earlier, the relative I_0 (noted as I_0' in Figure 1-4) can be interpolated from the intensity on either side of the absorption band.³

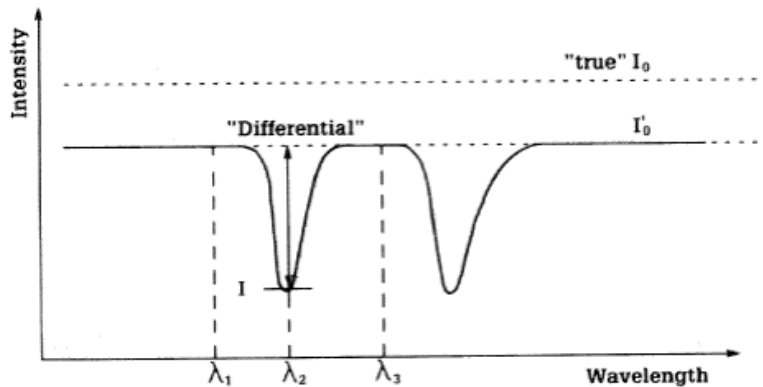


Figure 1-4. A typical response in DOAS. The absolute incident intensity (I_0) is not of importance, primarily because of the scattering losses that occur. (I'_0) is interpolated from the intensity that is observed on either side of the narrow absorption line of the species. Image taken from Reference 4.

This method has been successfully applied to the monitoring of nitric oxide species (NO_x). Shorter wavelength measurements are limited by an increase in Rayleigh scattering and O_2 absorption. NO can be monitored over the 200-230 nm range⁸, while NO_2 and HNO_2 can be monitored from 300-400 nm^{9,10,11,12}, beyond 400 nm the predominant absorbing species is NO_2 .¹³ Detection limits as low as 2 ppbv have been reported for NO_2 species.³

There are several advantages to this method. Atmospheric phenomena like Rayleigh and Mie scattering occur but do not interfere with the measurement since I_0 is interpolated from either side of the absorption line. Due to the broad band spectra and the long pathlengths there is high sensitivity. Using a broadband source allows for observation of numerous species simultaneously in a measurement. There are some disadvantages that come into play, however. First there are a relatively limited number of molecules that have the requisite absorption characteristics in the UV and VIS region for DOAS instruments (e.g., bands that

correspond to the highest intensities from the Xe arc source), and secondly precipitation (e.g., rain, snow, fog, etc.) will attenuate the signal because of scattering.

1.3.2. Laboratory Methods for Pathlength Enhancement

The DOAS technique is an excellent example of increasing pathlength to realize lower detection limits. This technique is well suited for what it does, i.e., atmospheric monitoring. However, how can the same goal of increasing pathlength be achieved for a bench-top application? Various approaches have been developed over the past ~75 years that are intended to provide a solution toward this end. Multi-pass cavity instruments that use mirrors to create an optical cavity have been the most widely studied approaches. There are two different ways that these cavities have been designed. In the first approach, light is injected into the cavity and a slight off-set in the mirror positions causes the light to trace a “zig-zag” path through the cavity. Several “zig-zag” designs have been reported in the literature. More recently, an alternative approach known as the “ring-down” design has generated great interest. In the “ring-down” experiment, the injected light remains on a fixed path (i.e., along the incident axis) before being measured at the detector. Both the “zig-zag” and “ring-down” designs will be discussed in the following sections.

1.3.2.1. Multi-pass “Zig-Zag” Cavity Designs

The White Cell, published in 1942, was the first design to create an optical cavity with the intention of increasing the pathlength.¹⁴ The design of the system requires three concave

mirrors with the same radius of curvature. As Figure 1-5 illustrates, two mirrors (A and A') are located next to each other while the third (mirror B) is located at a distance that is equal to the radius of curvature. The light enters the cavity and follows the path: source (above B) → A → 1 → A' → 2 → A → 3 → A' → 4 (detector). As mentioned earlier, with these multi-pass designs, the light traverses the cavity but along different axes within the cavity.

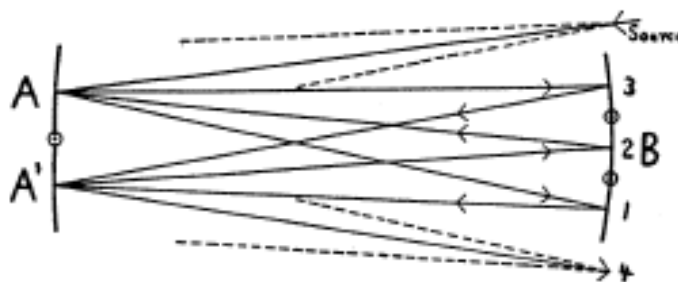


Figure 1-5. Schematic diagram of the White Cell. The distance from mirror A/A' to mirror B is equal to their radius of curvature as a means to establish conjugate foci on the surface of the mirrors. Image taken from Reference 14.

With this optical layout and using mirrors with a radius of curvature of 62.5 cm, White observed that light traversed the cavity 90 times corresponding to a pathlength of 56 meters.¹⁴ Since this method was introduced in 1942, there have been several techniques that have taken this platform and tried to build upon it.¹⁵ Notably, Hanst, Lefohn, and Gay applied an interferometer to this method in 1973.¹⁶ Their work led to a reduction in interference and increased the signal-to-noise ratio. They calculated that their approach would be able to detect less than one part per billion with 50 passes through a 10 m cell.¹⁶

In 1965, Herriott and Schulte reported a confocal arrangement of mirrors to direct a laser beam over large areas.¹⁷ Using two concave mirrors, after the light was injected into the

cavity it followed an elliptical path on the surface of the mirror and traversed the cavity, as shown in Figure 1-6. They applied a “perturber mirror” to re-initiate the light to create a slightly shifted elliptical shape. This is illustrated in Figure 1-6 as the second time around the elliptical path (note that point five is slightly shifted from point one). The perturber mirror can be seen in the upper right of Figure 1-7.

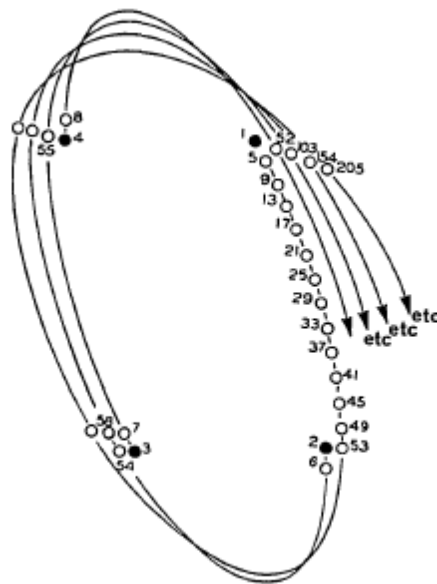


Figure 1-6. An example of the order of the spots position on the mirror. Image taken from Reference 17.

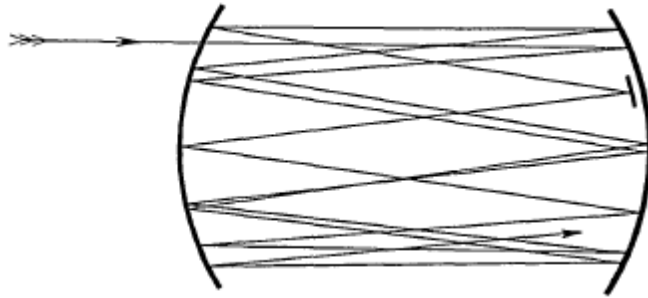


Figure 1-7. Cross section of the optical cavity showing the “perturber mirror” position. Image taken from Reference 17.

Herriott and Schulte’s design (known as the “Herriott Cell”) for a multi-pass instrument has had recent medical applications. Cancer cells produce NO in low concentrations to cause proliferation of the cells. Using a 100 m astigmatic Herriott Cell, Köhring et al. were able to obtain a minimum detection limit for NO of 124 parts-per-trillion (pptr), based upon 160 seconds of averaging time.¹⁸

The White and Herriott Cells were the pioneering designs in multi-pass cavity approaches for benchtop applications. There have been a multitude of techniques that have been developed based on the ground work which these two key approaches established.^{19,20,21,22,23,24} New techniques are constantly developing for advancing technologies. As the next section will describe, a technique has been developed that is not limited by the number of trips as the light “walks through” the cavity.

1.3.2.2. Ring-down Cavity Design

The “ring-down” design is the basis of “Cavity Ring-Down Spectroscopy (CRDS)”, a technique that was made possible by the development of ancillary technologies. Highly reflective mirrors, created by sputter-coating ions on to highly polished substrates, began to appear in the 1980’s as a “spin-off” defense technology (i.e., the Reagan era “Star Wars” program). These mirrors, called dielectric mirrors, alternate the layers that are sputter-coated between high and low refractive indices as shown in Figure 1-8. These layers are applied in one-quarter wavelength thicknesses and, because of Fresnel reflections, as light encounters the point in the layering where the refractive index changes, the wave undergoes a 180° phase shift and constructively interferes. Note that the light must be perpendicular to the mirror, but in Figure 1-8 the incident light is slightly off-normal to better depict the Fresnel reflections occurring at the alternating layers.

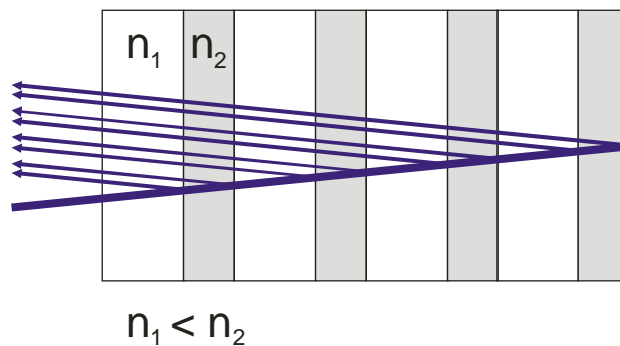


Figure 1-8. Illustration of sputter-coated layers of alternating refractive indices with an incident light striking the mirror and Fresnel reflections occurring at the point where the refractive index changes. (Diagram compliments of Dr. Paul Henning)

As the reflectivity of the mirrors increased, it became more challenging for engineers to measure their reflectivity so new methods for calculating the reflectivity were needed.

Anderson, Frisch, and Masser were the first to report an instrument that had a CRDS design.²⁵

They created an optical cavity with two mirrors, injected laser light into the cavity, and then rapidly turned it off. They were then able to observe the decay of the light trapped in the cavity after it passed through one of the mirrors. This allowed them to determine the relationship between the signal decay time (k) and the mirror reflectivity (R):

$$k = (1 - R)c/L \quad [1.4]$$

where c is the speed of light, and L is the distance between the mirrors. The first time that a chemical measurement was made by CRDS was reported by O'Keefe and Deacon in 1988.²⁶

Using a design for measuring mirror reflectivity identical to that used in the work of Anderson et al., they observed faint VIS absorptions in ambient air. Figure 1-9 illustrates how the decay curve was fitted to the observed "ring-down" signal. Even though the dielectric mirrors are highly reflective, there are some losses as light passes through the mirror (where R is $< 100\%$).

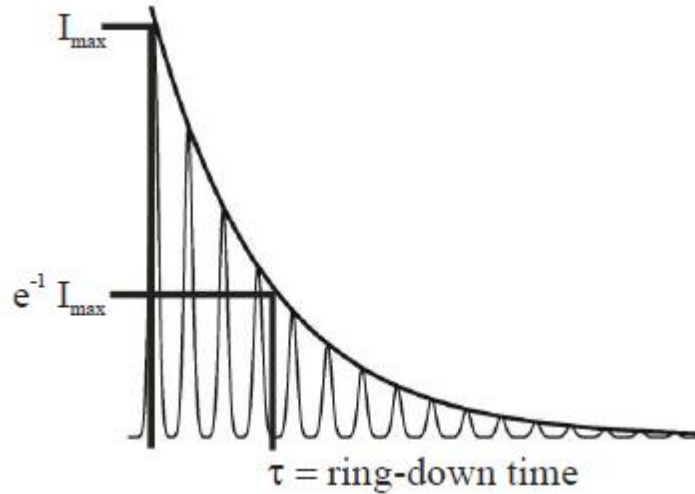


Figure 1-9. CRDS response showing the observed detector response (thin pulsing line), and the fitted decay curve. Image taken from Reference 19

The decay of the light within the cavity can be fitted to a first-order exponential function (Equation 1.5):

$$I(t) = I_{\max} \exp(-t/\tau_q) \quad [1.5]$$

where I_0 is the incident source intensity, t is the time, and τ_q is the lifetime of the light inside the cavity. τ_q is defined in Equation 1.6:

$$\tau_q = 2l c (T + L) \quad [1.6]$$

where T is the transmissivity of the mirrors, L is the single-pass loss within the cavity, c is the speed of light, and l is the length of the cavity. The ring-down time, τ , which is related to absorbance, is found by solving the decay function [1.5] for t when:²⁵

$$I = e^{-1} I_{\max} \quad [1.7]$$

The simplest CRDS setup is illustrated in Figure 1-10. The source is a pulsed laser, which is injected into the cavity by passing through the back or uncoated side of the dielectric mirror. There are two concave mirrors that are separated by length L , followed by the detector which is typically either a photomultiplier tube (PMT) or photodiode. The signal is read on the oscilloscope and then transferred for processing to the computer.

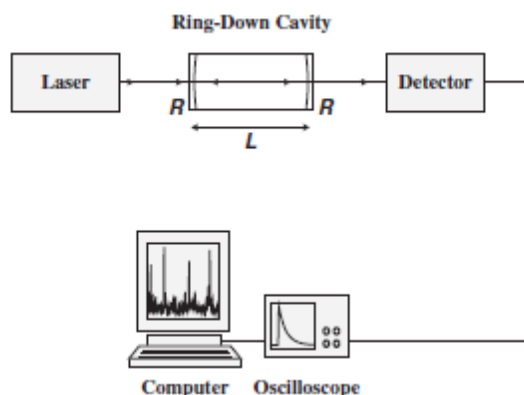


Figure 1-10. Experimental set-up for cavity ring-down absorption spectroscopy. The sample is contained in the cavity with length L and mirror reflectivity R . Image taken from Reference 21.

This technique has seen many improvements to enhance its capabilities. In the 30 years since its initial development, effective pathlength enhancements of as much as 50,000 times have been reported.^{27,28} Advancements in the technique include the use of continuous wave (cw) lasers^{29,30,31} and fiber loops.^{32,33} Condensed phases have also been studied using CRDS.^{34,35} The enhancement factor is appealing in techniques like liquid chromatography and capillary electrophoresis³⁶ where there are short sample pathlengths and desired detection limits are low. Variations of the original CRDS experiment also include using evanescent waves to probe condensed phases by the use of a Dove prism.^{37,38,39,40} Another approach involved the

custom building of a flow cell, illustrated in Figure 1-11. The flow cell is fabricated so that each interface between changing refractive indices is at Brewster's angle, which minimizes the optical losses within the system while allowing a flowing stream to be analyzed.^{41,42}

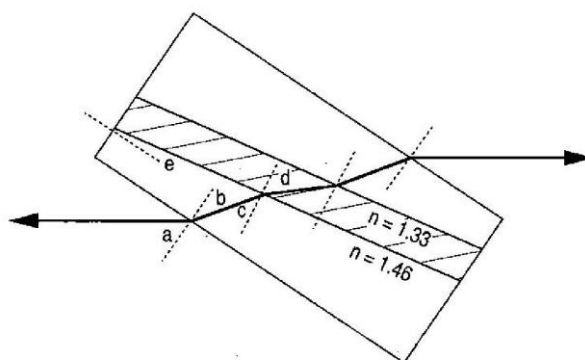


Figure 1-11. Schematic diagram of the Brewster's-angle flow cell. The refractive index is 1.46 for fused silica and 1.33 for water, the optimal wedge angle, e , is 7.9° . With this configuration the cell should be tilted so that the angle of light incidence, a , is 55.6° . The light refracts through the cell, hitting each surface at the appropriate angle for minimum reflection. These Brewster's angles are $b = 34.4^\circ$, $c = 42.3^\circ$, and $d = 47.7^\circ$. Image taken from figure 37.

One of the limitations of CRDS is that this technique works only for trace-level concentrations. If the concentration of the analyte becomes too high, the decay time occurs so quickly that the detector is not able to collect a signal. The next section of this dissertation describes a novel instrument that can bridge the gap of concentration ranges for measurements between relatively insensitive single-pass absorption spectroscopy and CRDS.

LITERATURE CITED

1. Skoog, D. A.; Holler, F. J.; Crouch, S. R., In *Principles of Instrumental Analysis*, Sixth ed.; Kiselica, S., Ed. David Harris: Belmont Ca., 2007; pp 188-190.
2. James D. Ingle, J.; Crouch, S. R., *Spectrochemical Analysis*. Prentice-Hall, Inc.: 1988.
3. Platt, U., Differential Optical Absorption Spectroscopy. In *Air Monitoring by Spectroscopic Techniques*, Sigrist, M. W., Ed. John Wiley & Sons, Inc.: 1994; p 58.
4. Ball, S. M.; Jones, R. L., Broad Band Cavity Ring-Down Spectroscopy. *Chemical Reviews* **2003**, (103), 23.
5. Platt, U., Dry Deposition of Sulfur Dioxide. *Atmospheric Environment* **1978**, 12, 4.
6. Pendorf, R. J., Tables of refractive index for standard air and the Rayleigh scattering coefficient for the spectral region between 0.2 and 20.0 μm and their application to atmospheric optics. *Journal of Optical Society* **1957**, 47, 6.
7. Junge, C. E., *Air Chemistry and Radioactivity*. Academic Press, New York and London: 1963; Vol. 4.
8. Tanjime, T.; Saheki, T.; Ito, K., Absorption characteristics of the γ -0 band of nitric oxide. *Applied Optics* **1978**, 17, 5.
9. Hall, C. T.; Blacet, F. E., Separation of the absorption spectra of NO_2 and N_2O_4 in the range of 2400-5000 \AA . *Journal of Chemical Physics* **1952**, 20, 4.
10. Schneider, W.; Moortgat, C. K.; Tyndall, G. S.; Burrows, J. P., Absorption cross-sections of NO_2 in the UV and visible region (200-700 nm) at 298k. *Journal of Photochemistry and Photobiology* **1987**, 40, 22.
11. Newitt, D. M.; Outridge, L. E., The ultraviolet absorption bands ascribed to HNO_2 *Journal of Chemical Physics* **1938**, 12, 11.
12. Bongartz, A.; Kames, J.; Welter, F.; Schurath, U., Near-UV absorption cross sections and trans/cis equilibrium of nitrous acid. *Journal of Physical Chemistry* **1991**, 95, 6.
13. Perner, D.; Platt, U., Absorption of light in the atmosphere by collision pairs of oxygen (O_2)₂ *Geophysical Research Letters* **1980**, 3, 2.
14. White, J. U., Long Optical Paths of Large Aperture. *Journal of the Optical Societies of America* **1942**, 32, 4.
15. White, J. U., Very long optical paths in air. *Journal of the Optical Society of America* **1976**, 66 (5), 411-416.

16. Hanst, P. L.; Lefohn, A. S.; Gay, B. W., Detection of atmospheric pollutants at parts-per-billion levels by infrared spectroscopy. *Applied Spectroscopy* **1973**, *27* (3), 188-98.
17. Herriott, D. R.; Schulte, H. J., Folded Optical Delay Lines. *Applied Optics* **1965**, *4* (8), 7.
18. Kohring, M.; Huang, S.; Jiang, M.; Ren, W.; Willer, U.; Caneba, C.; Yang, L.; Nagrath, D.; Schade, W.; Tittel, F. K., QCL-based TDLAS sensor for detection of NO toward emission measurements from ovarian cancer cells. *Applied Physics B* **2014**, *177*, 445-451.
19. Gebbie, H. A.; Bohlander, R. A., Nonresonant Cavity as a Long Path Absorption Cell. *Applied Optics* **1972**, *11* (4), 6.
20. Wang, T.; Aiken, J. H.; Hule, C. W.; Hartwick, R. A., Nanoliter-Scale Multireflection Cell for Absorption Detection in Capillary Electrophoresis. *Analytical Chemistry* **1991**, *63* (14), 5.
21. Nwaboh, J. A.; Desbois, T.; Romanini, D.; Schiel, D.; Werhahn, O., Molecular Laser Spectroscopy as a Tool for Gas Analysis Applications. *International Journal of Spectroscopy* **2011**, *2011*, 12.
22. Kim, K. C.; Griggs, E.; Person, W. B., Kilometer-path low-temperature multiple-reflection cell for laser spectroscopy using tunable semiconductor diodes. *Applied Optics* **1978**, *17* (16), 5.
23. Xi, X.; Young, E. S., Axial-Beam On-Column Absorption Detection for Open Tubular Capillary Liquid Chromatography. *Analytical Chemistry* **1990**, *62* (15), 6.
24. Kratz, H. R.; Mack, J. E., A Long Optical Path in a Restricted Space. *Journal of Optical Society of America* **1942**, *32*, 8.
25. Anderson, D. Z.; Frisch, J. C.; Masser, C. S., Mirror reflectometer based on optical cavity decay time. *Applied Optics* **1984**, *23* (8), 11.
26. O'Keefe, A.; Deacon, D. A. G., Cavity ring-down optical spectrometer for absorption measurements using pulsed laser sources. *Review of Scientific Instrumentation* **1988**, *59*, 2544-2551.
27. Scherer, J. J.; O'Keefe, P. A.; Saykally, R. J., Cavity Ring-down Laser Absorption Spectroscopy: History, Development, and Application to Pulsed Molecular Beams. *Chemical Reviews* **1997**, *97* (1), 25-51.
28. Romanini, D.; Lehmann, K. K., Ring-down Cavity Absorption Spectroscopy of the very weak HCN Overtone Bands with six, seven, and eight Stretching Quanta. *Journal of Chemical Physics* **2003**, *99* (9), 6287-6301.
29. Liu, A. W.; Kassi, S.; Perevalov, V. I.; Tashkun, S. A.; Campargue, A., High sensitivity CW-Cavity Ring Down Spectroscopy of N₂O near 1.28 μ m. *Journal of Molecular Spectroscopy* **2011**, (267), 191-199.
30. Wagner, N. L.; Dube, W. P.; Washenfelder, R. A.; Young, C. J.; Pollack, I. B.; Ryerson, T. B.; Brown, S. S., Diode Laser-Based Cavity Ring-Down Instrument for NO₃, N₂O₅, NO, NO₂, and O₃ from Aircraft. *Atmospheric Measurement Techniques* **2011**, *4*, 15.

31. Washenfelder, R. A.; Wagner, N. L.; Dube, W. P.; Brown, S. S., Measurement of Atmospheric Ozone by Cavity Ring-down Spectroscopy. *Environmental Science and Technology* **2011**.
32. Brown, R. S.; Kozin, I.; Tong, Z.; Oleschuk, R. D.; Loock, H.-P., Fiber-loop ring-down spectroscopy. *Journal of Chemical Physics* **2002**, *117* (23), 10444-10447.
33. Tong, Z.; Jakubinek, M.; Wrigh, A.; Gillie, A.; Loock, H.-P., Fiber-loop ring-down spectroscopy: A sensitive absorption technique for small liquid samples. *Review of Scientific Instruments* **2003**, *74* (11), 9.
34. Sneppen, L. v. d.; Wiskerke, A.; Ariese, F.; Gooijer, C.; Ubachs, W., Improving sensitivity of HPLC absorption detection by cavity ring-down spectroscopy in a liquid-only cavity. *Analytica Chimica Acta* **2005**, *558* (1-2), 5.
35. Xu, S.; Sha, G.; Xie, J., Cavity Ring-Down Spectroscopy in Liquid Phase. *Review of Scientific Instruments* **2002**, *73* (255-258).
36. Culbertson, C. T.; Jorgenson, J. W., Lower the UV Absorbance Detection Limit in Capillary Zone Electrophoresis Using a Single Linear Photodiode Array Detector. *Analytical Chemistry* **1998**, *70* (13), 10.
37. Sneppen, L. v. d.; Ariese, F.; Gooijer, C.; Ubachs, W., Liquid-Phase and Evanescent-Wave Cavity Ring-Down Spectroscopy in Analytical Chemistry. *Annual Review of Analytical Chemistry* **2009**, *2* (1), 23.
38. Shaw, A. M.; Hannon, T. E.; L, F.; Zare, R. N., Adsorption of Crystal Violet to the Silica-Water Interface Moniterd by Evanescent Wave Cavity Ring-Down Spectroscopy. *Journal of Physical Chemistry B* **2003**, *107* (29), 6.
39. Martin, W. B.; Mirov, S.; Martyshkin, D.; Venugopalan, R.; Shaw, A. M., Hemoglobin Adsorption Isotherm at the Silica-Water Interface with Evanescent Wave Cavity Ring-Down Spectroscopy. *Journal of Biomedical Optics* **2005**, *10* (2), 7.
40. Schnippering, M.; Nei, S. R. T.; Mackenzie, S. R.; Unwin, P. R., Evanescent wave cavity-based spectroscopic techniques as probes of interfacial processes. *Chemical Society Reviews* **2011**, (40), 14.
41. Snyder, K. L.; Zare, R. N., Cavity Rind-Down Spectroscopy as a Detector for Liquid Chromatography. *Analytical Chemistry* **2003**, *75* (13), 3086-3091.
42. Betchel, K. L.; Zare, R.; Kachanov, A. A.; Sanders, S. S.; Paldus, B. A., Moving Beyond Traditional UV-Vis Absorption Detection: Cavity Ring-Down Spectroscopy for HPLC. *Analytical Chemistry* **2005**, *77* (4), 6.

2. Variable Pathlength Cavity Spectroscopy

Variable Pathlength Cavity Spectroscopy (VPCS) is based on the formation of a high-finesse optical cavity, or simply a cavity that has low round trip losses, in which the pathlength can be adjusted by means of rotating mirrors. The mirrors are highly reflective dielectric mirrors, and the rotating mirrors have a slit milled into them, as shown in Figure 2-1. The slits allow for more light to enter the cavity and subsequently make more passes through the sample. The light that has been trapped in the cavity can then emerge from the cavity for detection. There are two fixed (steering) mirrors within the optical cavity but it is the rotating mirrors that define the cavity. The rotating mirrors are mounted on an axle with a relative angle of separation between the slits, designated as theta (θ). A high intensity, collimated, continuous wave (cw) source is used to inject light into the cavity. It is aligned to the rear-facing side of the entrance mirror so that as the entrance slit rotates into the beam path, the light can enter the cavity. The light then travels through a delay loop comprised of two fixed dielectric mirrors. This increases the length of the cavity to allow more light to be trapped as the entrance mirror rotates out of the beam path. The light that is now trapped in the cavity will continue to traverse the cavity and pass through the sample, which can be located anywhere in the cavity. Once the exit slit rotates into the beam path, all the light can then exit the cavity and travel to the detector.

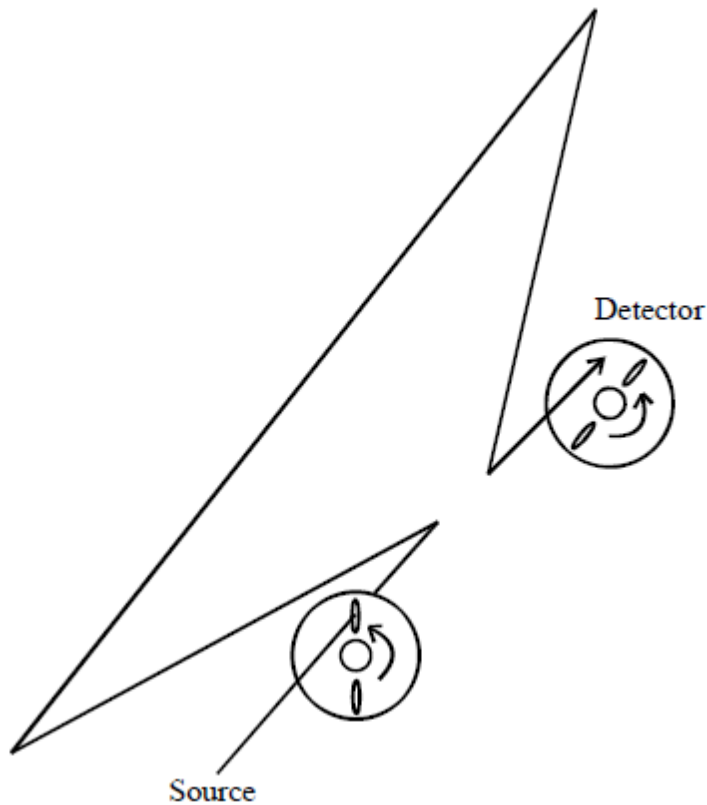


Figure 2-1. Schematic representation of the design of the variable pathlength cavity spectrometer beam path using a cw source and a rotating entrance and exit mirror. The four mirrors used to create the delay loop inside the cavity have been omitted for clarity. Image taken from Reference 1.

2.1.Theory

2.1.1. Calculation of Pathlength Enhancement

A theoretical expression for signal amplification by the enhancement of pathlength can be derived. The time required for the mirror to make one revolution is given by:

$$t_{rot} = f^{-1} \quad [2.1]$$

where f is the rotational frequency of the mirror in Hertz (Hz).

The amount of time the light stays trapped inside the cavity is equal to the time required for the mirror to rotate over the angle θ . The angle θ is formed between the center of the projected beam spot on the rotating mirror and the exit slit, as illustrated in Figure 2-2. The amount of time the light is trapped in the cavity is therefore given by:

$$t_{\text{trap}} = t_{\text{rot}} (\theta / 2\pi) \quad [2.2]$$

where θ is measured in radians. The distance traveled by the light during this time (d_T) is:

$$d_T = c_a \times t_{\text{trap}} \quad [2.3]$$

where c_a is the speed of light in air ($2.997 \times 10^8 \text{ m s}^{-1}$). The total number of reflections (N_r) that would occur during this time is given by:

$$N_r = n_r (d_T / d_p) - 1 \quad [2.4]$$

where d_p is the pathlength within the cavity (the distance from the face of the entrance mirror to the steering mirrors and then to the face of the rotating mirror). The number of mirrored surfaces the light strikes when traveling d_p is represented by n_r . Note that one reflection must be subtracted from the total number of reflections because when the light is released from the cavity, a reflection does not occur.

Assuming that no absorbers are present within the cavity, the transmissivity (T) after N reflections from a mirrored surface of specific reflectivity (R) is given by:

$$T = R^{N_r} \quad [2.5]$$

The total number of passes through a sample (N_s) placed in the beam path is given by:

$$N_s = d_T / d_p \quad [2.6]$$

Thus the effective sample pathlength (b^*) would simply be:

$$b^* = b \times N_s \quad [2.6]$$

where b is the pathlength of the sample cell (i.e., during one pass of the beam). The amplification factor achieved (AF) would therefore be:

$$AF = b^* / b \quad [2.7]$$

Substitution of the factors derived above yields a theoretical expression for b^* :

$$b^* = (b c_a \theta) / (2\pi d_p f) \quad [2.8]$$

where b^* is the effective sample pathlength in meters, b is the physical sample pathlength in meters, c_a is the speed of light in air in meters per second, d_p is the cavity pathlength in meters, and f is the rotational frequency of the mirror in Hz or rotations per minute respectively.

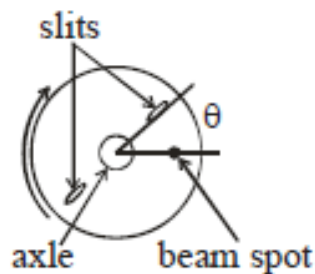


Figure 2-2. Schematic representation of the rotating mirror. Angle θ is defined as the angle between the center of the projected beam spot and the leading edge of the exit slit. It should be noted that while two slits are necessary for mirror balance, only one is utilized for the measurement. Image taken from Reference 2.

2.1.2. Example Calculation of b^*

This calculation is based on estimates using off-the-shelf components and the following (ideal) assumptions: (i) the rotating mirror is perfectly flat, (ii) the beam remains precisely collimated, (iii) vibrations which would de-stabilize the system are absent, and (iv) background absorption and scattering effects are non-existent.

Constant terms		
C_a	speed of light in air	$2.997 \times 10^8 \text{ m s}^{-1}$
Experimental Values		
b	physical sample pathlength	$1.0 \times 10^{-4} \text{ m}$ (0.10 mm)
R	mirror reflectivity	99.999%
n_r	number of cavity mirrors	2
f	frequency of rotation	90 Hz (5,400 RPM)
d_p	cavity length	3.0 m
θ	angular offset	0.52 radians (30°)
Calculated parameters		
t_{rot}	time to rotate mirror once	$1.11 \times 10^{-2} \text{ s}$
t_{trap}	time light remains trapped	$9.26 \times 10^{-4} \text{ s}$
d_T	distance travels	277,522 m
N_r	number of reflections	18,499
T	transmitted intensity	83.11%
N_s	number of passes through the sample	92,507
b^*	effective sample pathlength	9.25 m
AF	amplification factor	9,250

Table 2-1 Theoretical calculation of pathlength enhancement for an idealized VPCS experiment.

In this calculation, the mirror rotates at 90 Hz, a frequency that is easily attainable with commercial high-speed rotary motors. The width of the sample compartment is 0.10 mm and the cavity is 3.0 m. The time that the light is trapped within the cavity (i.e., passing through the sample) is about 11 ms. In this period of time, the trapped photons will travel almost 300 km, the light will be reflected almost 300,000 times, and approximately 6% of the light will still be

present for detection. The resulting pathlength thus increases from 0.10 mm to 9.25 m an almost 100,000-fold improvement.

2.1.3. Key Relationships

The relationship between rotational speed and angular offset will affect the number of passes through the sample and therefore the observed transmittance as illustrated in Figure 2-3. If the angular offset between the entrance slit and the exit slit were held constant and the rotational speed was varied, change in the transmittance and the observed pathlength would be observed. As the rotational speed of the mirror increases, the exit slit takes a shorter amount of time to rotate into the beam path compared to a slower rotational speed. Since the slit reaches the beam path sooner, the light can exit the cavity more quickly, because the light will take fewer trips through the sample, i.e., a higher transmittance will be observed with a shorter b^* . Conversely, as the rotational speed decreases, the light spends more time within the cavity and thus makes more passes through the sample, resulting in a lower transmittance and an increase in b^* .

If the rotational speed were held constant and the angular offset were to increase, there would be a larger offset between the entrance and exit slits. This causes the exit slit to take more time to rotate into the axis of the beam path resulting in a decrease in transmittance and an increase in b^* . The opposite would be true as well, i.e., if the angular offset were decreased there would be less time required for the exit slit to enter the beam path thereby resulting in a higher transmittance and decreased b^* .

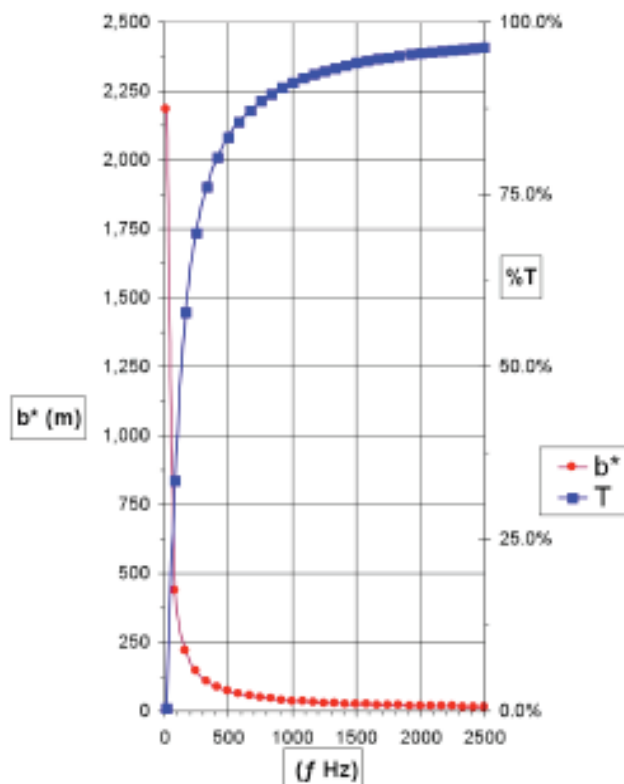


Figure 2-3. Theoretical relationship between the light transmittance (T) and the pathlength enhancement (b^*) that could be realized at an angular offset of 15 degrees and a physical pathlength of 0.01 m. Image taken from Reference 1.

It is through the manipulation of these variables that gives the VPCS such versatility over a wide concentration range. A key drawback of CRDS is that as the concentration of the analyte increases, a point is reached when the signal decay (“ring-down”) is too fast to measure. With the VPCS, the factors for the measurement can be selected to produce the optimal transmittance for a given concentration of analyte. As shown in the example calculation above, this can range from a single-pass measurement to 147,773 passes which corresponds to a pathlength of 0.010 m to 18 m.

2.2. Instrument Prototypes

Since the inception of the idea of the VPCS (originally as “Photon Trapping Spectroscopy”, or PTS) in 2007, there have been many modifications that have led to the current version of the prototype. This section will discuss the different stages that have shaped the development of the current mode, summarizing the initial work done by Dr. Beth Ruddy and the extensive work done by Dr. John Frost.^{2,1} The nomenclature of “*Pi* VPCS”, where “*i*” represents each successive stage in the development, will be used to differentiate among versions of the instrument.

2.2.1. VPCS Prototype 1

The initial prototype of the instrument was composed of five major components: a high intensity, collimated light source; several mirrors; the rotating axle and mount; a motor to the drive axle; and a PMT detector. The source was a Uni-Phase 500-mW CW argon-ion laser operating at a wavelength of 488 nm. The air cooled laser had an output beam diameter of ~0.6 mm and a divergence of ~0.9 milli-radians. The steering mirrors that directed the light to the entrance mirror were silvered mirrors that were 25 mm in diameter. The mirrors were reported to have a reflectivity of 0.999995 at the operating wavelength of 488 nm and were specified to have a surface roughness of less than 0.05 nm radius-of-curvature (ROC).² Figure 1-15 shows the 5-mm diameter hole, which was drilled into the center of the mirror for the axle as well as the two 1-mm by 4-mm slits that were 180 degrees apart.

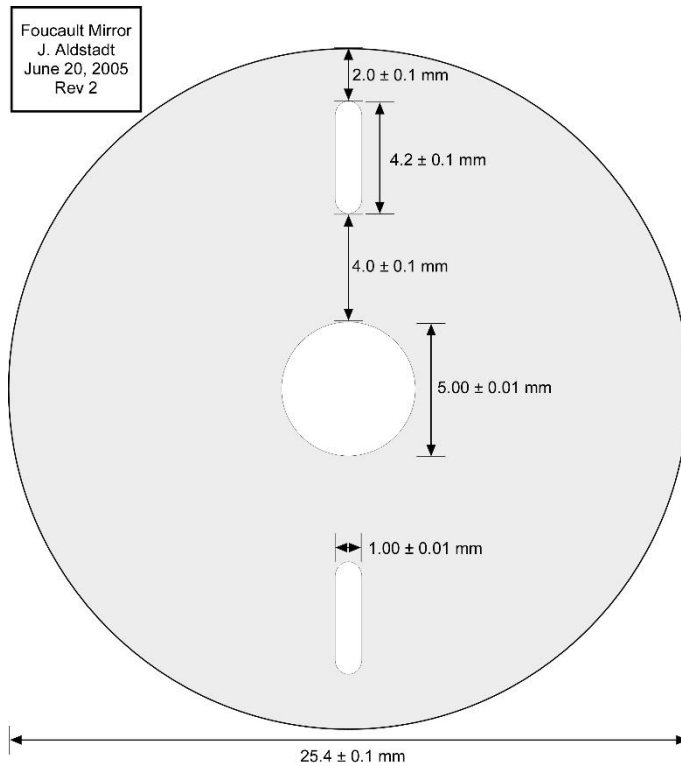


Figure 2-4. Original dielectric mirror specifications for the P1 VPCS.

The axle layout and mount of the P1 prototype are shown in Figure 2-5. The rotating mirrors were mounted on an axle that is 18 cm long and 4 mm in diameter and was expanded at each end to 4.75 mm. The mirrors were slip-fit onto Teflon bushings which pressed against the 4.75 mm tapers. Neoprene and steel washers held the mirror against the 4.75 mm tapers with a nut attached to a threaded portion of the axle, which stepped back down to 3 mm at each end. The axle was supported on each end by an “L” shaped bracket containing a stainless steel ball bearing. Behind one mirror, a brass pulley was attached to the 3 mm section of the axle by a set screw.

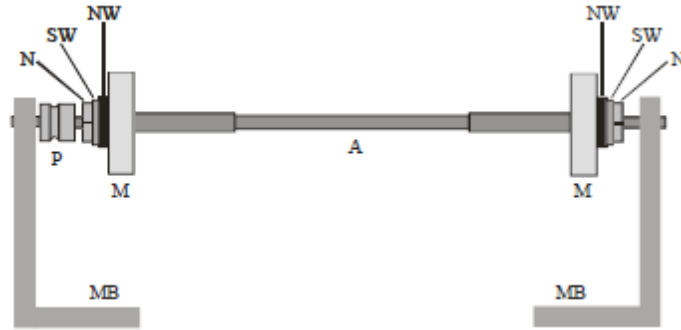


Figure 2-5 Axle and mount assembly of the P1 prototype. A (axle), M (mirror), MB (mount base), N (nut), NW (neoprene washer), P (brass drive pulley), SW (steel washer). Image taken from Reference 1.

A neoprene rubber O-ring was used as the drive belt between the axle and a high-speed rotary drill that was held by a pair of steel mounts. A variable-gain PMT was used for detection.

The optical layout of the P1 VPCS is shown in Figure 2-6. As discussed earlier, the coatings of alternating high and low refractive index material were applied to the mirrors in one-quarter wavelength layers. The Fresnel reflections that occur at the interface between the high and low refractive index creates constructive interference after a 180° phase change. If the incoming light strikes the surface of the mirror at or close to perpendicular, then the layers are one-quarter wavelength thickness and the mirrors become highly reflective. However, if the incident angle increases, the light no longer travels the one-quarter wavelength through the alternating dielectric layers. Therefore, the reflectivity of the mirrors decreases because less constructive interference occurs. Additionally, the non-perpendicular angles also increased divergence of the beam at each mirrored surface.

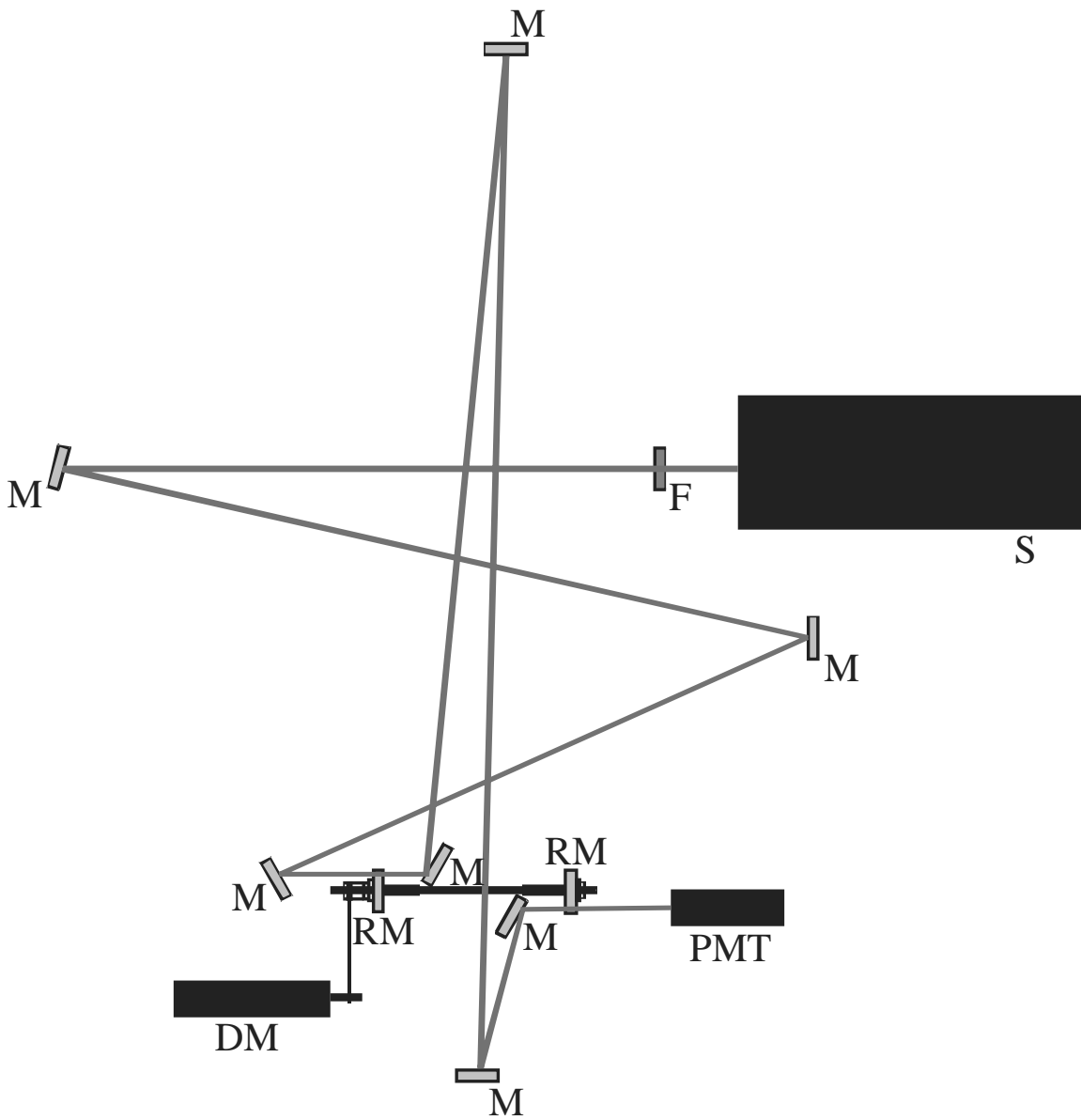


Figure 2-6. P1 VPCS optical layout. DM (drive motor), F (filter), M (mirror), PMT (photomultiplier tube), RM (rotating mirror), S (source). Image taken from Reference 1.

stable signal. To correct this problem, a black acrylic paint was applied to the rear faces of the mirrors to prevent the light from continuously being injected into the cavity.

For diagnostic purposes, the beam was projected onto a distant surface during alignment as a means to more sensitively monitor the progress of the alignment. If aligned, one would expect the beam to produce a single point. However, the projected beam was observed to produce a circle. To help correct this issue, the alignment hubs of the rotating mirrors were designed (Figure 2-8) to permit adjustments to the positions of the mirrors that were mounted on the axle. The two small Delrin hubs were each held in place on the axle by three set screws. Each hub had three nylon-tipped screws that ran parallel to the axle to maintain contact with the surface of the mirror. These screws were adjusted to ensure the mirrors on the axle were perpendicular to each other. This was done by adjusting the screws to minimize the “circle-forming” during manual alignment of the instrument.

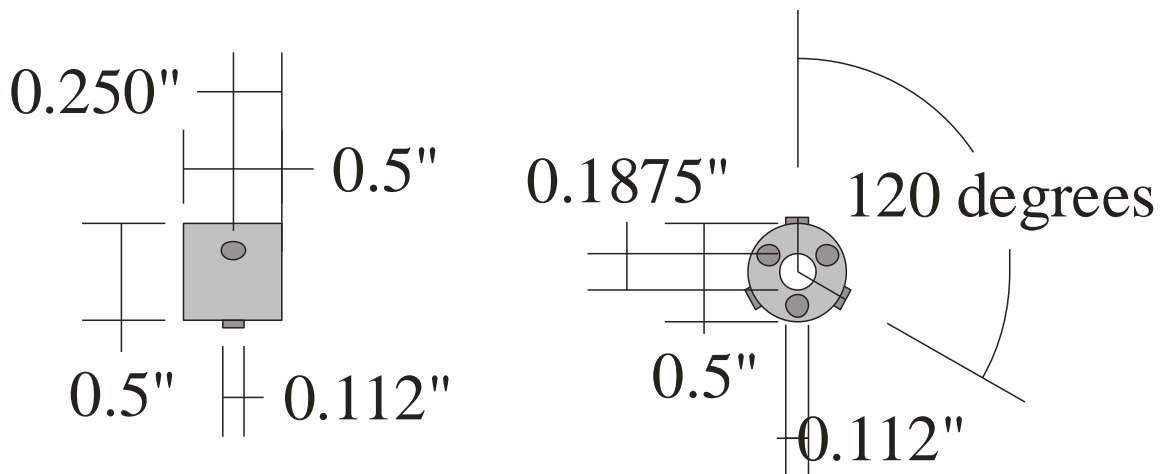


Figure 2-8. Specification for the hubs used for aligning the rotating mirrors. Three set-screws were used to hold the Delrin hubs against the axle. The other three set-screws were nylon-tipped because they were in contact with the mirrored surfaces. Image taken from Reference 1.

2.2.3. VPCS Prototype 3

For the P3 prototype, the primary change to the P2 prototype was the design of the axle mount assembly. A major drawback of the P2 prototype was that the new rotating mirror alignment hubs did not reduce vibrations to a tolerable degree. Three sources of vibration were identified.

First, the holes in the mirrors for the axle were slightly off-center, which in combination with a long unsupported axle (Figure 2-9), created a large amount of vibration. Secondly, the neoprene drive band which connected the motor to the axle was another contributor to vibration. The pulley was located in very close proximity to the mirror and was on a portion of the axle where the diameter was only 3 mm. The third contributor was the “L-shaped” axle mounts. When the axle mounts were secured, the fittings rotated slightly which put an uneven pressure on the bearings. Not surprisingly, this had adverse consequences for maintaining the precise and stable alignment of the mirrors.

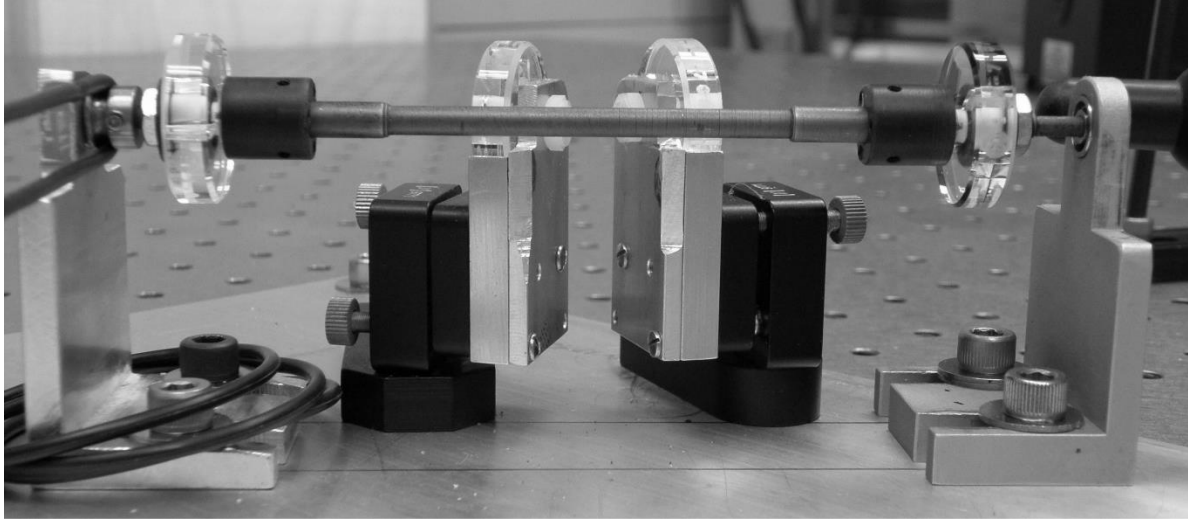


Figure 2-9 The P2 axle mount assemble. The unsupported axle, the weak “L-shaped” axle mounts, and the drive band not being separated from the mirrors lead to observable vibrations. Image taken from Reference 1.

These three problems were addressed in the P3 prototype by completely redesigning the mount as shown in Figure 2-10. The new mount replaced the separate supports of previous prototypes with a single-piece mount with four vertical supports. Each vertical support contained a sealed ABEC-5 high speed bearing rated for more than 60,000 RPM (1 kHz). The mount and axle were constructed from CrMo steel, which is known for its strength and vibration dampening. The drive pulley was separated by two supports to isolate the possible vibrations caused by the motor on the axle. The base of the mount was 2.85 cm thick and each support was more than 1 cm thick. Once the bearings were mounted, and the axle was securely in place, the supports were then affixed to the base. These supports were recessed into the base and held secured to the base by two screws that passed through the bottom of the base into the supports, thereby increasing the rigidity of the mount. With the base fully

assembled, it was secured to the optical table with 12 screws. The large mass of the base (> 2 kg) secured to the optical table ensured the maximum degree of vibration dampening.

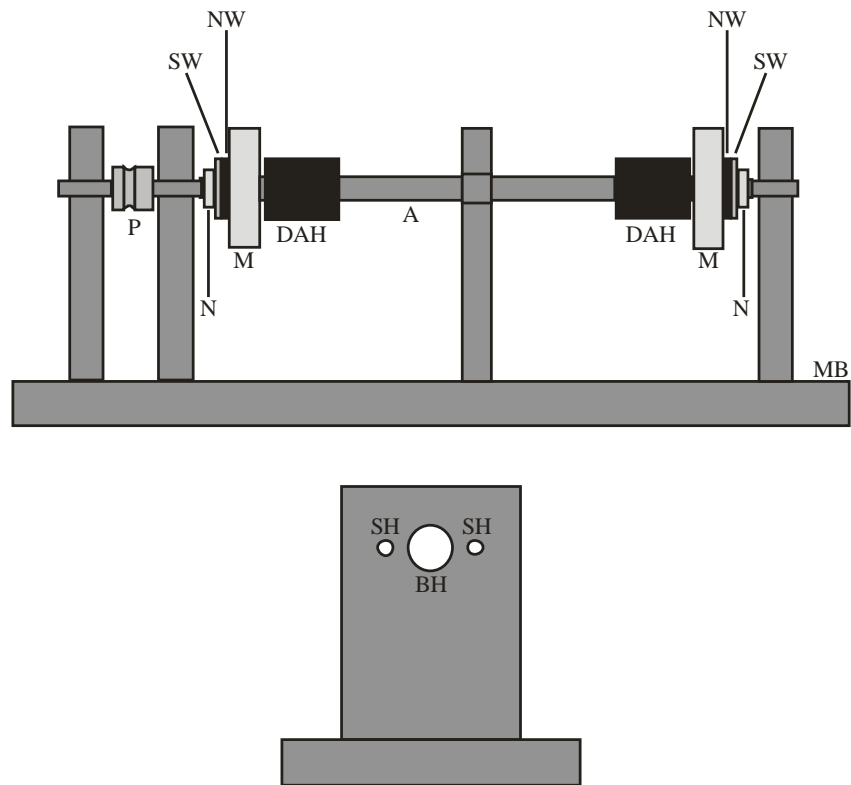


Figure 2-10 Schematic diagram of the assembly of the P3 prototype axle mount from the side view (top) and end view (bottom). A (axle), BH (bearing hole), DAH (Delrin alignment hub), MB (mount base), M (mirror), MB (mirror bushing), N (nut), NW (neoprene washer), P (brass drive pulley), SH (source hole), SW (steel washer). Image taken from Reference 1.

2.2.4. VPCS Prototype 4

Prototype 4 also involved some major changes compared to the previous design. One issue that was observed in testing was the divergence of the beam as it would traverse the cavity. Although all collimated sources exhibit divergence to some degree, the extent that was observed in the P3 prototype was unacceptable. To better understand the situation, a “ray tracing” software program was used (Figure 2-11 and 2-12). Figure 2.11 is a representation of the optical cavity in the P3 prototype using a source with a beam size of 0.69 mm and a divergence of 0.9 mrad. In this configuration, the light would only be able to make three passes through the cavity before it would extend beyond the edge of the mirror. Figure 2.12 used the same optical layout except that two flat steering mirrors were replaced with concave mirrors that had a radius of curvature (ROC) of 1 m. The use of such mirrors was tested on the instrument and as expected it proved beneficial in reducing the degree of divergence – in fact, a focusing effect was achieved. The beam spot projected onto the exit mirror was reduced to less than its diameter at the source, with no observable increase in the beam diameter after several round trips.

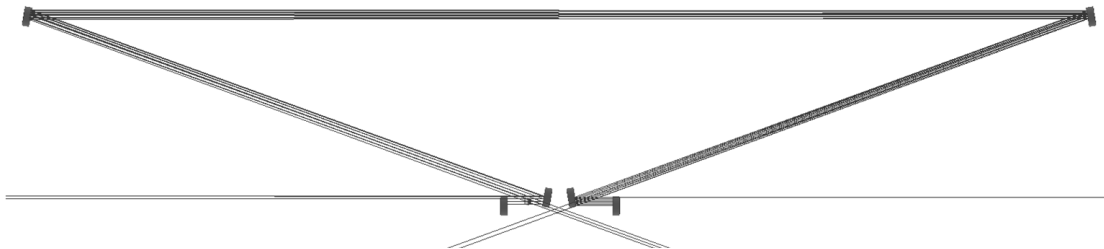


Figure 2-11 Ray diagram of the optical cavity using flat steering mirrors. If only flat mirrors were used the beam quickly "walked out" of the cavity. Image taken from Reference 1.

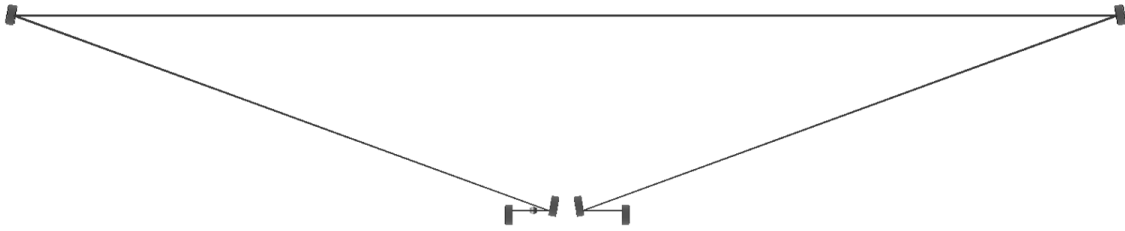


Figure 2-12 Ray diagram of the optical cavity using concave (ROC = 1 m) steering mirrors. The divergence of the beam within the cavity was negligible. Image taken from Reference 1.

Another issue that was overcome in the P4 design stemmed from issues that were observed when the light entering the cavity would interact with the edge of the mirror slits. Because alignment was accomplished when the mirrors were not rotated, this problem was not readily apparent. Of course only a very small fraction of the source light ($\ll 1\%$) is trapped within the cavity – specifically, the last “slice” reflected by the trailing edge of the entrance slit. This interaction with the rough edge of the entrance slit caused the beam to deflect several degrees, which resulted in the beam entering the cavity no longer perpendicular to the rotating mirror faces. The slits in the mirrors were fabricated by conventional machining of the glass substrate. Figure 2-13 is an image from a scanning electron microscope at 30-fold magnification that reveals the roughness of the edges of the slit.

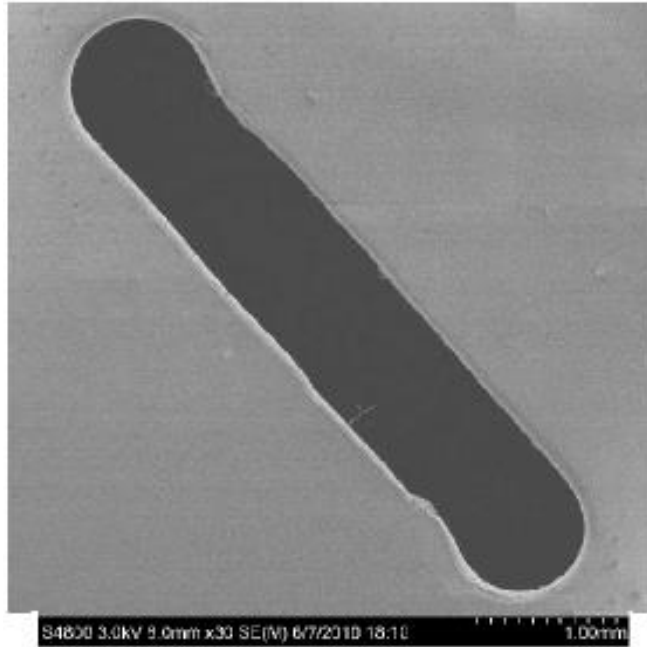


Figure 2-13. Electron micrograph of a slit in a dielectric mirror (30-fold magnification). Image taken from Reference 1.

This turned out to be a fatal flaw in the use of an entrance mirror with a slit milled into it. Imperfections in the slit geometry, however, were not a significant concern for the exit mirror as the PMT has a large photo-cathode surface in close proximity to the exit of the cavity.

It was decided that the best option was to inject the light into the cavity in the same manner as used in CRDS. Because a significant fraction of the light will pass through the backside of an entrance mirror, a CW source will not work in this approach. Therefore, a pulsed laser replaced the CW laser.

With the primary source changed to a pulsed tunable dye laser, a secondary laser was added to aid in the alignment of the cavity. The second laser (CW, 532 nm) was made collinear to the primary source by using a reflection grating. To ensure co-linearity, both sources were

reflected from the grating and sent to the first steering mirror. The beams were then projected several meters onto a flat surface. Both sources were collinear if they struck the reflection grating at the same spot across the room. Once the two sources were collinear, the primary laser was turned off and the secondary CW laser was used to align beam within the cavity. Because the wavelength of the secondary laser (532 nm) was different from the optimal wavelength of the high-reflectivity mirrors (488 nm with approximately ± 10 nm for optimal performance), more light passed through the entrance mirror and thus made visual alignment of the cavity easier to perform. Figure 2-14 illustrates the optical layout of the P4 prototype, which includes a third laser to monitor the frequency of the rotating mirror. This simple CW laser (HeNe, 632 nm) is 180° relative to the primary beam path to continuously measure the rotational speed of the exit mirror.

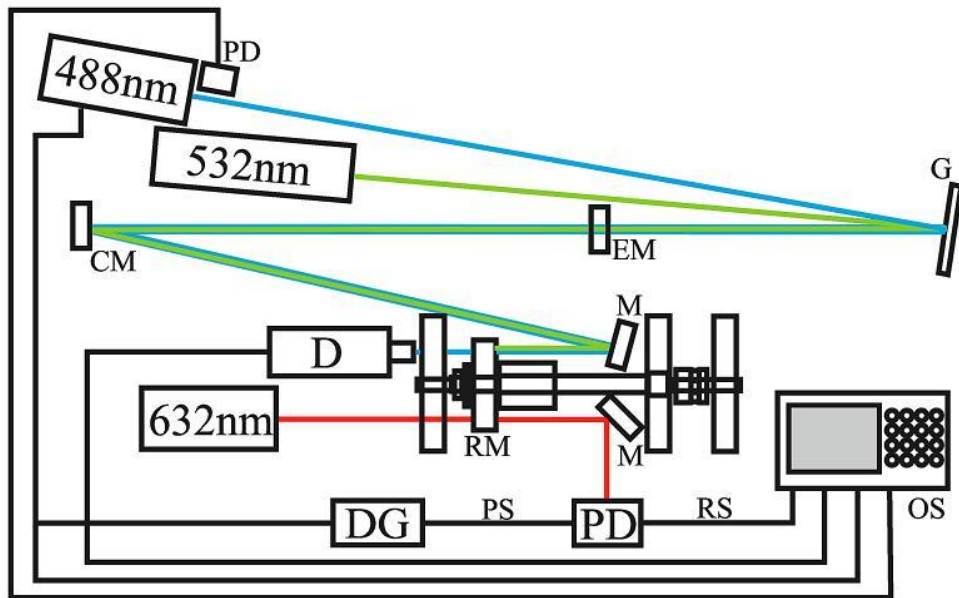


Figure 2-14. Schematic diagram of the P4 prototype. CM (concave mirror), DG (delay generator), EM (entrance mirror), G (diffraction grating), M (mirror), OS (oscilloscope), PD (photodiode), D (photomultiplier tube), PS (processed signal), RM (rotating mirror), RS (raw signal). Image taken from Reference 1.

2.3.VPCS P4 Testing

For the P4 prototype, a relationship between angular offset and transmittance at a given rotational speed was defined (Figure 2-15). The flat part on the top of the curve represents single pass measurements. Because the width of the beam is much smaller than the width of the slit (~0.1 mm beam vs. ~10 mm slit) the full intensity of the laser is reaching the detector. The asymmetry of the curve represents trapping and non-trapping situations. The light that is present on the non-trapping side is primarily attributed to the beam being “sliced” as the slit moves into the beam path. Additionally scattered light may contribute as well due to imperfections in the slit edge. Thus the angular offset approaches zero as a larger segment of the beam passes through the slit. The positive angular offsets show that the decay of the

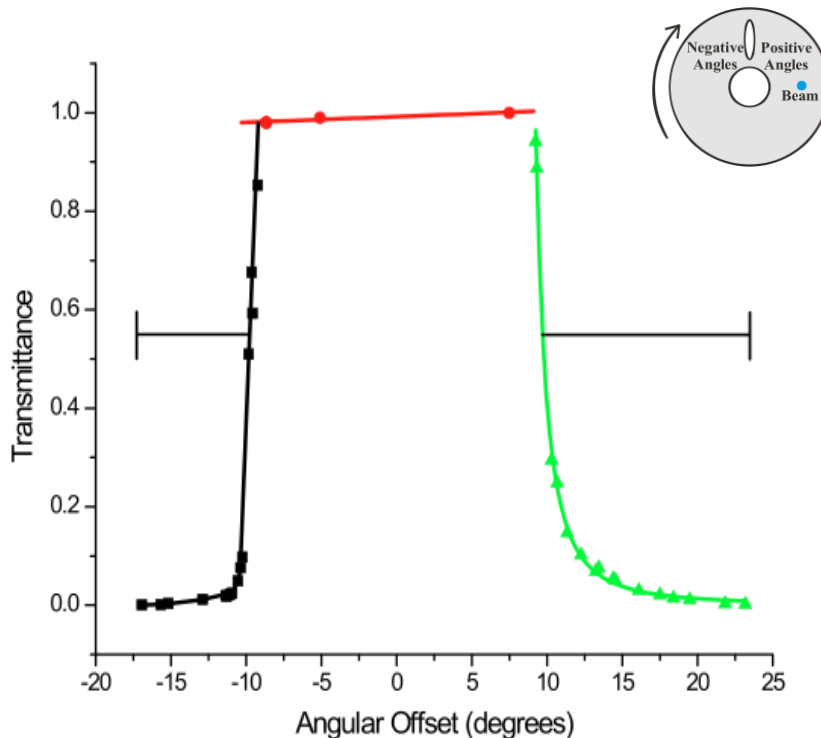


Figure 2-15 The dependence of the cavity transmittance on the angular off-set. Negative values are those in which the exit slit has already passed the beam position and no trapping is possible. Image taken from Reference 1.

transmitted light is occurring more slowly, therefore light is being trapped in the cavity before exiting through the slit and reaching the detector.

The P4 prototype also demonstrated that the theoretical relationship between the rotational speed and the transmittance also held true. Figure 2-16 compares the profiles recorded for rotational speeds at ten thousand and fifteen thousand revolutions per minute. The response has the same general features as shown in Figure 2-15. A key difference is the transmittance that was observed on the trapping (right) side of the response (shown in green in Figure 2-15). A higher transmittance at a given angular offset occurs at a higher rotational speed. This agrees with the theory that if the mirror rotates faster, there is less time for the light to traverse the cavity and lose energy.

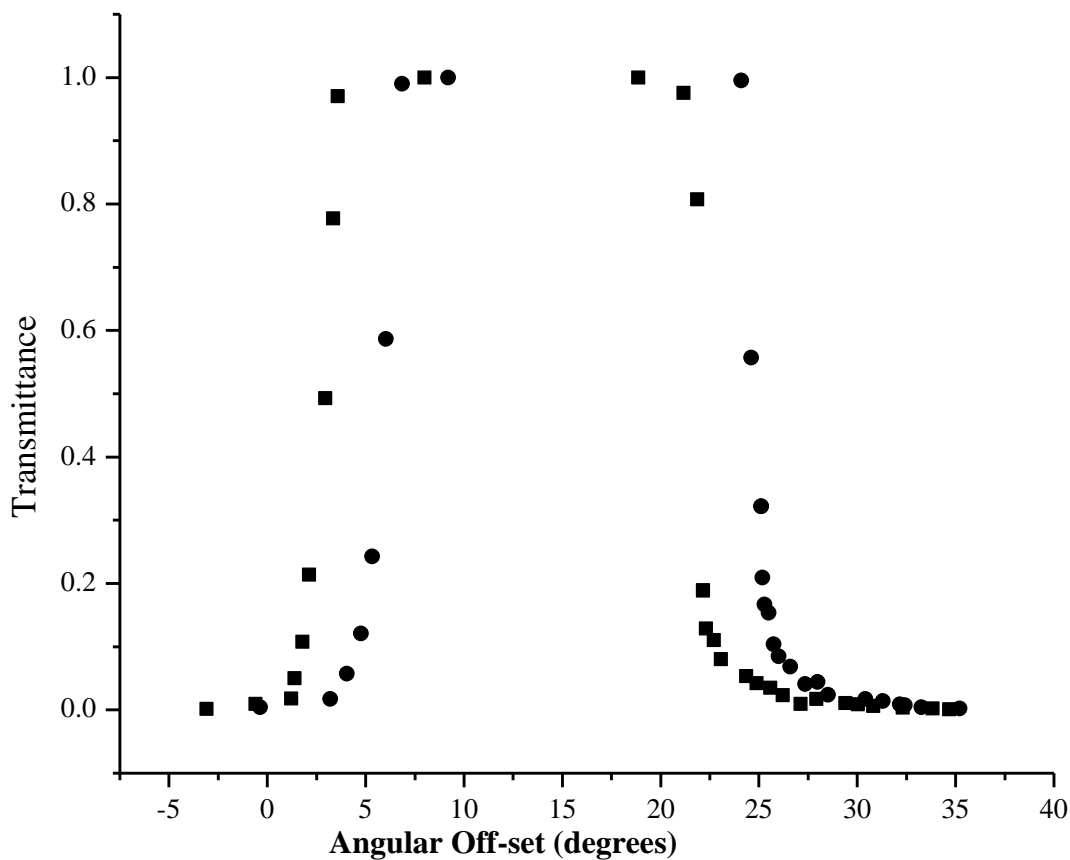
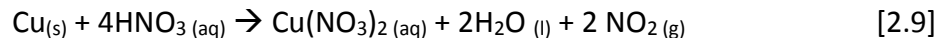


Figure 2-16. VPCS response profiles at 10 (▪) and 15 (•) krpm showing the shifting of the curves to higher angular off-sets. Image taken from Reference 1.

After the characterization of the VPCS and proof that trapping occurs, the next step was to determine the pathlength enhancement (b^*). Nitrogen dioxide was chosen as the analyte because it has an almost continuous absorption band from the UV through the VIS,³ it is available commercially in high purity or easily produced in the lab, and it is of interest in atmospheric pollution monitoring. For the initial measurements, commercial NO₂ permeation tubes were not high enough in concentration to use in a single-pass absorption measurements for comparison to the P4 VPCS prototype. Therefore NO₂ was generated using the following reaction:



Nitric acid was added dropwise to copper shavings, and the gas generated was split between the photodiode array (PDA) for single-pass measurements and the VPCS instrument, the gas was introduced into the beam path using the jet assembly shown in Figure 2-17.

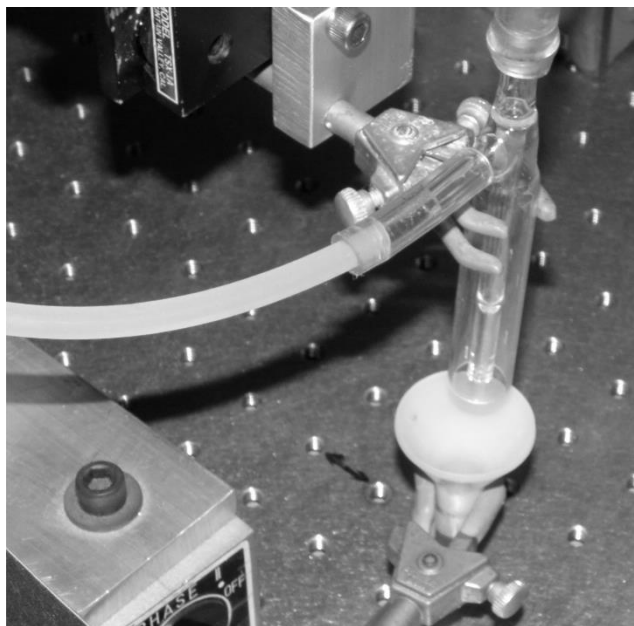


Figure 2-17 Photograph of the gas introduction jet. The $\text{NO}_2(g)$ entered from the top of the jet and the sweep gas (air) entered from the tube protruding from the side. The $\text{NO}_2(g)$ passed through the optical path of the VPCS and then was collected by the white funnel positioned under the beam path (which was under a slight vacuum). Image taken from Reference 1.

The PDA spectrometer monitored 488 nm and the spectra were averaged over the time required to collect 300 traces with the VPCS. The data was compared between the PDA and the VPCS with and without the $\text{NO}_2(g)$ present to determine the absorption enhancement of the VPCS. The transmittance was plotted vs angular offset as shown in Figure 2-18.

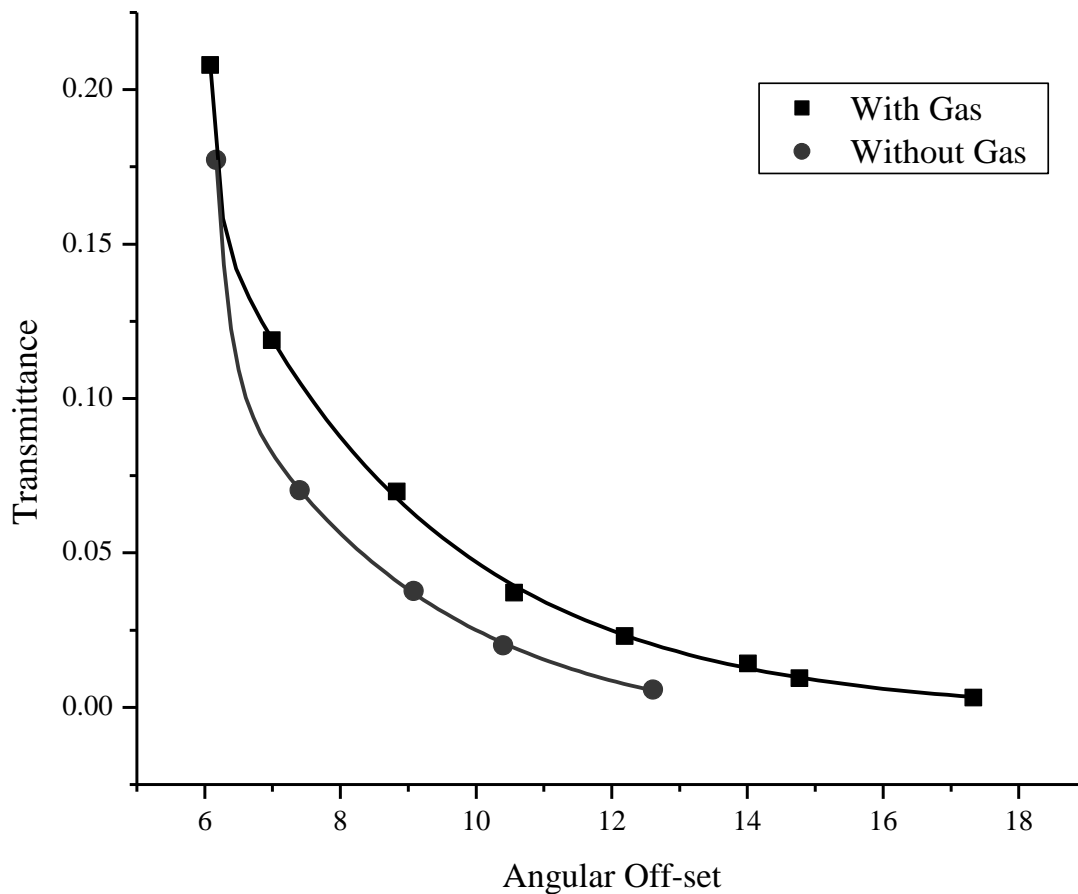


Figure 2-18 Transmittance at 488 nm of the P4 prototype VPCS response with and without $\text{NO}_{2(g)}$ present as a function of angular off-set. Data was collected as a constant rotational speed of 10 krpm

For a $\text{NO}_{2(g)}$ concentration of 1.28 mM, an enhancement of 53 times was observed vs the single-pass measurement. The data shown in Figure 2-18 were fitted to regression curves which were used to calculate the absorption at specific off-set angles, as shown in Figure 2-19.

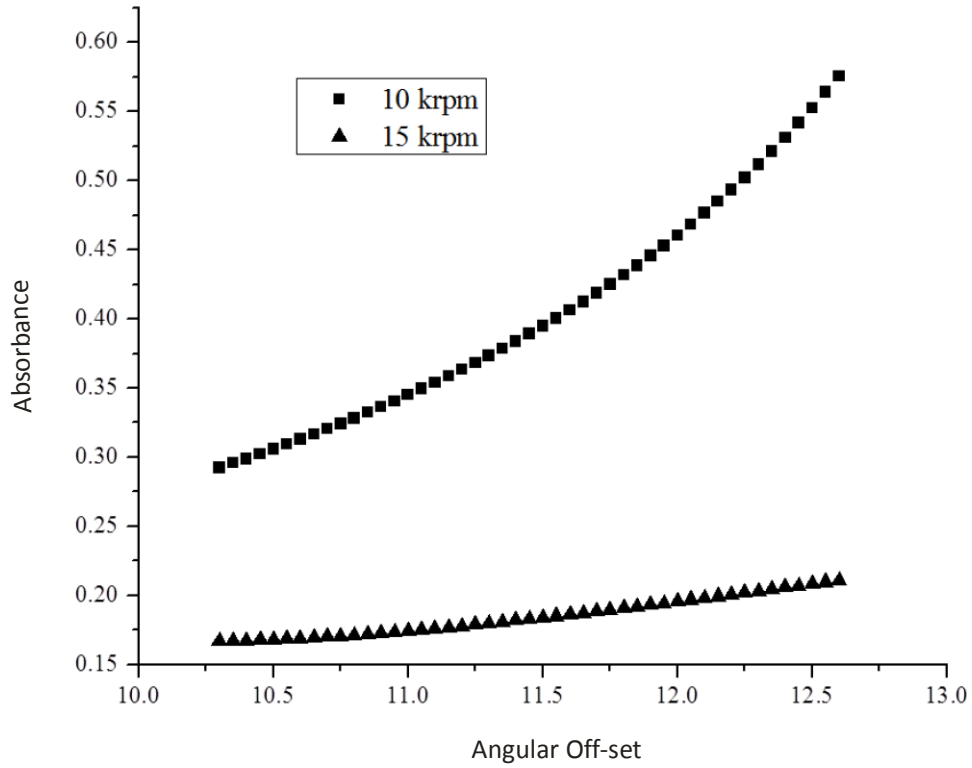


Figure 2-19 An example of the VPCS absorption as a function of angular off-set calculated from the fitted regression curve at 10 and 15 krpm.

The VPCS data from Figure 2-19 was compared to that from the single-pass measurements to calculate the enhancement factor (b^*). The calculated enhancement factor as a function of angular offset and rotational speed from the experimental data is shown in Figure 2-20.

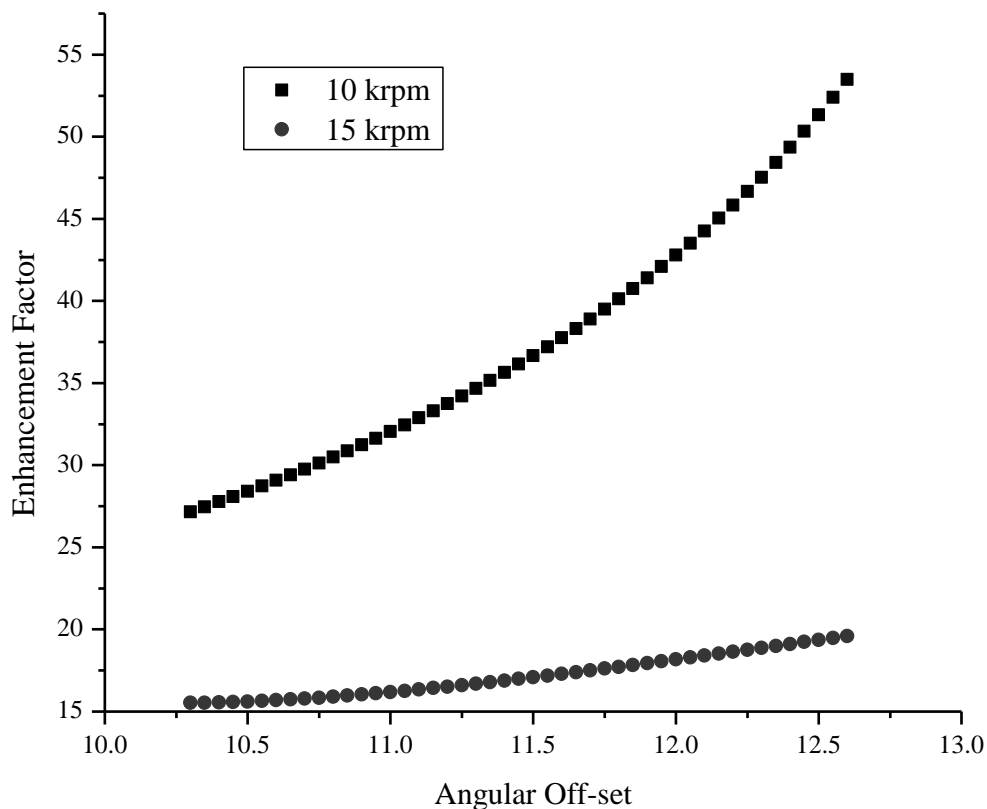


Figure 2-20 Enhancement factor as a function of increasing rotational speed and angular off-sets.

2.4. Statement of Thesis

The goal of the work described herein is to create an automated prototype of the VPCS (“P5”). The complete automation of the instrument control, data acquisition, and data reduction functions will be described. The automation of instrument control not only includes the components described in the P4 prototype but also a novel system for the automated alignment of the beam within the cavity. Performance characteristics of the P5 instrument will be further defined and an improvement of the enhancement factor for gas-phase samples will be demonstrated.

LITERATURE CITED

1. Frost, J. A. Photon Trapping Spectroscopy: A novel Extended Pathlength Spectroscopic Technique. University of Wisconsin-Milwaukee, Milwaukee, 2011.
2. Ruddy, B. Studies in Gas Chromatography-Tandem Mass Spectrometry and Absorbance Spectroscopy for the Determination of Polychlorinated Biphenyls in Freshwater Biota. University of Wisconsin-Milwaukee, Milwaukee, 2006.
3. Atkinson, D. B., Solving Chemical Problems of Environmental Importance using Cavity Ring-Down Spectroscopy. *The Analyst* **2003**, (128), 9.

3. Experimental

3.1. Generation of Gas-phase Analyte

In previous work with the instrument, a system was designed for generating nitrogen dioxide by chemical reaction.¹ In this method, shown schematically in Figure 3-1, a separatory funnel was used to add concentrated nitric acid drop-wise to copper shavings. The resulting NO₂ production varied widely over time, however. The inconsistent flow of nitric acid through the separatory funnel to the copper shavings caused variation in the production of NO₂. In the previous work, this problem was partly overcome by averaging 300 measurements, as well as simultaneously monitoring the NO₂ from a split line by off-line molecular absorbance spectroscopy. To improve upon this approach, in the present work NO₂ was generated by the use of a certified standard (Praxair, Milwaukee, WI, USA). The lecture-size bottle had a certified concentration of 160 parts per million by volume (ppm_v) that was certified to be ±5% in accuracy. Generation of the NO₂ test analyte in the gas-phase was thus more accurate, stable, safer, and more convenient for each measurement.

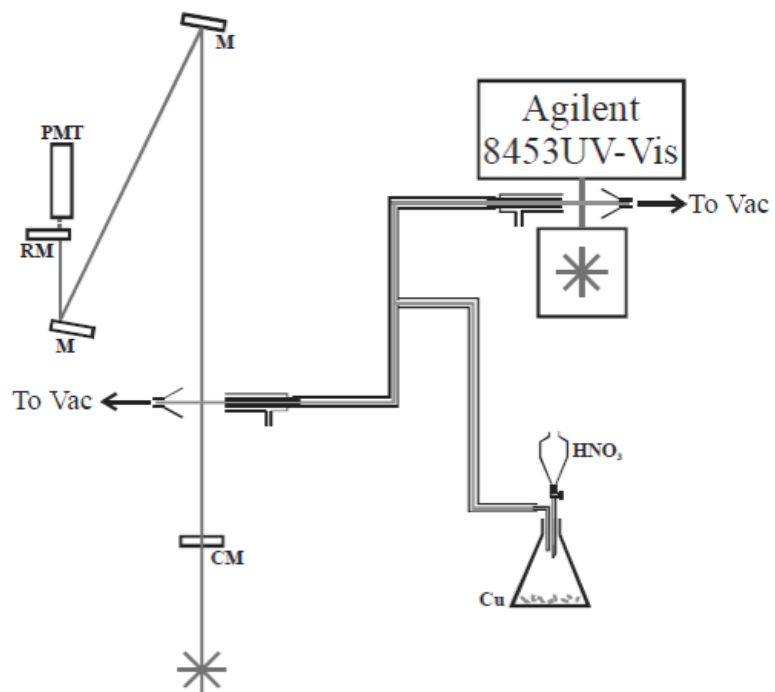


Figure 3-1. Schematic diagram of the Nitrogen Dioxide generator. The VPCS is depicted at left (M = fixed flat mirror, RM = rotating mirror, CM = fixed concave mirror, PMT = photomultiplier tube detector).

In the NO_2 testing apparatus, the single-pass measurements were made with an ultraviolet-visible-near infrared (UV-VIS-NIR) Molecular Absorbance Spectrophotometer (Model 8453A, Agilent Technologies Inc., Santa Clara, CA, USA), shown in Figure 3-2. Data was recorded using the Agilent ChemStation software (Rev. A. 10.01).

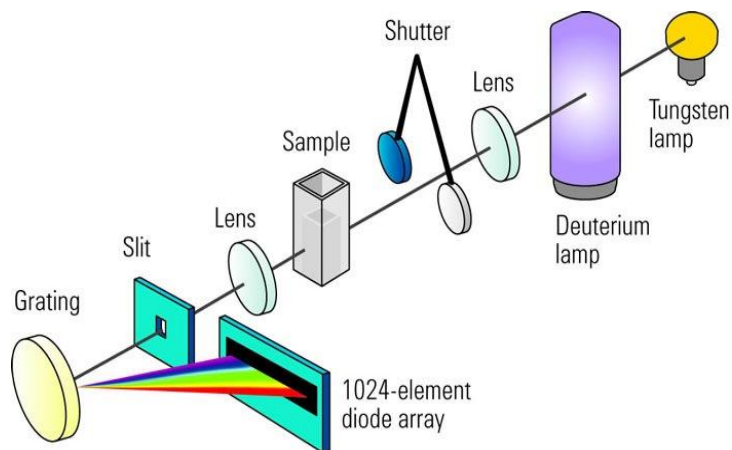


Figure 3-2. Schematic diagram of the Agilent Photodiode Array Spectrophotometer. Diagram taken from Reference 2.

Wavelength range	190-1100 nm
Resolution	1 nm
Wavelength accuracy	< 0.5 nm
Wavelength repeatability	< 0.2 nm
Photometric accuracy	< 0.005
Photometric noise	< 0.00002
Baseline flatness	< 0.001

Table 3-1. Specifications of the Agilent Photodiode Array Spectrophotometer.²

3.2.VPCS Instrument Design

3.2.1. Optics

A total of four prototypes had been developed prior to the present work.¹ The fifth prototype, hereafter referred to as “P5”, was developed in this work. In the P5 system, the primary light source for the measurement was a pulsed dye laser (Model PL-201, maximum average power 56 mW, Photon Technology International, Birmingham, NJ, USA) that used Coumarin 481 dye at 0.01 M in *p*-Dioxane (Exciton, Dayton, OH, USA).¹ The dye laser was

pumped by a Nitrogen laser (Model GL-3300, Photon Technology International); the specifications are listed in Table 3-2. The tunable primary laser was monitored by using a photomultiplier tube (PMT) detector (Hamamatsu, Model H5784, Hamamatsu, Japan) with variable gain adjustment.

Type	N ₂ -Pumped Dye
Pulsed or CW	Pulsed
Wavelength	Variable
Max Pulse Energy	2.8 mJ
Spectral Bandwidth	0.1 nm
Beam Dimension at exit	3 x 6 mm
Beam Divergence at exit	3 x 7 mrad

Table 3-2. The key specifications for the Nitrogen Laser Model GL-3300.³

To more precisely align the primary source (i.e., the pulsed N₂-pumped dye laser), a secondary source was used. Specifically, a continuous wave (CW) laser (Holograms & Lasers International, 25 mW Green, Houston, TX, USA). This laser operating at 532 nm was made collinear with the primary laser by the use of a reflection grating. The typical function of a reflection grating is to cause light undergo diffraction so certain wavelengths can be selected to make spectroscopic measurements. In this application, two beams of light at different wavelengths were directed to the same point on the grating, with different incident angles. After precise alignment of the incident beams, the two beams were reflected by the grating traveling the same path, i.e. they were collinear. To achieve collinearity, the entrance mirror was removed and the primary source light from the dye laser was directed to the center of the

first intra-cavity mirror. A 1 mm aperture was placed between the reflective grating and the entrance mirror to the cavity. The beam spot from the primary laser was then projected across the lab (~10 feet) by using a flat mirror. The secondary CW laser was then turned on and alignment of the two beams was carefully adjusted. The secondary CW laser was considered to be sufficiently aligned when the incident light from it would strike not only the same spot on the grating as the primary laser but also, after being projected across the room, the same spot on the wall ~10 feet distant. Once the center of the beam profiles were aligned, the primary source was turned off and the cavity itself was aligned by using the secondary source. The flat entrance mirror was placed back into the beam path so the light would pass through the flat entrance mirror into the center of the first intra-cavity mirror, which was concave with a 1 m radius of curvature (ROC). The light was then reflected to the second intra-cavity mirror that directed the light to the rotating exit mirror. The cavity was aligned so that the light returning from the exit mirror would be precisely reflected back to the aperture between the entrance mirror and the reflection grating.

The rotation of the exit mirror was monitored with a continuous wave HeNe laser (JDS Uniphase, 1508P-0, Milpitas, CA, USA; the specifications are listed in Table 3-3) operating at 632.8 nm was monitored by a photodiode detector (PD) was built in-house. The PD had two outputs: the first output collected the raw PD response. The second output was used as the input signal to trigger the firing of the primary source (i.e., the N₂-pumped dye laser). The N₂ laser operated most consistently at a repetition rate of ~5 Hz. Therefore the second output of the PD was equipped with a limiting circuit, which would introduce an adjustable dead time

following the output pulse. This dead time was set to ~200 ms to achieve the 5 Hz repetition rate favored by the N₂ laser.

Type	HeNe
Pulsed or CW	CW
Wavelength	632.8 nm
Power	0.5 mW
Beam Dimension at exit	0.48 mm
Beam Divergence at exit	1.7 mrad

Table 3-3. Key specifications of the HeNe used to monitor the rotational speed of the mirror.⁴

3.2.2. Signal Processing

The signals from the PMT and the photodiode detectors were collected by the use of a 250 MS/s digitizer (Model 5761, National Instruments, Austin, TX, USA); pertinent hardware specifications can be found in Table 3-4. The digitizer is connected to a field-programmable gate array (FPGA) module (FlexRIO FPGA Model 7965R, National Instruments, Austin, TX, USA); specifications for the FPGA module can be found in Table 3-5. The FPGA module was located in the second slot position of the data system chassis (Model PXIe-1071, National Instruments). Programming was done on a controller (Model PXIe-8108, National Instruments, Austin, TX, USA) located in the first slot the system chassis; specifications for the controller can be found in table 3-6. Data reduction and instrument control were performed in LabVIEW 2012 (Version 12.0.0, National Instruments, Austin, TX, USA), with FPGA (Version 12.0.0) and Real Time (Version 12.0.0 software packages)

Specification	Analog Input
Sample Rate	250 MS/s
Resolution	14 bits
Number of Channels	4
Bandwidth (AC-Coupled)	0.1 to 500 MHz
Input Range (AC-Coupled)	2.07 V _{pk-pk} peak to peak?
Coupling	AC or DC
Input impedance	50 Ω

Table 3-4. Hardware specifics of the NI-5761 Digitizer.⁵

Features	Specification
Default time base	400 MHz
Time base reference source	100 MHz
Time base accuracy	250 ps peak-to-peak jitter
Memory size	2 banks; 256 MB per bank
Maximum theoretical data rate	1.6 GB/s per bank

Table 3-5. Key Specifications for NI 7965R FPGA Module.⁶

Features	Specification
CPU	Intel Core 2 Duo Processor T9400(2.53 GHz dual core processor), 800 MHz FSB
On-die L2 cache	6 MB
Single-channel DDR2 RAM, PC2 6400	1 GB Standard, 4 GB Maximum
Hard Drive	80 GB Serial ATA
Connection ports	GPIB (IEEE 488 Controller), Serial Port (RS-232), Parallel Port, Hi-Speed USB (2.0) Ports (4 total), PXI Trigger Bus Input/ Output
Operating System	Windows 7 Professional

Table 3-6. Specifications for PXIe-8108 controller for the VPCS system.⁷

3.2.3. Alignment

Images were captured with a charge-coupled device (CCD) camera (Model Prosilica GC, Allied Vision Technologies GmbH, Stadtroda Germany) and using a 2/3" 12-36 mm focusing lens (Model Verifocal - Manual Iris Megapixel, Computer, Commack, NY, USA). The specifics of the CCD camera are listed in Table 3-7, and the quantum efficiency of the camera's working range is shown in Figure 3-3. Light-emitting diodes (LEDs) were used (Model DEV-10754, LilyPad LED Micro, Yetda Industry LTD, Hong Kong, China) to locate the center of the first concave mirror.

Features	Specification
Interface	IEEE 802.3 1000baseT
Resolution	1360 x 1024
Sensor	Sony ICX285
Sensor Type	CCD Progressive
Max Frame rate at full resolution	20 fps

Table 3-7. Prosilica GC camera specifications.⁸

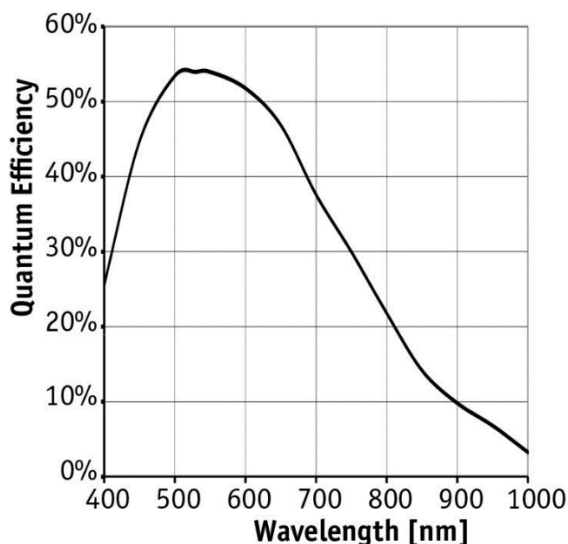


Figure 3-3. Optical performance of the CCD camera. Image taken from Reference 8.

The red LEDs had dimensions of 3.2 x 1.6 mm. A solenoid (Model SHE-T0637, Arndt Electronics, Berlin, Germany) was used to automatically control when the CW light entered the cavity during auto-alignment. The camera, placed behind the concave intra-cavity mirror, was aligned by placing an object near the surface of the mirror. The alignment of beam in the cavity was adjusted by motorized DC Servo Motor Actuators (Model Z812, Thor Labs, Newton, NJ, USA) that were controlled by two DC Servo Motor Controllers (Model T-Cube, Thor Labs, Newton, NJ, USA). The images were collected by using an Ethernet module (Model 8234 Dual Gb ports, National Instruments, Austin, TX, USA) that was located in the third slot position of the PXIe system chassis described above. The images were processed by using LabVIEW Vision Development Module software (Version 14.0.0, National Instruments, Austin, TX, USA).

Literature Cited

1. Frost, J. A. Photon Trapping Spectroscopy: A novel Extended Pathlength Spectroscopic Technique. University of Wisconsin-Milwaukee, Milwaukee, 2011.
2. Technologies, A., Agilent Cary 8454 UV-Visible Spectroscopy System Operator's Manual. Technologies, A., Ed. 2014.
3. PTI, Nitrogen Laser Operation Manual. International, P. T., Ed. Birminham, NJ, 2008.
4. JDSU, Self-Contained Helium-Neon Laser Systems. Corporation, J. U., Ed. 2012.
5. Instruments, N., NI 5761 User Guide and Specifications. Corporation, N. I., Ed. Austin, Texas, USA, 2010.
6. Instruments, N., NI PXIe-7965R NI FlexRIO FPGA Module for PXI Express. Corporation, N. I., Ed. Austin, Texas, USA, 2014.
7. Instruments, N., NI PXI-8108 User Manual. Corporation, N. I., Ed. Austin, Texas, USA, 2010.
8. GmbH, A. V. T., Technical Manual AVT GigE Vision Cameras. Technologies, A. V., Ed. Stadtoda, Germany, 2013.

4. Results and Discussion

4.1. Prototype 4 Hardware and Data Treatment

Prototype 4 was the working model that was developed and published by John Frost.¹

The major limitation of the P4 prototype was the hardware used for data collection and data reduction. To collect and reduce the data was a long process. While demonstration of trapping and applying that to gas-phase samples was demonstrated, there was no real-time feedback. The key relationships (i.e., rotational speed and angular offset) were unknown until after a full response curve worth of data was collected and reduced. This took several hours to complete. This chapter will discuss the hardware for the P4 prototype as well as the process for data reduction. Then the new hardware used to automate the P5 prototype will be introduced and the software architecture, functionality, and testing will be discussed.

4.1.1. Hardware

The timescale required to collect data from the PMT and the laser PD were significantly smaller than the time scales needed to monitor the rotating mirror channels. This required two oscilloscopes to monitor the channels at the appropriate sampling speeds. To match timestamps between the two oscilloscopes, several channels needed to be monitored on both oscilloscopes. Prototype 4 data collection was accomplished by the use of a 500-MHz oscilloscope (LeCroy, Waverunner LT 344, Chestnut Ridge, NY, USA) to collect data from the PMT, the dye laser internal photodiode, and the triggering signal. This will be referred to as oscilloscope 1 henceforth. A second 500-MHz oscilloscope (LeCroy Waverunner LT 364,

Chestnut Ridge NY, USA) was used to collect the dead-time-limited HeNe PD, the raw HeNe signal, the triggering signal, and the dye laser internal photodiode.

The PD that was in the dye laser was used to correct the timing between the two oscilloscopes. This peak has a short duration and a sharp rise time which was used to trigger the start of the data collection on oscilloscope 1 and 2 and later synchronize the data.

The signal from the HeNe PD was then directed through a switch that would interrupt the signal if the instrument was not operating. From this switch the signal was sent into a Stanford Research Systems (SRS) SR-240 50 Ω fast preamp with a gain of 5. The SR-250 output a TTL pulse that was sent to a second SR-250 to act as fine adjustment to the system. The first SR-250 was set to the 10 ms scale and the second would use the μ s scale to allow for fine adjustment to the delay of the laser. The output TTL signal was then sent back to the SR-240 before being split to oscilloscope 2 and the N₂ laser.

Table 4.1 below summarizes the settings and specifications of the oscilloscopes described above.

	Oscilloscope 1, Lecroy Waverunner LT 344	Oscilloscope 2, Lecroy Waverunner LT 364
Sampling Rate	250 MS/s	2.5 MS/s
Time per division	20 μ s	2 ms
Trigger Mode	Normal	Normal
Trigger off Channel	4	4
Trigger	0.54 V leading edge	0.856 V leading edge
Sweeps to average	300	300
Channel 1	PMT, 2 – 100 mV/div, 50- Ω terminated	Dead-time-limited HeNe PD output, 1 V/div. DC terminated
Channel 2	Not used	Unprocessed HeNe PD, 2 V/div, DC terminated
Channel 3	Triggering signal from SR-240 am, 0.5 V/div, 50- Ω terminated	Triggering signal from SR-240 am, 0.5 V/div, 50- Ω terminated
Channel 4	Dye Laser internal PD, 1 V/div, 50- Ω terminated	Dye Laser internal PD, 0.2 V/div, 50- Ω terminated

Table 4-1 Operating settings of the two oscilloscopes utilized by the P4 PTS prototype

When collecting data with the P4 prototype, the N₂-laser would be triggered externally by a TTL pulse from the SR-240 when the interrupt switch was turned on. The repetition rate of the laser was approximately 5 Hz, which was determined based on the consistency of the laser firing. As discussed below, the actual rotational speed was calculated post-data collection. With the rotational speed fixed the other factor that could be controlled was the angular offset. The angular offset was also determined post-data collection. During the data collection the sweeping of the angular offset was done by adjusting the SR-250's 1 ns to 10 ms scale and ten-turn potentiometer control.

4.1.2. Data Collection and Treatment

The data files were processed using both Microsoft Excel 2003 SP3, and Origin Pro 7.0 SR0. Four channels were required to monitor for the use of PTS Prototype 4. The data collections were averaged for 300 sweeps on the oscilloscopes. An example of the data observed is shown in Figure 4-1.

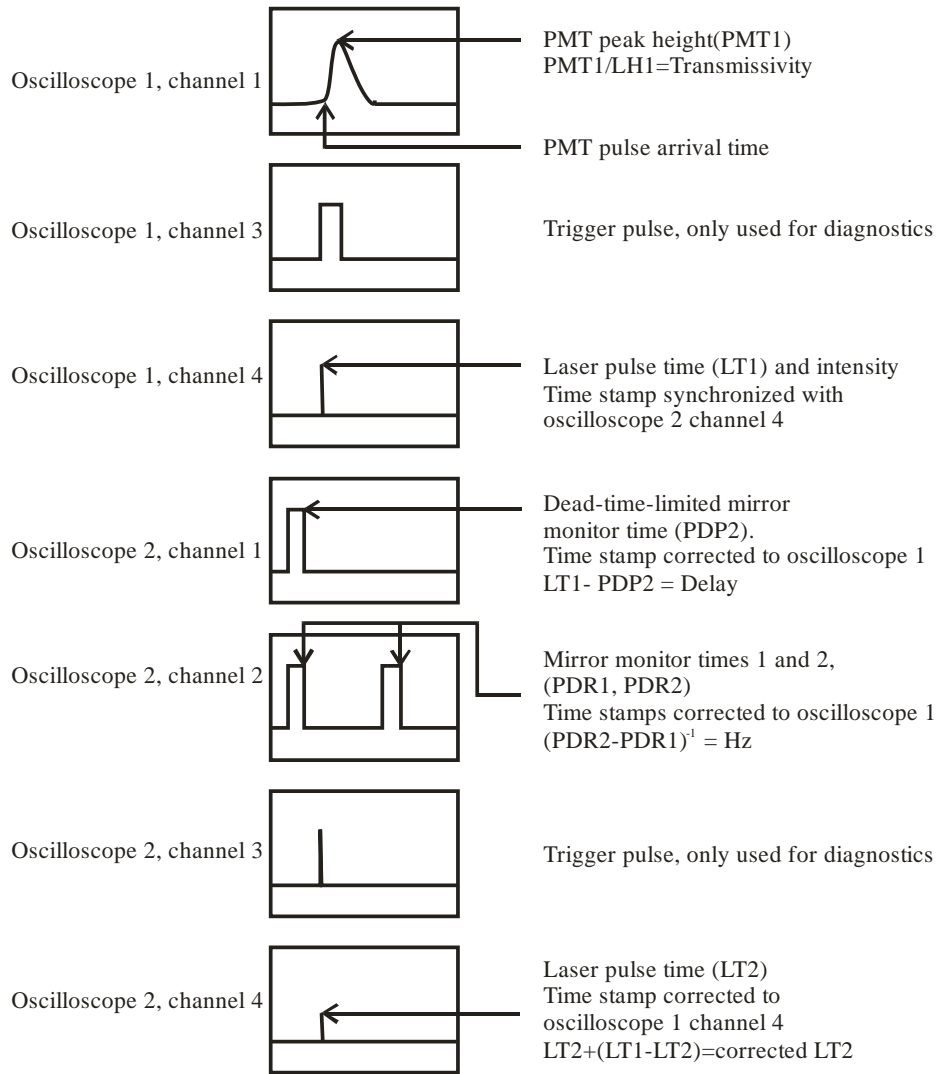


Figure 4-1 Description of oscilloscope channel signals and the selection of the data points relevant to the calculations. Image taken from Reference 1.

The rotational speed and the triggering signal was monitored at 180° to the primary laser beam path. The rotational speed was monitored with a continuous wave (cw) HeNe laser operating at 633 nm with the response measured using a fast photodiode detector (PD) and recorded on channel 2 of oscilloscope 2. There were two outputs to the PD, the raw signal and the “dead-time” signal. The trailing edge of the peaks were used to calculate the rotational speed by taking the reciprocal of the difference in the trailing edge timestamps of two adjacent peaks.

The second output, or dead-time signal, was used as the input to trigger the N₂-pumped laser as discussed earlier. The dead-time signal was sent to a switch that the operator could toggle to interrupt the pulsed N₂-laser from firing. From the switch, the dead-time signal was directed to a Stanford Research System (SRS) SR-240 50 Ω preamp with a gain of 5. The signal was then split, with one sent to oscilloscope 2 and the second sent to a SRS SR-250 gated integrator and boxcar average input. After being “triggered” the SR-250 outputs a TTL pulse which can be delayed from 3 ns to 100 ms by use of the SR-250’s 1 ns to 10 ms scale and ten-turn potentiometer controls. This TTL pulse was then sent to a second SR-250 set to μs scale to provide fine adjustment to the system. The “busy” output TTL signal, or triggering signal, was split and sent to external trigger input jack on the N₂-laser. The second line was directed to oscilloscope 2 and used only for troubleshooting. The time difference between the trailing edge of this peak was subtracted from the laser pulse time to determine the delay.

The peak intensities were manually located by finding the maximum value in Origin Pro 7.0. The data points were transcribed to Microsoft Excel and time corrected for the difference

between the two oscilloscopes. This was done by subtracting the time stamp of the laser signal of one oscilloscope from the other and adding the difference to the smaller of the two laser original time stamps. Once the data from all channels were collected, transferred, and time corrected the mathematical manipulation could be done to determine the transmissivity, the rotational speed of the rotating mirror, and the angular offset of the exit slit at the time the laser was fired.

The angular offset in degrees was found by solving Equation 4.1:

$$\theta = \theta_{\text{HeNe:Dye}} - (t_{\text{laser}} - [T_{\text{HeNe}} - (T_{\text{W}_{\text{HeNe PD}}}/2) - (T_{\text{W}_{\text{slit}}}/2)] \cdot f \cdot 360) \quad [4.1]$$

In this equation $\theta_{\text{HeNe:Dye}}$ is the angular displacement between the center of the HeNe and Dye lasers, T_{HeNe} is the timestamp of the trailing edge of the HeNe peak as measured by the PD, $T_{\text{W}_{\text{HeNe PD}}}$ is the temporal width of the HeNe PD peak, $T_{\text{W}_{\text{slit}}}$ is the temporal width of the slit, and f is the rotational speed of the exit mirror in Hz.

The PMT detector measures the signal from the primary laser and is registered on channel 1 of oscilloscope 1. The peak intensity value and corresponding time of the data point were transferred to Microsoft Excel. The baseline value was also recorded in Excel and the PMT peak intensity was corrected for that value. The transmissivity of the cavity was calculated by using the ratio of the PMT signal peak height to the peak height from the laser PD.

4.2. Prototype 5 Hardware and Data

Analyzing the results obtained with P4, it was determined that to better understand the operation of the instrument and to thereby increase the pathlength enhancement factor a more efficient way of collecting and reducing the data was required. While the work done with

Prototype 4 was able to demonstrate that trapping occurred and that a gas-phase measurement was possible, there was no way to determine key relationships like angular offset and rotational speed until the full curve was collected and analyzed. Unfortunately it would require several hours to collect and reduce the data. A new system with real-time feedback would allow for a better understanding and characterization of the instrument. With a grant from the University of Wisconsin-Systems (WiSys) Applied Research Grant Program, the data collection hardware was upgraded for a more automated method for analysis.

4.2.1. Prototype 5 Hardware

A primary goal of the P5 re-design phase of the project was to simplify the data processing method by completely automating it. For example, as described in Section 3.1, two oscilloscopes were used in the P4 instrument design because of differences in the timescales for the photon detection and laser-firing measurements, i.e., each needed a separate data acquisition channel. Therefore in the new design, a single platform for multiple data streams was selected. The platform was selected to perform the required functions in parallel and in real-time.

Of course the P5 system had to possess the same (or better) performance characteristics than the P4 system. To meet the parameters required to match the functionality of the P4 system, there are four major components in the P5 design: the PXI Chassis, the FPGA Module, the Digitizer Module, and the Embedded Controller.

PXI Chassis

The PXI chassis (NI 1071) is the backbone of the system. Each device has direct access to the shared bus, i.e., each has its own “lane” to transmit data up to 250 MB/s (sending or receiving). PCI Express software allows for faster data rates than the previous PCI version used in the P4 system.

FPGA Module

The Field-Programmable Gate Array (FPGA) is a re-programmable silicon chip wherein each processing task is assigned to a different portion of the chip. Because there is no interaction between logic blocks on the chip, tasks do not compete with one another for the same resources (e.g., memory space). Thus the FPGA (NI 7965R) allows the I/O to be controlled at the hardware level, thereby providing faster response times with specialized functionality to meet the requirements of the application.

Digitizer Module

The Digitizer Module (NI 5761) collects the analog data for processing by the FPGA. The module has four analog input channels with 14-bit resolution as well as eight digital I/O channels. The analog bandwidth is 500 MHz with a sampling rate of 250 MS/s.

Embedded Controller

The Embedded Controller is the on-board computer, with Windows 7 Professional, LabVIEW® 2012 (base package), and LabVIEW Real-Time® installed in the controller. The drivers for the FPGA and the Digitizer Modules are also found on the controller.

4.2.1.1. PXI Chassis

Peripheral Component Interconnect (PCI) platform systems are rugged PC-based platforms that are used for modular measurements and automation. This is attained by having a chassis that connects the modules via a backbone (group of electrical connectors in parallel to each other) to a shared bus (channel or path between the components in a computer). PCI buses became a mainstream computer bus in the mid-1990's with common operation at 33 MHz and 32 bits with a bandwidth of 132 MB/s². These have a shared bus, and over time devices have taken more of the bandwidth of the bus. The PCI express was then developed which used a point-to-point topology, meaning that the components are directly connect to each other. This system uses a shared switch versus a shared bus of the original PCI systems. This now allows each device on the backbone to have direct access to the bus with its own 'lane' to transmit up to 250 MB/s sending or receiving per lane. PCI express allows for faster data rates than the previous PCI. PXI (PCI eXtensions for Instrumentation) was developed and launched in the late 1990's. The PXI platform has the same features of PCI systems with the addition of specialized synchronization busses. PXI is governed by the PSI Systems Alliance (PXISA). A PXI system consists of three parts, the chassis, the controller, and the module(s).

The chassis is the backbone to the system. It provides power, cooling, and communication buses of the PXI system. The chassis that was chosen for this project is NI's PXIe (PXI Express) NI-8108. This is a 4-slot compact desktop chassis that is 8.43 in x 10.12 in x 6.97 in. The bandwidth available to each slot is 1 GB/s for a total system bandwidth of 3GB/s. For PXI modules there is a 10 MHz reference clock with an accuracy of ± 25 parts per million (ppm), less than 5 ps (10^{-12} sec) jitter and a maximum slot-to-slot skew of 250 ps. For PXIe

modules there is a 100 MHz reference clock with an accuracy of ± 25 ppm, less than 3 ps jitter, and a maximum slot-to-slot skew of 100 ps.



Figure 4-2 Example of a PXIe system with the PXIe NI-1071 chassis. Image taken from National Instruments.

4.2.1.2. FPGA Module

Field-Programmable Gate Array, or FPGA, are reprogrammable silicon chips and were invented in 1985³. FPGAs provide hardware-timed speed and reliability of application-specific circuit (ASIC) and process-based systems but do not require the custom design of ASICs and the associated large cost. While FPGA has the same flexibility as a processor-based system, it is not limited by the number of processing cores. FPGAs are truly parallel in nature. Each processing task is assigned to a different portion of the chip with no interaction to other logic blocks, therefore the processes are not competing for the same resources. This allows the I/O to be controlled at the hardware level which provides faster response times with specialized functionality to meet the application requirements.

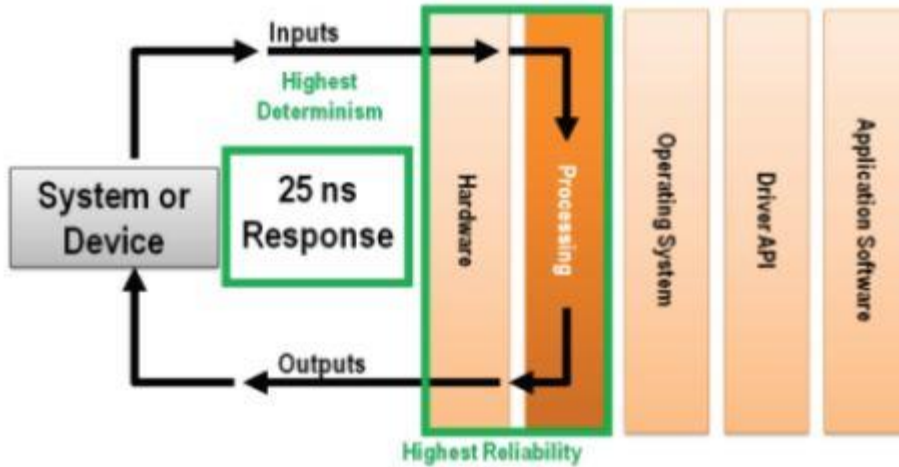


Figure 4-3 Hardware-level processing allows for high amounts of reliability as well as low response times versus trying to carry out the same functionality through an operating system.³ With FPGA there are not the layers of software that the code and data travels through so there is much faster processing. Image taken from National Instruments.

Illustrated in Figure 4-4 below, the main components of the FPGA chip include I/O blocks, configurable logic blocks, and a programmable interconnect. I/O blocks are special blocks on the peripheral for external connections. The configurable logic blocks are used to implement the combinational and sequential logic. The programmable interconnect are wires to connect inputs and outputs to logic blocks.

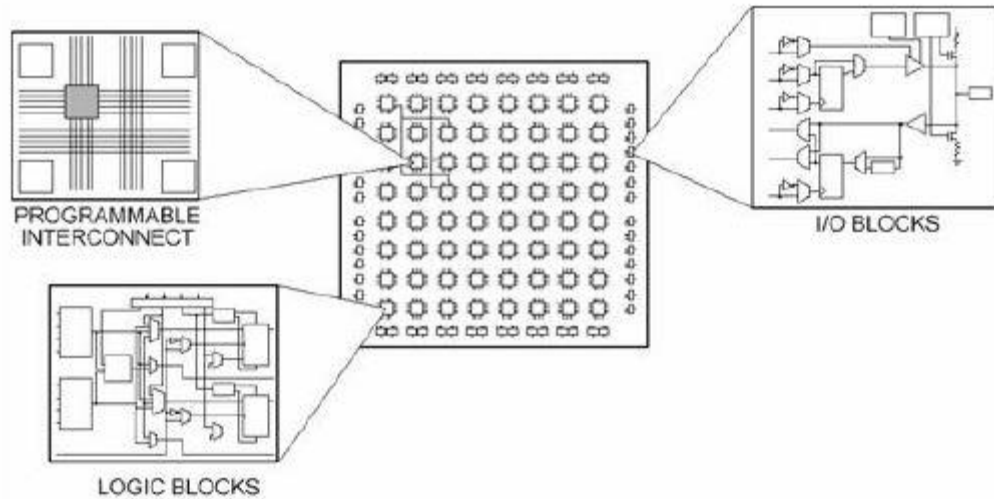


Figure 4-4 The different parts of an FPGA³ with the center of the image being the FPGA chip, the other three main components are illustrated as to their location and interaction with each other. Image taken from National Instruments.

The FPGA module used in the P5 application is the NI 7965R which uses a Virtex-5 SX95T FPGA chip, with 14,720 FPGA slices, 640 FPGA DSP slices, 8,784 kbit of FPGA memory (block RAM), and 512 MB of onboard memory (DRAM).



Figure 4-5 NI PXIe-7965R. Image taken from National Instruments.

4.2.1.3. NI 5761 Digitizer Module

The NI 5761 adapter module connects to the NI 7965R FPGA module. The NI 5761 adapter module that has four analog input channels with 14-bit resolution. The analog bandwidth is 500 MHz and a sampling rate of 250 MS/s. There are also eight digital I/O channels.



Figure 4-6 NI 5761 Adapter Module used in prototype 5. Image taken from National Instruments.

Two of the four analog input channels are used in the P5 instrument. Channel 0 is used to monitor the PMT signal, and channel 1 is used to monitor the laser PD signal. Four of the digital I/O channels are implemented. Two channels are used in the automated alignment procedure and are discussed below. A third channel is used to monitor the HeNe PD signal for calculating the rotational speed. The HeNe signal is also used to monitor the when the exit slit is 180° to the primary beam path. That pulse is used to initiate the laser triggering sequence to make the primary measurement.

The final digital I/O channel is used to send the digital pulse that triggers the firing of the pulsed nitrogen laser. The signal that is output by the digital I/O is a 2.5 V CMOS, however the nitrogen laser requires a 3 V signal to fire. To increase the voltage to an adequate level, a voltage buffer was designed and fabricated, schematically illustrated in Figure 4-7. Channel 0 is

used where the buffer circuitry is laid out with the circuitry diagrammed in Figure 4-7. Note in Figure 4-7, as mentioned above, Channel 1 is used as the input for the rotational speed. There are also colored LEDs in the design to indicate power (red) as well as when the digital signal is sent to the laser (green).

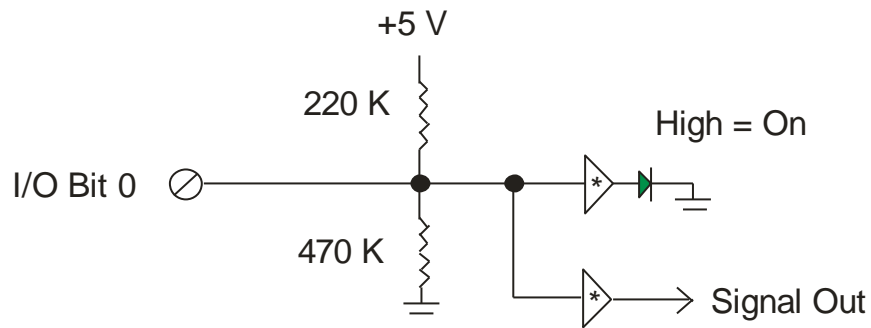
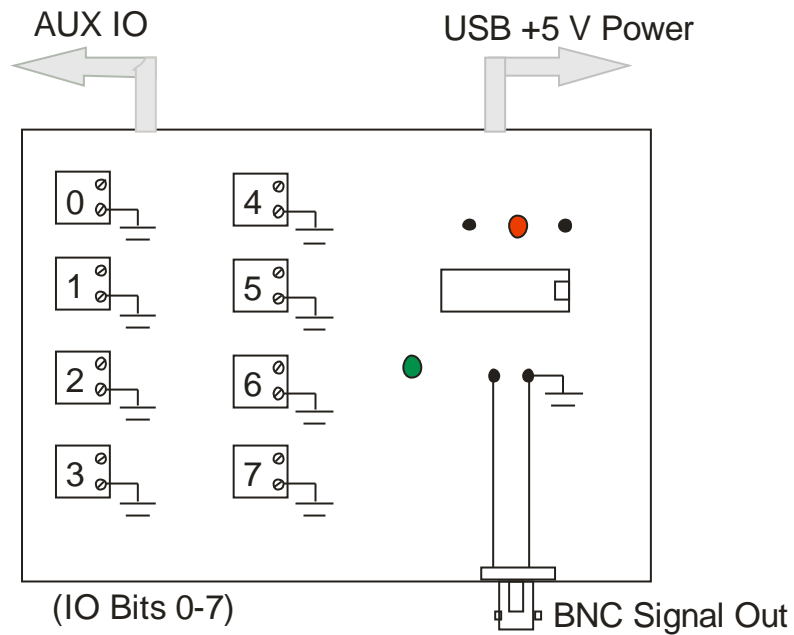


Figure 4-7 Electrical schematic for voltage buffer built to increase the CMOS signal to trigger the Nitrogen laser.

4.2.1.4. Embedded Controller

The embedded controller is the on-board PC for the system that delivers high performance computing in a compact in-chassis embedded computer. The controller that was chosen for this system is the NI PXIe-8108 controller, and is located in slot 1 of the chassis. It has a 2.53 GHz Intel Core 2 Duo T9400 dual-core processor, up to 1 GB/s system bandwidth and 250 MB/s slot bandwidth, and 1 GB (1 x 1 GBDIMM). Windows 7 Professional, LabVIEW® 2012 basics, and LabVIEW Real-Time® are installed on the controller. The drivers for the NI-7965R module and the NI-5761 digitizer are also found on the controller.

4.2.2. Automated Alignment Hardware

The alignment process is similar to that used in the P4 instrument. Because the P5 still uses the CRDS-like source injection method, using the primary laser (pulsed nitrogen laser operating at 488 nm) is not feasible. While the amount of light that enters the cavity through the mirror is sufficient to be measured by the PMT detector, it is not visually detectable and therefore impractical for manual alignment. In the same manner as in the P4 prototype, the P5 design incorporates a 532 nm cw-laser to align the light within the cavity. This wavelength was selected because it is outside the bandwidth of the mirrors (488 nm). To make this alignment source co-linear to the primary source, a diffraction grating was used in manner that is reverse of the way that it is normally used. That is, the beams adjusted to be made co-linear within the cavity as revealed by their merger at the grating. Once the alignment was completed, the alignment source was turned off and measurements were made with the primary source.

4.2.2.1. P5 Automated Alignment Process

The camera was initially placed behind the first folding mirror, concave mirror 1 (CM 1) (Figure 4-8). An object was placed near the surface of the mirror and the camera was then aligned and focused on that object through the mirror. The goal was to view the incident and the reflected light that was striking the surface of CM 1. After extensive testing, it was found that the camera had difficulty detecting the laser beam spot unless it was viewed directly facing the direction of beam's origin. While the camera could easily focus on the spot from the incident beam, light returning from the rotating mirror was difficult for the camera to focus upon. Therefore the instrument layout was re-designed such that the camera is positioned to focus and CM 1 to monitor the light after striking the rotating mirror and en route to the entrance mirror.

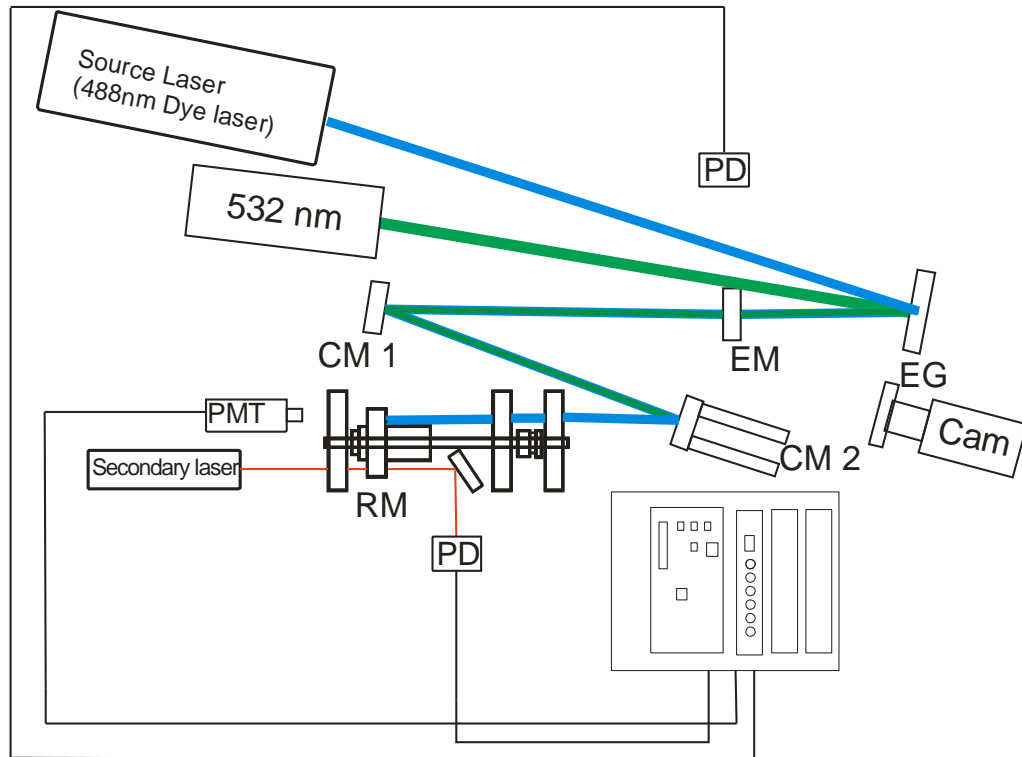


Figure 4-8 Diagram of P5 instrument. (EG, Grating; EM, Entrance Mirror; CM 1, Concave Mirror 1; CM 2, Concave Mirror 2; RM, Rotating Mirror; PMT, Photomultiplier Tube Detector; PD, Photodiode Detector; Cam, Allied Technologies Camera; 532 nm, CW Alignment Laser; Secondary Laser, 633 HeNe) Initially the camera was placed behind CM-1, however inadequate images were obtained so the current design was implemented with the camera locate behind CM 2 to image CM 1. CM 2 has the piezoelectric motors attached to the mount.

The automated alignment process is as follows: the LEDs are found at the front of CM 1 as shown in Figure 4-9. Figure 4-10 is an example of an image captured by the camera. The image is then processed in LabVIEW Vision® software on the NI PXIe-8108 Controller. Because these LEDs are affixed to the front of the mirror mount, their location is precisely known. That information is utilized by the LabVIEW® algorithm to triangulate the center of the mirror based on the image of the illuminated LEDs.

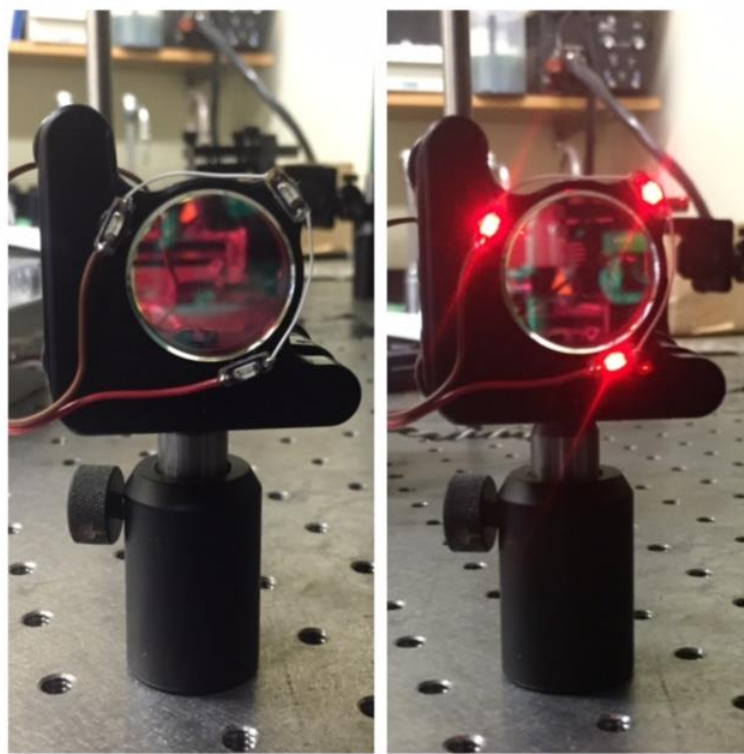


Figure 4-9 Image of CM-1 face with the LED's off (left) as they would be during a measurement, and on (right) as they would be during the automated alignment process.



Figure 4-10 Example of an image taken by the Allied Technologies camera; this image is processed through an algorithm to triangulate the center of the mirror.

Once the LED coordinates are determined, they are saved for reference and subsequent iterations. The LEDs are then turned off, and the shutter is opened to allow the cw laser light (532 nm) to enter the cavity. The camera then captures the location of the beam as the source light is returning from the rotating mirror to the entrance mirror; an example of the image from the camera is shown in Figure 4-11. LabVIEW® then iteratively processes the image so that the source beam strikes the center of the mirror, i.e., based upon the coordinates calculated from the triangular LEDs. The positioning is adjusted at concave mirror 2 (CM 2) to using electric motors controlled by “T cubes”. The “T cubes” are single channel DC servo control motors. They are connected to the PXIe controller by USB cable. The alignment is based on the

assumption that the cw laser is co-linear to the dye laser and that those beams are entering the cavity and striking the center of CM 1.

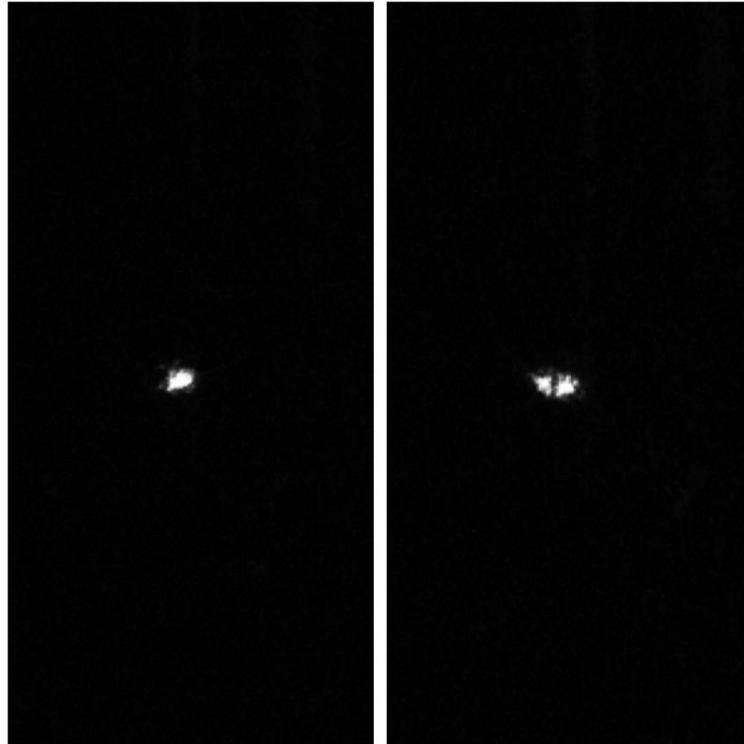


Figure 4-11 The images were captured by Allied Technologies camera. This is a comparison of the aligned (left image) vs. misaligned (right). Two spots are observed as one is the incident light and the second spot is the light returning to the entrance Mirror

The alignment is done in five steps: locating the center of the mirror, locating the incident beam, locating the reflected beam, adjusting the vertical position, and adjusting the horizontal position. To align the cavity, the entrance mirror must first be moved out of the beam path. Ideally the alignment process would not have the entrance mirror moved, however the amount of light from the secondary laser that passes through the entrance mirror was insufficient to be detected by the camera. The current position of the camera (labeled “CAM”

in Figure 4-8) provided the best images of both the incident light as well as the light reflected back to CM 1 from the rotating mirror.

The first step in the program is to locate the center of the mirror. This is done by locating the three LED's placed on the surface of the mirror mount. Once the software locates those points, the central coordinates are then used to overlay the green lines as seen in Figure 4-12. The midpoint of each of the three lines is calculated and the red lines are overlaid by connecting the midpoint and the opposite point in the triangle.

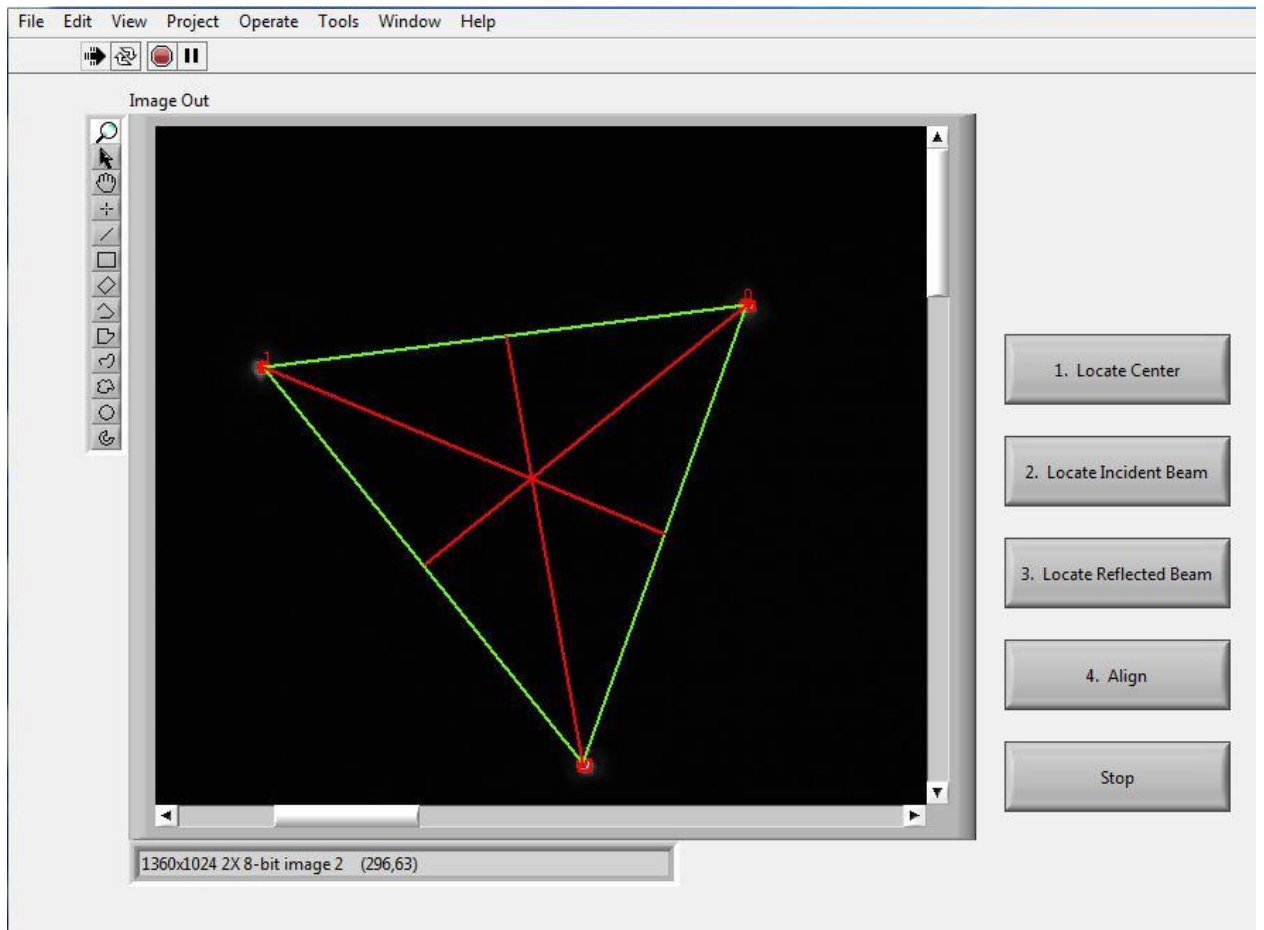


Figure 4-12 Step 1 of the alignment process involves locating the LED's and overlaying the crosshairs based on the midpoints between the points.

The next step is to turn off the LED's and turn on the secondary laser. The coordinates of the LED's are used to overlay the lines for the triangle as well as the crosshairs. The exposure time of the camera is also increased to locate the incident beam, which is the light that is coming from the secondary laser, which is reflected off the diffraction grating and striking CM 1, as seen in Figure 4-13. This allows the operator to confirm that the incident light is striking the center of the concave mirror. If the light is not, the operator can adjust the position of the diffraction grating to aim the beam to at the center of the mirror.

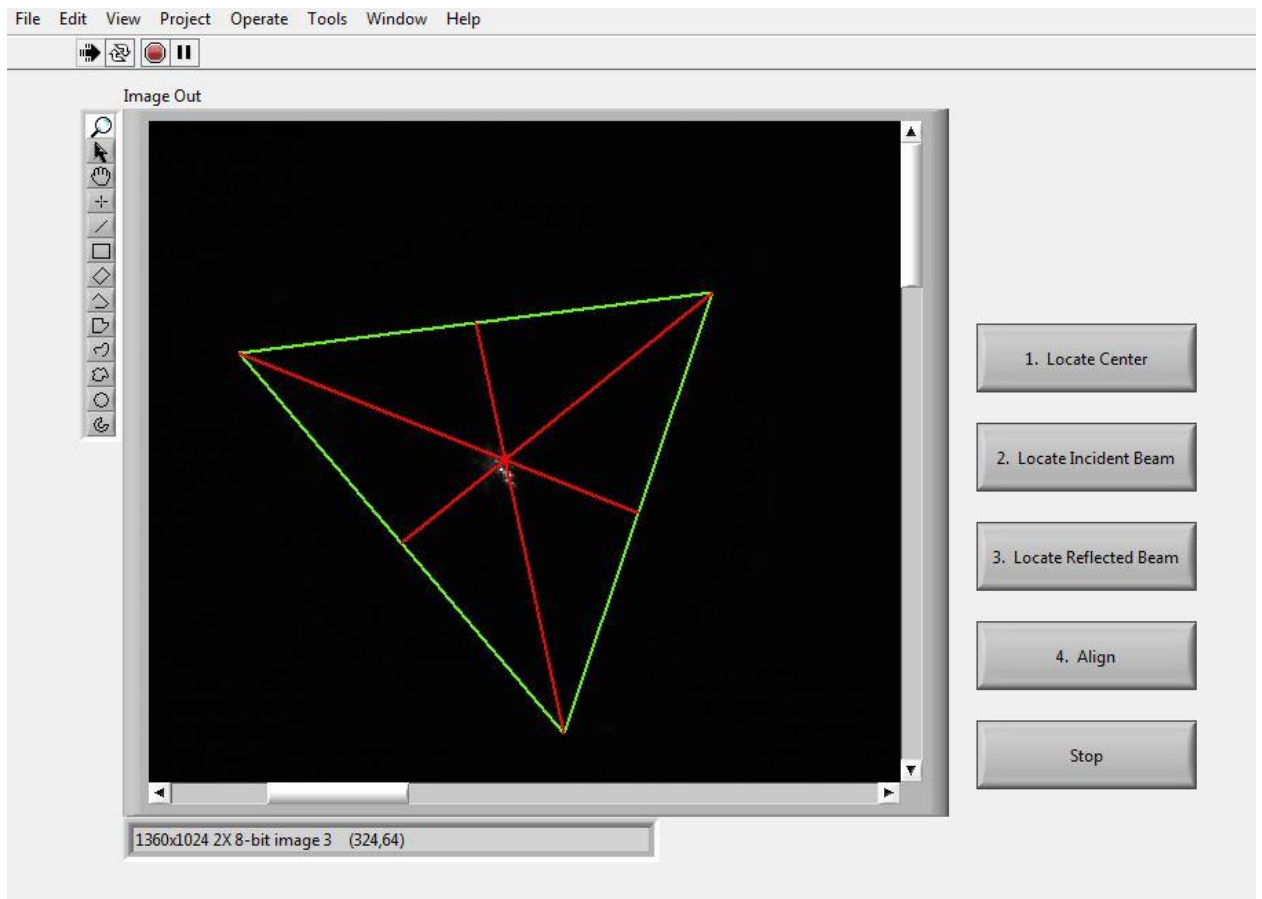


Figure 4-13 Step 2 of the alignment process is to locate the incident beam and confirm that it is striking the center of the mirror.

The next step is to locate the beam spot that has made a pass through the cavity and is returning to the entrance mirror. This spot can be seen as the off-center spot in Figure 4-14 below. Since the intensity of the reflected beam is lower than the incident beam, the exposure time on the camera needed to be increased again.

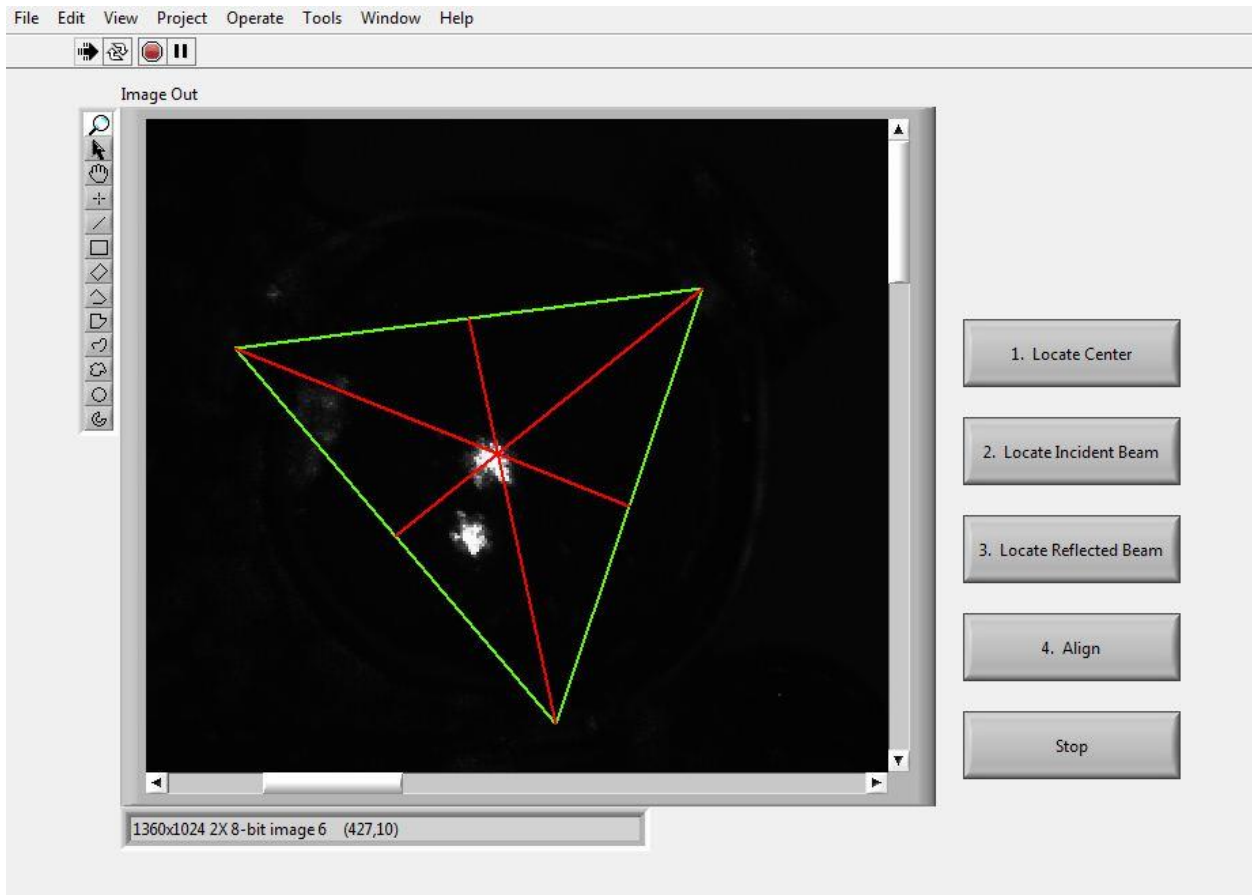


Figure 4-14 Step 3 of the alignment process is locating the position of the reflected beam after making a pass through the cavity, striking the rotating mirror, and returning to the entrance mirror.

Steps four and five involve the adjustment of CM 2 with the piezo-electric actuators. The operator can either press the “Jog” arrows seen in Figure 4-15 or input a numerical value by double-clicking the position coordinate box to input a smaller increment for the mount to

move. First the position for the vertical alignment is adjusted, followed by adjustment of the lateral position.

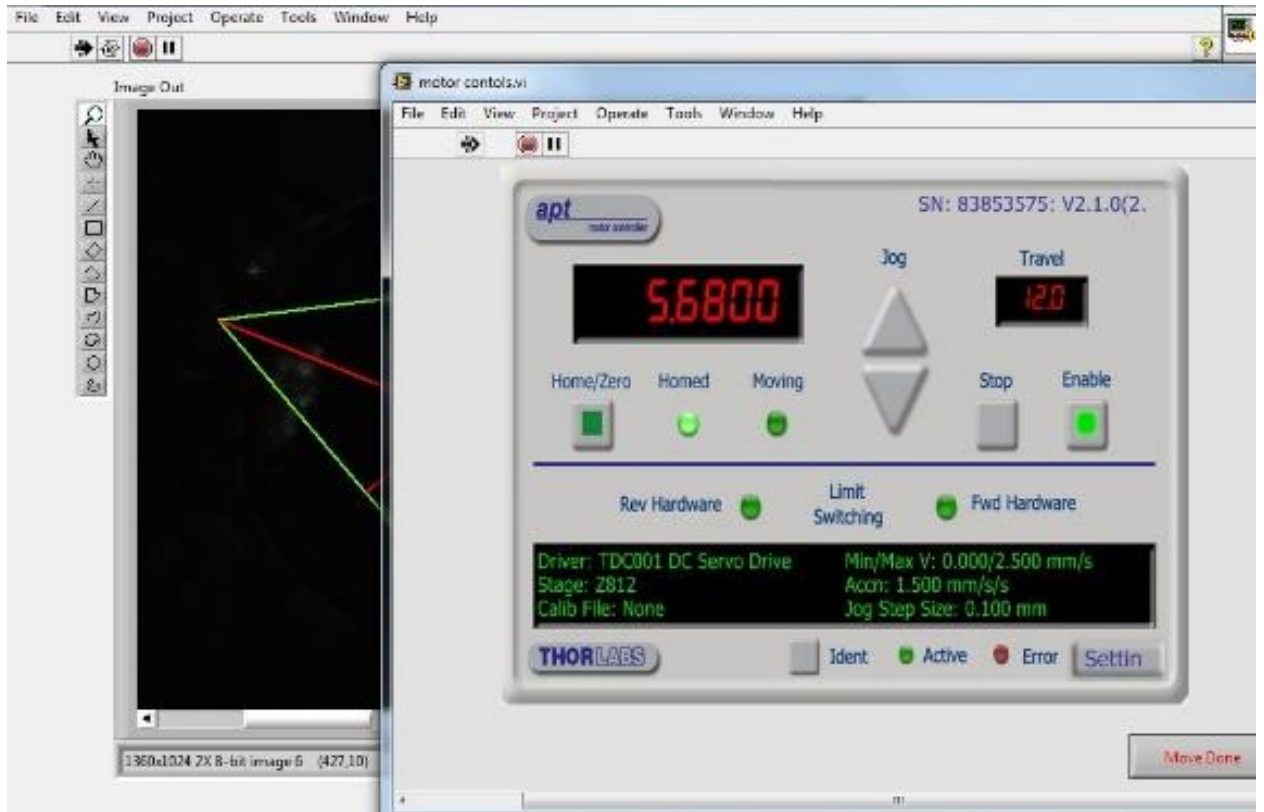


Figure 4-15 The operator can adjust the position of CM 2 by pressing the "Jog" arrow or by double-clicking the position and inputting a value for a smaller adjustment.

After adjusting the position of the mount, the operator can click the "Move Done" button on the pop up window and a new image of the beam positions will be acquired and displayed. The operator is then prompted to choose if the beam is aligned (Figure 4-16). The crosshairs are still displayed to confirm the position of the beams relative to the center of the mirror. Figure 4-16 illustrates the final alignment position with the reflected beam aligned and both beams at the center of the mirror. Since the two beams are now located in the horizontal

plane of the mirror the operator clicks "Yes", and the VI will proceed to repeat the procedure for the horizontal positioning.

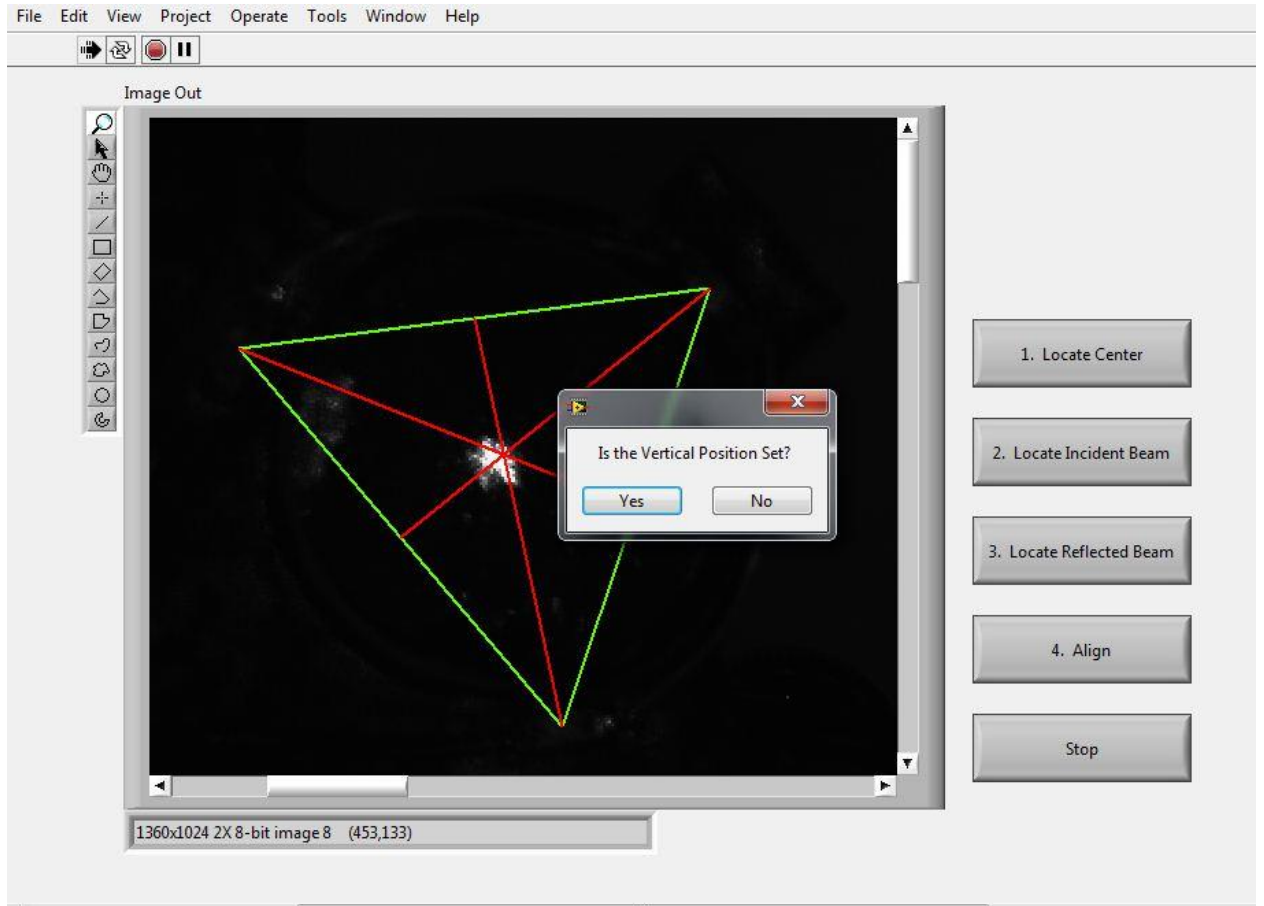


Figure 4-16 Updated image of the new position of the beam based on the adjustments made to the vertical position change. If the operator selects "Yes", the VI proceeds to aligning the horizontal position; if "No" is selected the control menu is displayed to continue adjusting the vertical position.

Once the alignment is complete, the operator then moves the entrance mirror back into alignment by having the back-reflected light from the entrance mirror pass through the iris that is between the entrance mirror and the diffraction grating.

4.3.P5 Software

The combination of National Instruments hardware and the LabVIEW® platform were selected for the P5 version of the VPCS for several reasons. LabVIEW® is optimized for engineers and scientists. It offers graphical programming to allow users to create applications to test, control, and make measurements. While the LabVIEW® programming environment allows for flexibility to program many different applications, it also comes with a tool box containing thousands of built-in functions. The modularity and reconfigurability of the National Instruments hardware combined with the LabVIEW® programming language made for ideal instrument prototyping.

4.3.1. LabVIEW® Programming Language

Applications created in LabVIEW® are called “virtual instruments” (VIs) because the appearance and function of these programs resembles that of physical instruments such as oscilloscopes or multimeters. There are two parts of a VI: the front panel and the block diagram. The front panel is the user interface of the VI where the user can control the VI by inputting values or pressing buttons to display data. The block diagram is the portion of the VI

where the code is placed to process the input data from the user, perform the programmed algorithm, and then display the output data. An example of a simple VI is illustrated in Figure 4.17. The functionality of this VI is to simultaneously add and subtract two values. The user inputs two numbers in the two boxes on the left of the front panel (right), presses the run arrow on the top bar, and then the VI executes the algorithm and displays the results. The block diagram (left) is the programmed algorithm. The data flow follows the lines from each of the inputs of X and Y. The “wire” from each of the inputs is split and the value is sent to both the addition and subtraction functions. The arithmetic is carried out and the data then passes along the wire to the indicators on the right of the block diagram.

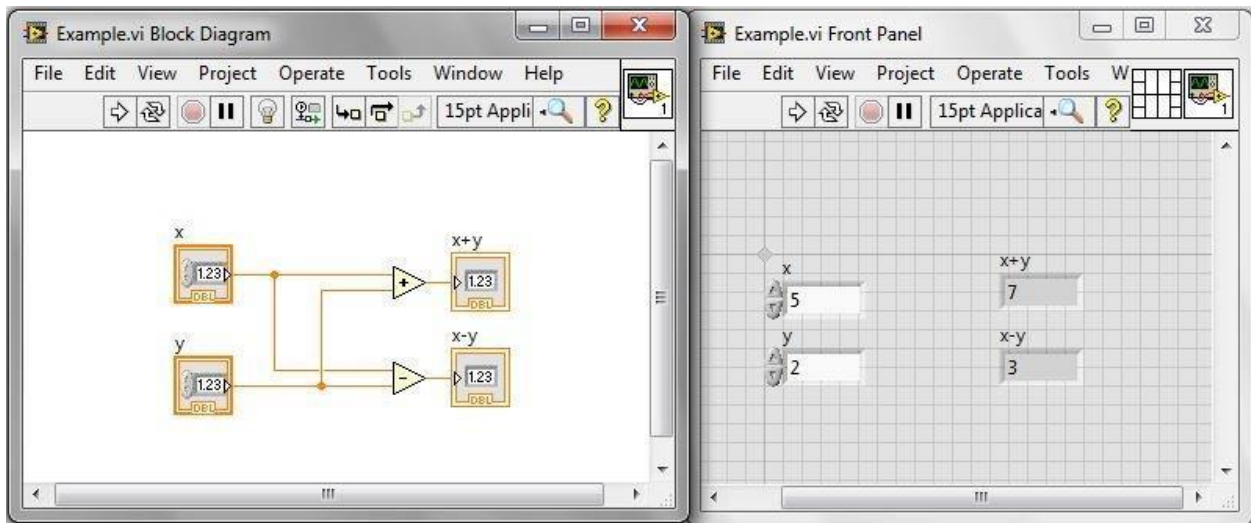


Figure 4-17 An example VI showing the block diagram (left) and front panel (right) for the addition and subtraction of X and Y.

4.3.1.1. Programming Structures in LabVIEW®

The VI in Figure 4.17 will only go through one iteration. There are several different structures that are used to programmatically control the flow and the execution of a subdiagram. These are implemented depending on the desired functionality of the VI being created.

4.3.1.1.1. While Loop

A While Loop, shown in Figure 4.18, is a structure that repeats the subdiagram inside the loop until the conditional terminal (input terminal) receives a particular Boolean value. In the loop, the conditional terminal is located in the lower right corner and can be programmed to “stop if true” or “continue if true”. In Figure 4.18 the current representation is “stop if true”. This condition can be met if there is a Boolean button on the front panel or it can be programmed to terminate the loop if a programmed Boolean logic operator is met. The box in the lower left corner of the loop structure is the iteration count, ranging from 0 to $n-1$.

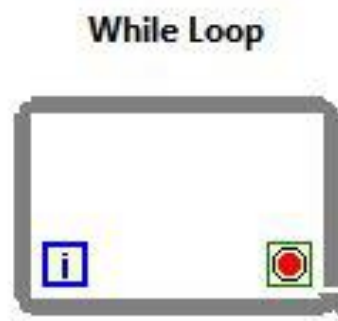


Figure 4-18 While Loop structure. The loop will continuously run until the Boolean value (right, "stop if true" icon) is met. The box (left) with the "i" is number of iterations.

In Figure 4-19, a While Loop has been added to the VI shown in Figure 4-17. Here the run arrow of the VI is clicked (below the “Edit” pull-down menu) and the subdiagram will continuously function and the output of “x+y” and “x-y” will be updated if the user changes either of the inputs. When the user clicks the stop button (below data outputs), a Boolean value of “true” is sent to the conditional terminal to stop the While Loop from executing.

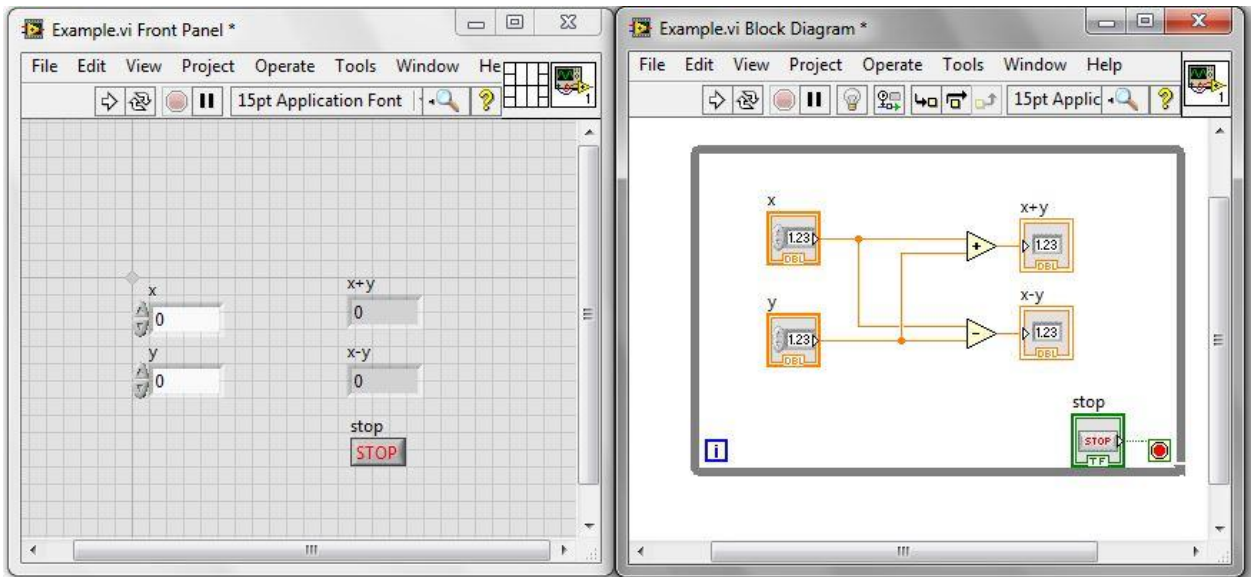


Figure 4-19 The While Loop will run continuously perform the data reduction until the stop button is clicked on the front panel.

4.3.1.1.2. For Loop

The For Loop is a structure that will execute a subdiagram for n iterations. The lower left corner in Figure 4-20 displays the same iteration count as in the While Loop. This structure now has an input on the upper left corner, “ N ”, that is the determination of how many iterations the loop will execute. This value is wired to the count terminal. This can be programmed by wiring a constant value on the block diagram, a user input value through a control on the front panel, or through any numeric value that is derived from the data (i.e., a For Loop can be programmed to execute based on the number of data points in an array that is being reduced in the subdiagram). As with the While Loop, the iteration count ranges from 0 to $n-1$.

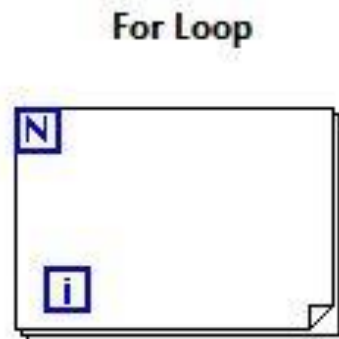


Figure 4-20 For Loop executes n iterations, where n is wired to the input on the upper left hand corner.

In Figure 4-21 a For Loop has been applied to an iterative addition VI. A shift register has been added to the loop, which is the downward-facing triangle of the left of the structure and paired to the upward-facing triangle of the right of the structure. Shift registers store data from the previous iteration so that it can be used in the second iteration and can be

applied to For Loops or While Loops. For example, for the VI shown in Figure 4-21, each iteration is going to add the “y” value to the number for each iteration (in this example, the increment is 1). The count terminal has the *N* input terminal wired with a constant value of 10; therefore, this subdiagram will undergo 10 iterations and then stop. The “x” value is outside the loop and writing a value of zero for the first iteration of the loop. After the first iteration of the loop, the reduction that occurs is “0+1”, and the result of that operation is then stored on the shift register to be used for the next iteration. The second iteration will take the value off the shift register (i.e., 1) and carry out the operation of the addition of “y”, resulting in a value of 2. The value of two will be stored on the shift register for the subsequent iteration. This will continue until the iteration count of the loop equals that of the count terminal. LabVIEW® counts the first iteration as “0”, therefore at the end of the 10 iterations of the loop the iteration count is displayed as nine (9).

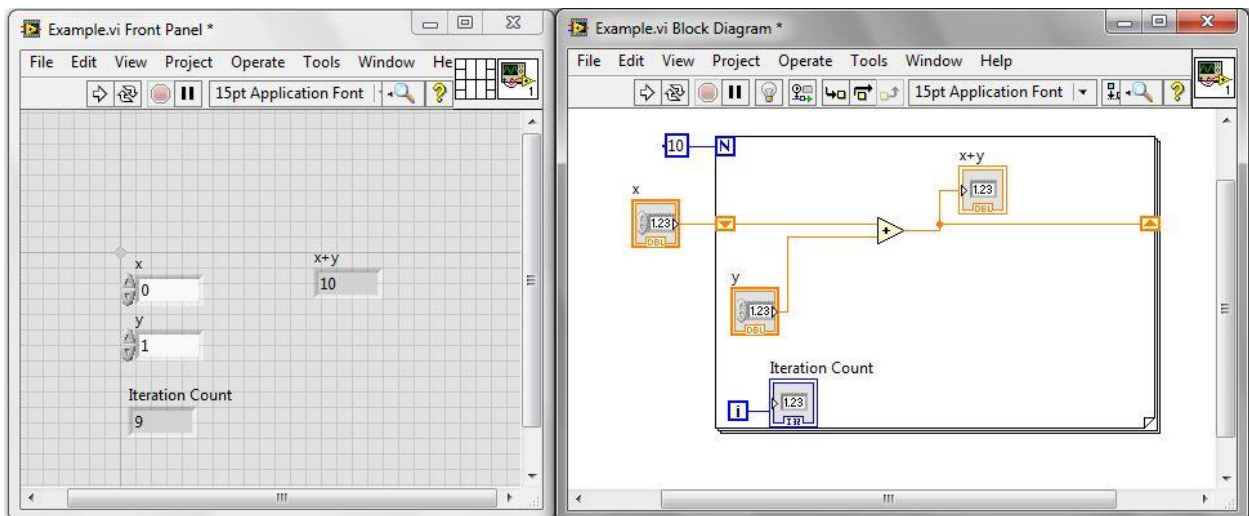


Figure 4-21 A for loop used to increment an input value "x" by "y", for 10 iterations. The result of the loop is stored on the shift register to be used for the mathematical operation in the subsequent iteration.

4.3.1.1.3. Sequence Structure

Sequence structures are used when the execution of a subdiagram needs to happen in a precise order. A sequence structure, shown in Figure 4-22, consists of one or more subdiagrams, or frames, that undergo one iteration unless paired with a While Loop or For Loop. Data flows from left to right in a sequence structure, and the next sequence cannot execute until the previous sequence finishes.

**Flat Sequence Structure
[Flat Sequence]**

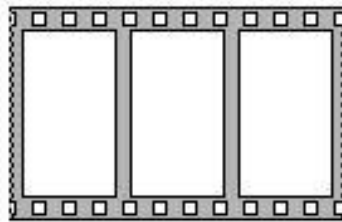


Figure 4-22 Sequence structure controls the order in which subdiagrams occur, starting on the left and working toward the right.

There may be portions of the subdiagram that take longer to execute than others. In Figure 4.18, the “y” value is passing to the second frame of the sequence structure. Since there is processing that is being done, that value will sit at the terminal between frame one and two. In order for the second frame to execute the value of “y” and “x+y” must both be at the terminal; it is only when all the operations are completed in the first frame that the data can pass through the terminal to be carried out in the second frame.

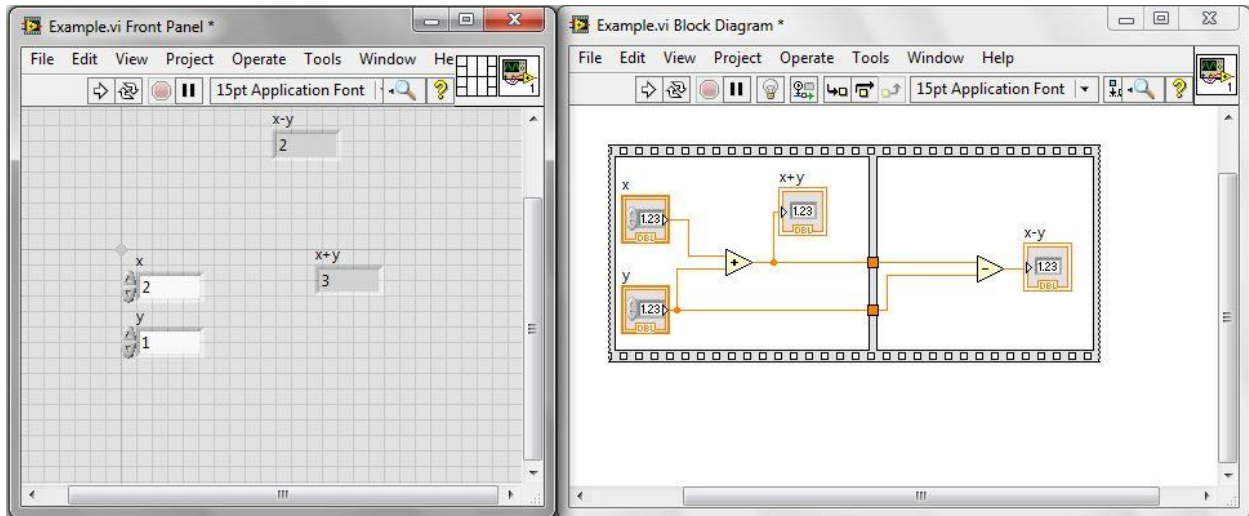


Figure 4-23 Example of the use of a sequence structure. This controls the order in which the subdiagrams will execute. Once all data is at the terminals then the second frame can execute.

4.3.1.1.4. Case Structure

Case structures have one or more subdiagrams or cases, however only one of these subdiagrams executes. There is a value wired to the selector terminal (the question mark on the left side of the structure in Figure 4-18) that determines the subdiagram that executes. Different cases can be set up for an input from Boolean, string, numeric, enumerated type, or error clusters.

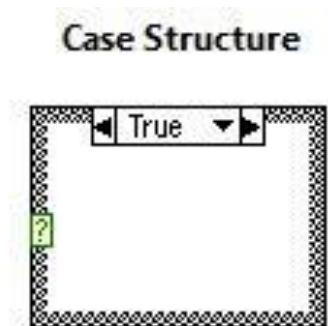


Figure 4-24 Case structure, with the true case showing. The selector terminal is the question mark (?) on the left side of the structure and is used to select the case that will be executed.

Figures 4-24 and 4-25 are examples where a Boolean is used to select the case. In both examples the mathematical function of “x+y” are carried out. The output of the function is sent to a “greater than 0?” function. If the output is greater than zero, a Boolean value of true is output, if less than zero a false value is output. That Boolean is wired to the selector terminal which then executes the appropriate case, which in this example is trigger a Boolean indicator on the front panel.

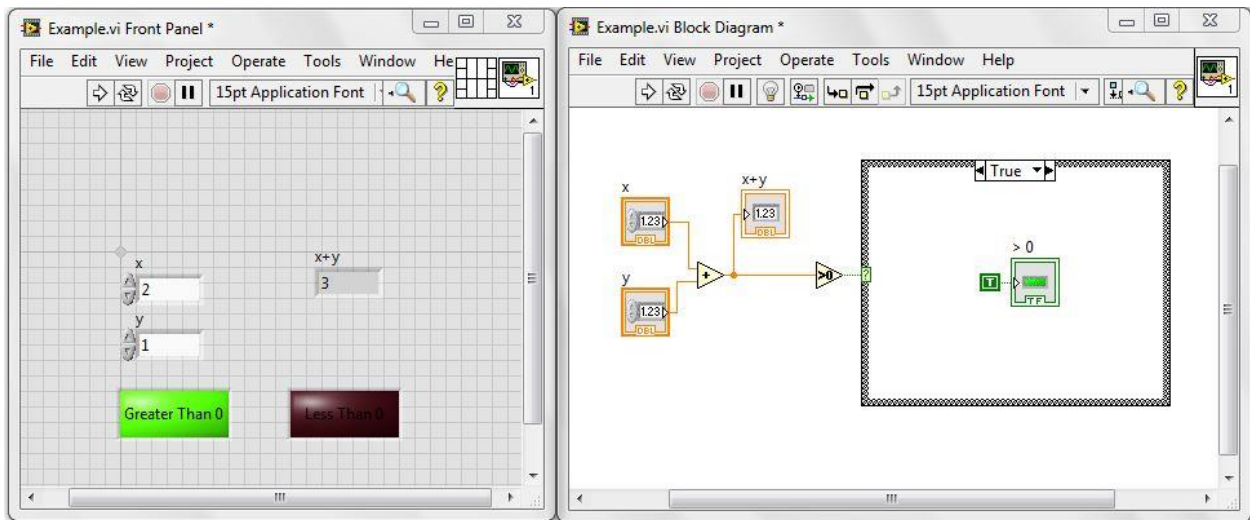


Figure 4-25 Case structure where the input to the selector terminal is true, causing the true case to be executed and lighting up the "Greater Than 0" Boolean on the front panel.

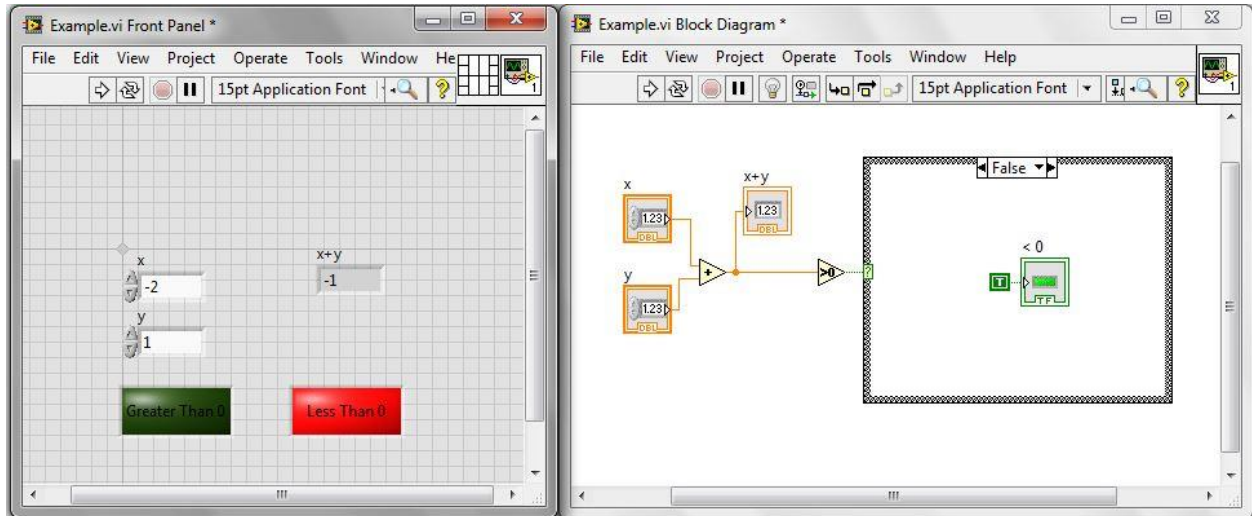


Figure 4-26 Case structure where the input to the selector terminal is false, causing the false case to be executed and lighting up the "Less Than 0" Boolean on the front panel.

4.3.1.2. Program Architecture for LabVIEW® and LabVIEW Real-Time®

As the desired functionality of VI's increases there are several common architectures that are used to maximize the data collection and reduction. LabVIEW® programming through Windows does not allow for true parallel processing. These different architectures are applied to a VI, increasing modularity which prevents data loss, creates better trouble shooting and error handling, and allows for ease in the addition of new functionality.

4.3.1.2.1. Producer-Consumer Architecture

A way to account for the serial execution of processes in a VI is through the use of the Producer-Consumer architecture. When a VI is running the processes are operating in a serial

and will be running at different rates. This architecture is used when the desired functionality of a VI is data collection and reduction. The data is collected and stored in a queue to be processed in the order in was collected. As shown in Figure 4-27, the simplest form of this architecture is two loops. As the name implies there is one loop that is producing data and the second loop is consuming or reducing that data being produced.

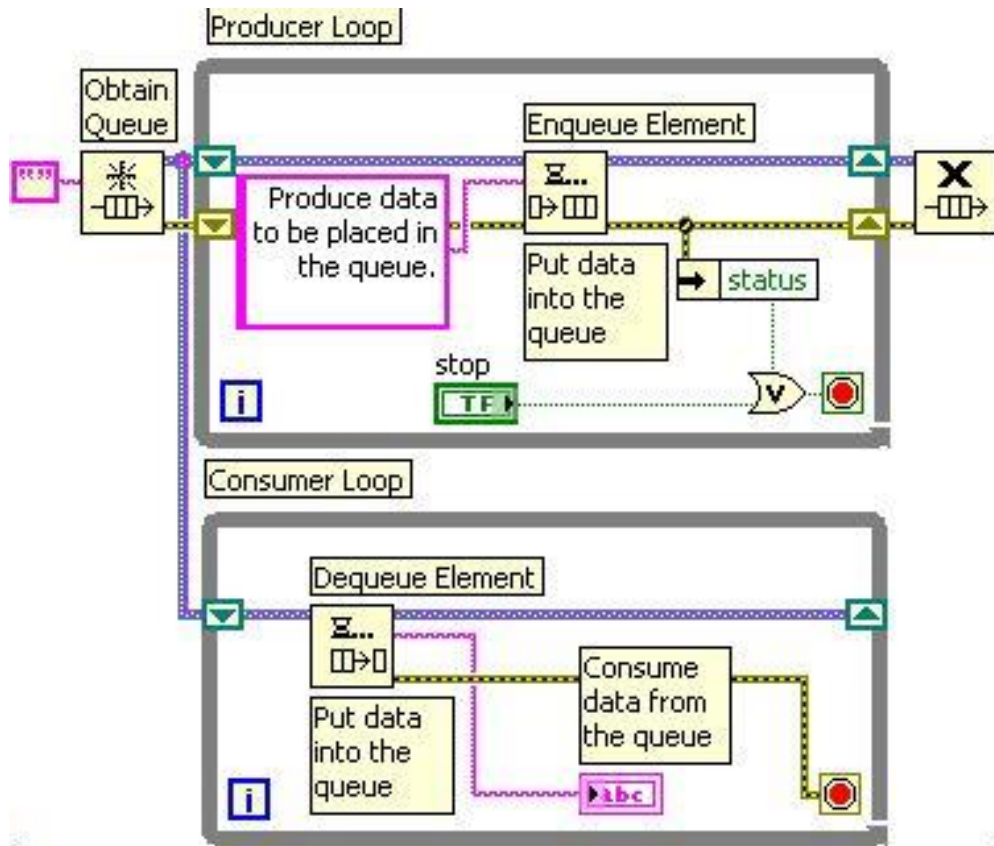


Figure 4-27 Structure of a Producer-Consumer architecture. The upper loop is producing the data and saving it to a queue, while the consumer loop reads the data from the queue and performs the data reduction.

In implementing a Producer-Consumer architecture the initial step is to create a queue or a FIFO (First In First Out). This is where data is produced in the first loop is stored until it is

reduced in the second loop. As data is generated in the producer loop it is then stored in the queue until called upon in the consumer loop.

4.3.1.2.2. State Machine

One of the fundamental architectures in LabVIEW® is a state machine. This method is used to implement complex decision-making algorithms that are represented by flow charts or state diagrams, and typically applied to situations with a user interface. State machines are used when distinct states, or separate blocks of code, exist and there is a specific action needed to be carried out by each state. These are done by implementing case structures as discussed earlier, however instead of using true/false for the cases, any number of case can be added to the structure to tailor to the VI functionality.

The first step in a state machine is an “initialization” step, followed by a “default” state. Once the VI is initiated the “default” state is the resting state for the VI. The data flow from states are controlled either by data inputs or user inputs. An example of a flow chart that could be a common state machine VI is illustrated in Figure 4-28.

The VI is created to control the temperature of a device, i.e. a computer. Upon starting the VI an initialization step is undergone. This prepares the VI to carry out its functionality. This can include opening communication channels with hardware, set temperature threshold for when the fan turns on, maximum temperature to force emergency shutdown, etc. For this example the “default” state would be the “Monitor Temperature” state. In this state it would be checking the thermocouple at a set interval (written into the code), and the temperature

data would determine the state that the VI would go to. If the temperature is below the set threshold, the fan would not turn on and it would sit in the “monitor temperature” state. As the device is warming up, and the temperature reaches the threshold value a Boolean value triggers the changing of the state machine to the “Fan Control” state. In this state the fan would then be turned on to help regulate the temperature. If the temperature reading in the “Monitor Temperature” state reaches the maximum temperature value, it would go into the “Emergency Shutdown” state. Here, the shutdown procedure to help protect any hardware for suffering from damage due to over-heating.

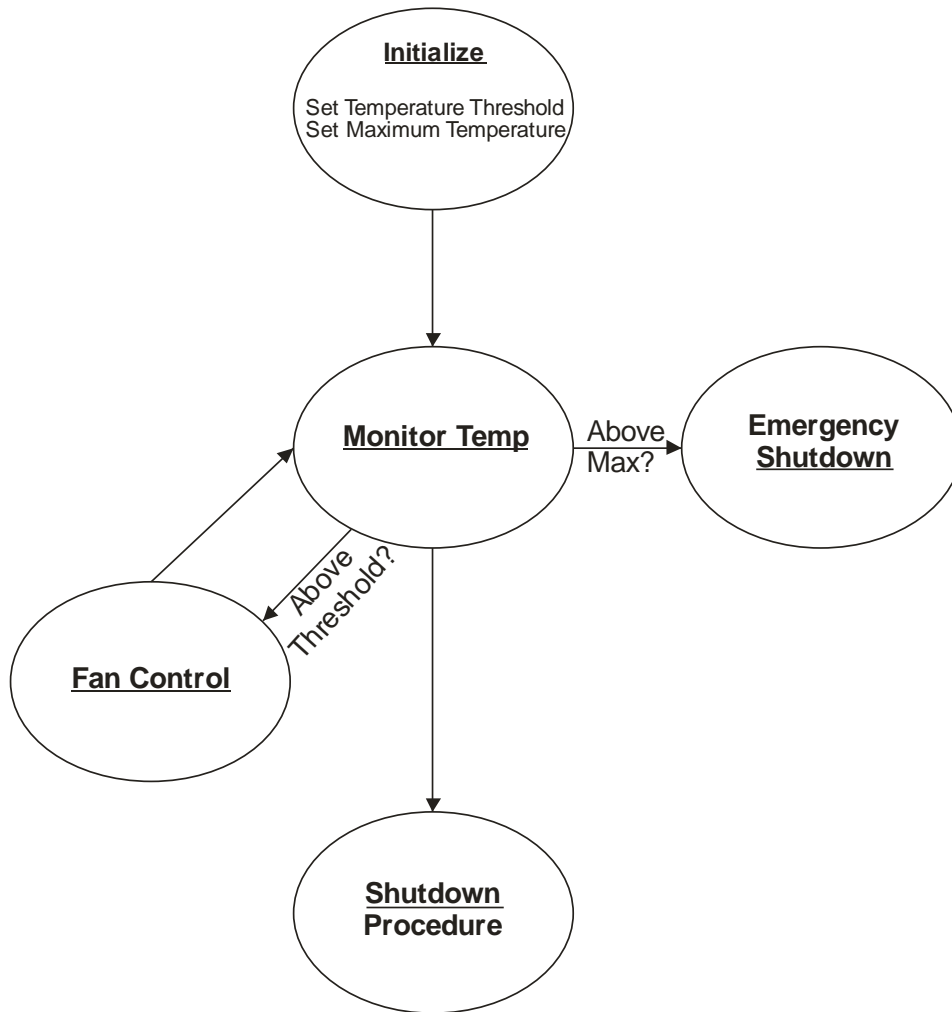


Figure 4-28 Flow chart for a simple state machine. Flow chart describing temperature monitoring. The VI is initialized, with setting the threshold and maximum temperature values.

The way this is executed in LabVIEW® is by placing a case structure inside a While Loop, as shown in Figure 4-29. Since this is something that is typically run for extended periods of time, the While Loop is used to repeat the current state in the case structure until the state changes.

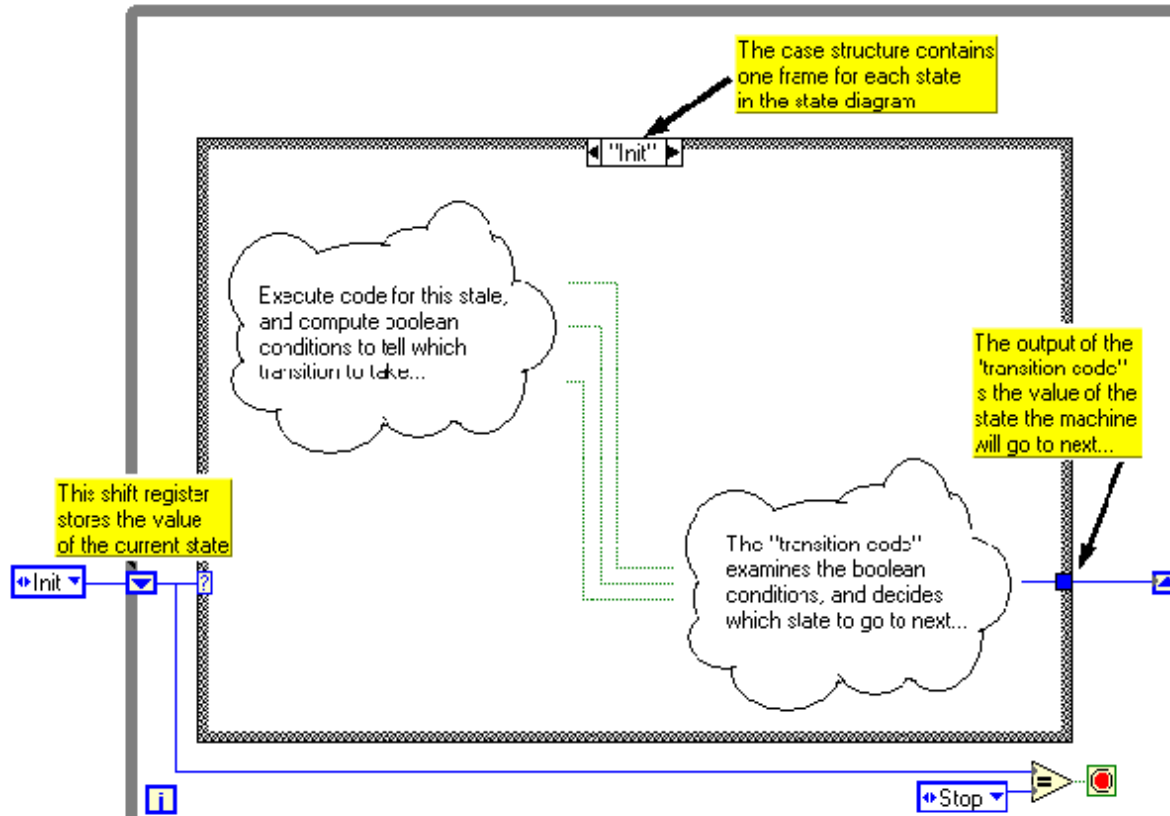


Figure 4-29 Example of how a state machine looks programmatically. It is a case structure that is in a while loop. Shift registers are used on the while loop to carry over the data to set the state of the case structure. Figure taken from National Instruments.

4.3.1.2.3. Real-Time® Architecture

When working with FPGA there is a protocol for transferring data to and from the FPGA module. To maximize the functionality of the FPGA the best programming practice is to have the essential code on the FPGA. To do this the Real-Time® software is used to communicate

between the user interface and the FPGA. Figure 4-30 shows the architectural layout for linking the user interface to the FPGA VI.

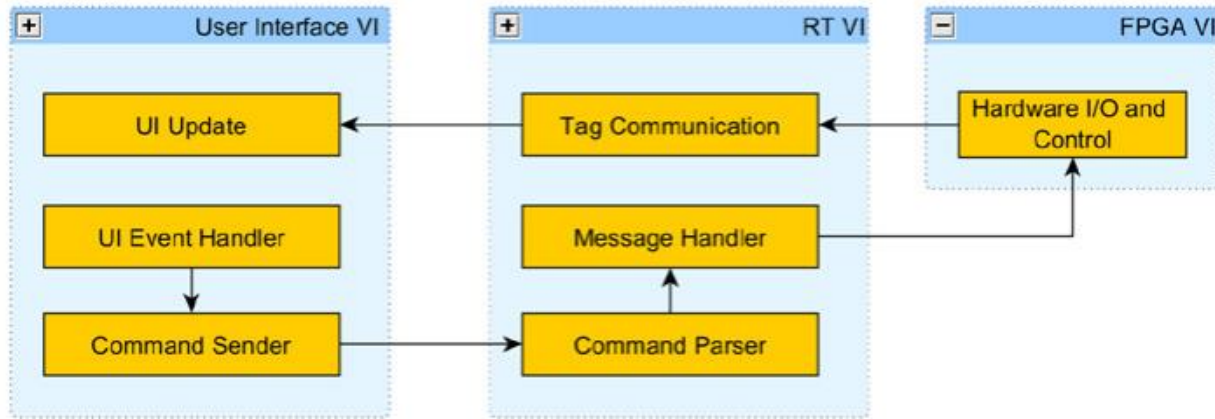


Figure 4-30 Common software architecture for control and monitoring applications. There is the User Interface, the Real-Time® VI or Host VI, and the FPGA VI or Target.

There are three types of data transfer (data transfer is represented by black arrows in Figure 4-30) that are used in Real Time architecture depending on the desired functionality. Message/Command transfer is used for low-latency data transfer, i.e., user inputting a value or pressing a button on the user interface. Current Value or Tag signal is data that is used for low-latency as well. These are commonly bound to Input/output (I/O) channels in a high-channel-count system and used to transfer a current data value, i.e., a set point for a control system or current temperature. The final type of data transfer is Stream. Streaming is used when high throughput of data is required and latency is not a concern. This is accomplished by using multiple layers of buffers. At the FPGA level the buffer is smaller and transfer data to the Real Time interface in smaller groups where there is a larger buffer to store more data. The Real Time VI has larger buffer capability and is able to transfer larger groups of data.

4.3.2. P5 Software Testing

The main focus of this work has been to develop the automated working prototype of the VPLS. The coding architectures previously described were implemented on a larger scale to create a VI with the desired functionality of the instrument.

4.3.2.1. VPLS LabVIEW® Architecture

The design of the program for the P5 instrument follows the State Machine architecture, due to the flow of automating the instrument from initialization, triggering, collecting data, etc. This program is running in the Windows-based environment of LabVIEW®, with functions that call to access the FPGA through Real-Time® communications and previously discussed. The flow diagram of the State Machine is illustrated in Figure 4-31.

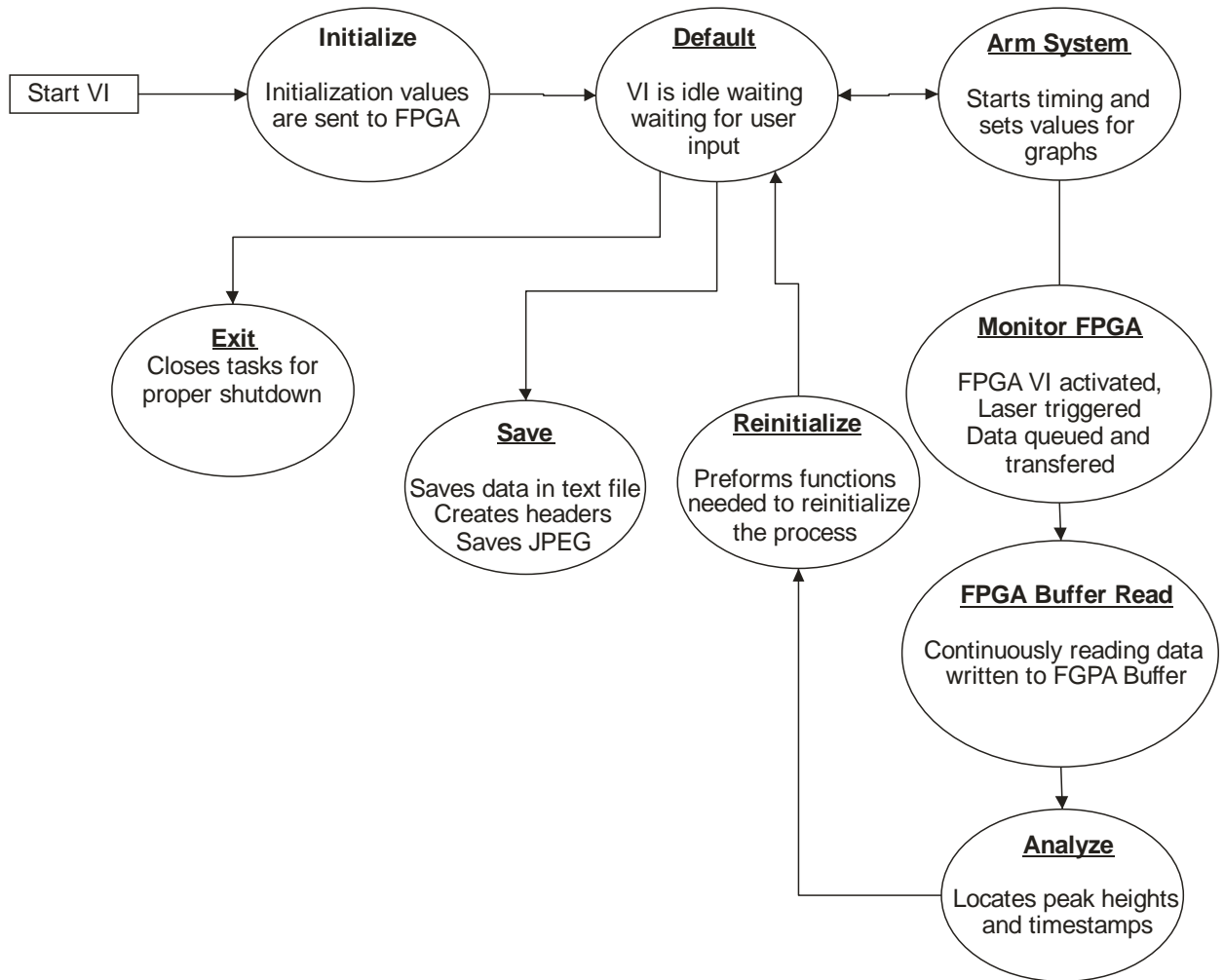


Figure 4-31 Flow diagram of VPLS State Machine

Once the VI is started, the VI opens the calling VI's that are in the program as well as opening the communication to the FPGA target. Once the initialization is complete the VI waits in the default state, where the user has control over inputs for the instrument. The inputs include control over the programmed delay, number of data points to collect, as well as different controls for troubleshooting. The key troubleshooting controls allow the user to simulate a constant rotational speed and manually trigger the laser. Once the desired delay is

input, that is sent to the FPGA in the “Arm VI” state. Once these values are input the VI then sits in the default state until the user clicks the “Arm System” button. Once clicked the VI then goes through the data collection loop. The programmed delay counter is initiated once the threshold is reached on the HeNe digital input. The HeNe PD is used to monitor the rotational speed of the mirror as well as act as the trigger to start the programmed delay. Looking at the face of the rotating mirror, the PMT is located behind the mirror at the three o’clock position and the HeNe is located at the nine o’clock position.

The programmed delay is determined by using the rotational speed and calculating the time required for the mirror to rotate 180 degrees. A user input delay of “0” would theoretically then be a single pass measurement. The adjustment for collecting the full curve is done by adjusting this delay to trigger the laser before or after 180 degrees. For example at 83.3 Hz (5000 RPM), it will take 6,000 μ sec to complete one-half of a rotation. If the user leave the default value of zero programmed for the time adjustment, the laser will trigger and that will correspond to a single pass measurement. For trapping to occur the laser needs to be triggered before the slit rotates into the primary laser beam path. This is done by inputting a negative value which is then subtracted from the time required to make one-half of a rotation. For example, inputting a value of -250 adjusts the delay time to 5750 μ sec in this example.

Once the adjustment has been input to the VI and the “run” button has been pressed, the VI takes the rotational speed from the previous rotation and calculates the time for one-half of a rotation. The adjusted value is then subtracted and the resulting time is the input to the sequence structure that delays the firing of the primary laser.

Once the “Arm System” button is pressed, the data from the analog inputs monitoring the dye laser PD and the PMT monitoring starts. These values are stored locally on the FPGA in buffers and on the Host or PC VI, the data is then pulled to the Host or PC VI to ensure data does not overflow the FPGA buffer. Once the data collection is complete, the Host VI then uses a peak finding VI to locate the peaks for the PMT and dye laser PD signal, and their corresponding timestamps.

The data is graphically displayed on the user interface as well as the peak information. The operator can then select if the data is to be saved. If the “save” button is pressed the VI then implements that state in the state machine code. The VI prompts a user to select a file to save the data to, and then creates a text document documenting all the settings of the instrument (i.e., rotational speed, programmed delay, adjusted time, PD peak height, PD peak time, PMT peak height, PMT time, etc.)

4.3.2.2. P5 Data Channels and example calculation

With the new hardware, the different data collection rates were not an issue as they were with the P4 prototype, therefore only three channels needed to be monitored as compared to seven required for P4. The three channels monitored for the P5 prototype are the photomultiplier (PMT) signal for the primary measurement, the Dye Laser photodiode (PD) and the HeNe PD. The PMT signal monitors the 488 nm light as it leaves the cavity; the values that are used in data reduction are the peak height and timestamp. The dye-laser PD signal records the firing time of the dye laser. This is located on the optics table so the timestamp

corresponds to the time the light enters the cavity. The value used for data reduction is the timestamp with the peak height monitored for troubleshooting. A diagram of typical graphical response as well as a sample calculation is shown in Figure 4-32.

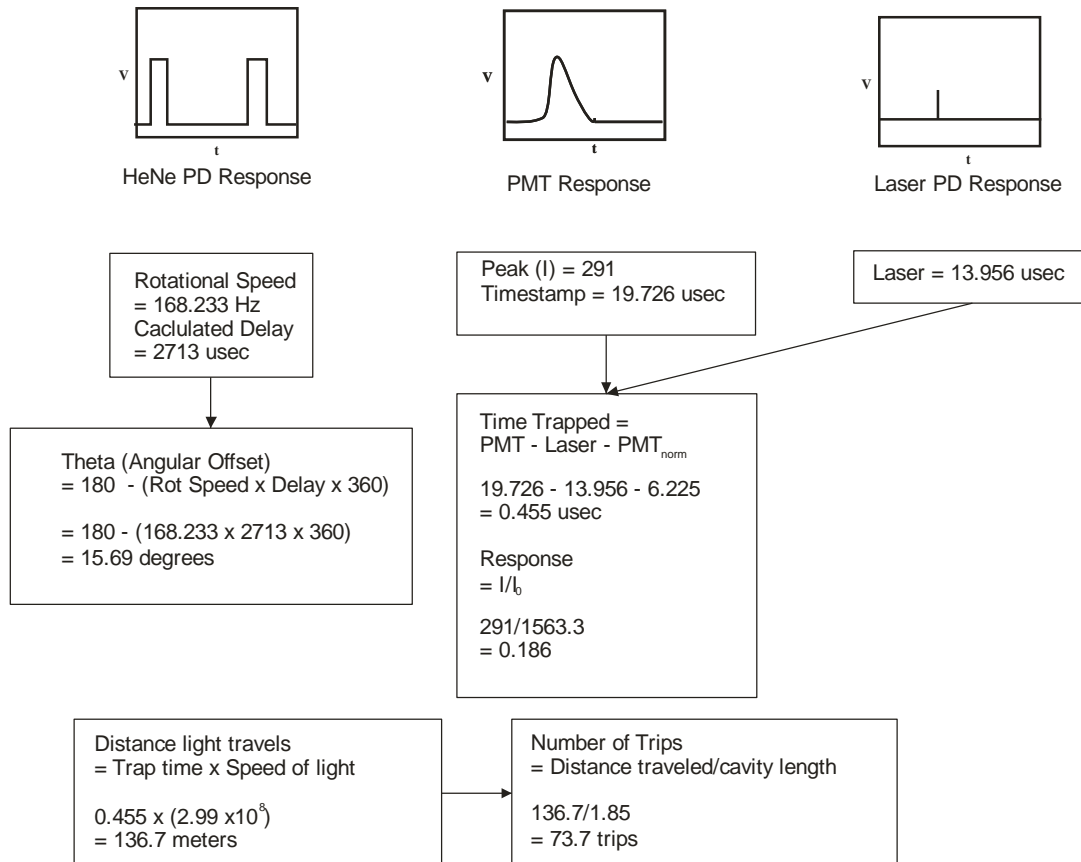


Figure 4-32 Diagram of the three signal responses and an example calculation using the data obtained.

4.3.2.3. Testing Results

4.3.2.3.1. Rotational Speed Monitoring

The purpose of this study was twofold. First to confirm the values obtained through the LabVIEW® calculations matched the values from the previous reduction method, and second to

monitor the stability of the rotational speed of mirror at a set position on the control dial.

Previously the only feedback as to the rotational speed of the axle was a digital display on the motor. This was a whole number represented as 1/1000 of the rotational speed. With the P4 prototype 300 sweeps were averaged before the data was transferred and reduced. The data observed from these averages was not always clear as to what value to use for the rotational speed calculation, this being more predominant at slower rotational speeds, shown in Figure 4-33. The top graph is the data obtained from averaging 300 measurements on the oscilloscope, and it can be seen that the rotational speed has a large amount of variation between each of the measurements since a clean edge is not produced. Table 4-2 illustrates this numerically.

The motor was incrementally monitored (from 1-20 kRPM), 300 sweeps were measured with the oscilloscope, and ten points were collected with the NI hardware. The rotational speed was calculated by locating the leading edge of the first two peaks, subtracting the time difference of the earlier peak from the latter, and the inverse was taken to calculate the rotational speed in Hertz (Hz). The values were also converted to RPM to compare to the display value of the motor. While the average values between the two have a strong correlation, it should be noted the large standard deviation of the ten measurements made with the NI hardware has a sizable standard deviation.

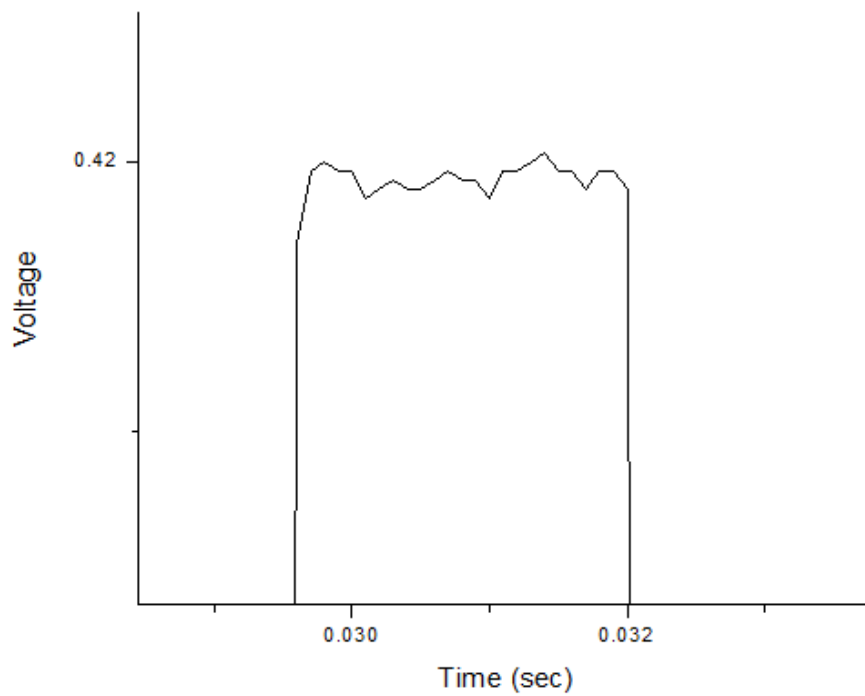
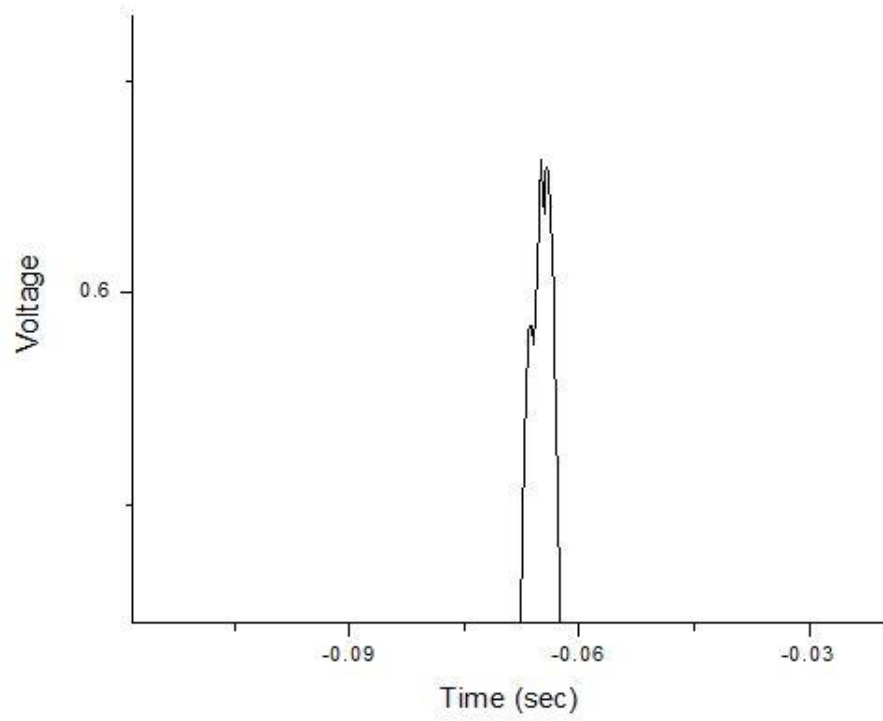


Figure 4-33 Comparison of the data collected by the oscilloscope (top) and NI hardware (bottom). The mirror was set to rotate at 1000 RPM. The oscilloscope averaged 300 sweeps, and the NI data from a single curve of 300 measurements collected by the oscilloscope.

Displayed Rot Speed (kRPM)	Scope		LV			
	RPM	Hz	RPM	Std. Dev.	Hz	Std. Dev.
1	903.1	15.08	902.8	18.27	15.05	0.30
2	1604.3	26.77	1606.2	19.86	26.77	0.33
3	2525.3	42.03	2523.2	13.86	42.05	0.23
4	3623.2	60.76	3614.5	0.00	60.24	0.00
5	4537.2	75.64	4540.7	12.30	75.68	0.21
10	8928.6	148.81	8931.3	19.70	148.85	0.33
15	13477.2	225.02	13507.5	25.46	225.12	0.42
20	18633.5	310.56	18610.5	31.60	310.17	0.53

Table 4-2 The Displayed rotational speed is the value recorded from the digital screen of the motor. The Scope data was the calculated rotational speed from an average of 300 sweeps. The LabVIEW values were collected from a single run, with the rotational speed being calculated for 10 consecutive rotations.

Since the new hardware can be used to control the triggering of the laser, single measurements could be used to get a better representation of the rotational speed. This would allow for the calculation of the rotational speed for the instrument measurement.

4.3.2.3.2. Trapping Calculations

Once the automated data collection was completed, the next phase was to look at the full response curve and characterize the trapping. The first test was to replicate the work previously demonstrated and compare the trapping at various rotational speeds. Figure 4-34 shows a comparison in the trapping at four different rotational speeds (5, 10, 15, and 20 kRPM). Negative angular offsets correspond to the laser triggering before the slit rotates into the beam

path, while the positive angular offsets are when the slit has passed the beam path. In order to compare the data between the rotational speeds, the data has been normalized. The signal was normalized by dividing all the values by the maximum signal observed. The angular offsets were normalized so the highest amount of light transmitted would be a zero degree angular offset. Due to the nature of the alignment process, the beam path is not exactly 180 degrees to the HeNe beam path. Therefore the programmed delay for a single-pass measurement may be shifted by up to five or six degrees. To correct for this, the calculated angular offset value previously determined to be the single-pass measurement is subtracted from all calculated angular offsets at that rotational speed.

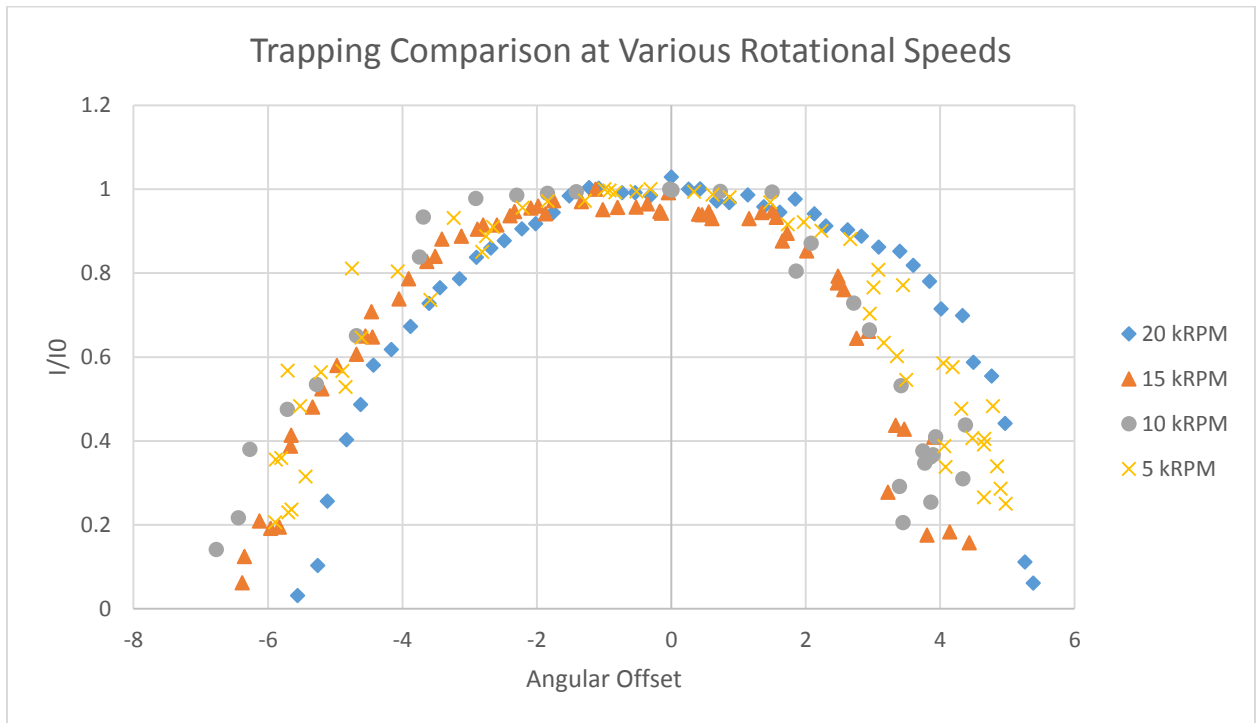


Figure 4-34 Full response curve overlay at 5, 10, 15, and 20 kRPM. The asymmetry on the negative angular offsets indicates trapping is occurring. Each point is an average of 10 measurements recorded at each programmed delay. The angular offset does not take into consideration the jitter in the dye laser firing.

An asymmetry can be seen among the four overlaid graphs. The negative angular offsets have a more gradual slope versus the positive angular offsets, which indicates that more light is present on the negative side. For the positive angular offsets, the decreased linearity of the data is attributed to “jitter” in the laser, due to the amount of light being detected coming from the sliced beam as the slit is passing the beam path, the larger discrepancies in the signal and angular offset are observed.

In order to determine the VI timing was functioning as intended it was to test at long delays. Any issues in the control of the instrument would then come to light by programming longer delays. Longer delays would require the rotational speed monitoring to be accurate, as well as precise calculations for the time delay and triggering the nitrogen laser. This was done by calculating the time delay required for the slit to rotate 180° to the beam path plus an additional 360° of rotation. This means that the system would be armed, the HeNe triggering signal would be detected, and the VI would have to wait a delay time of three times that of the study previously discussed. The results of this are shown in Figure 4-35.

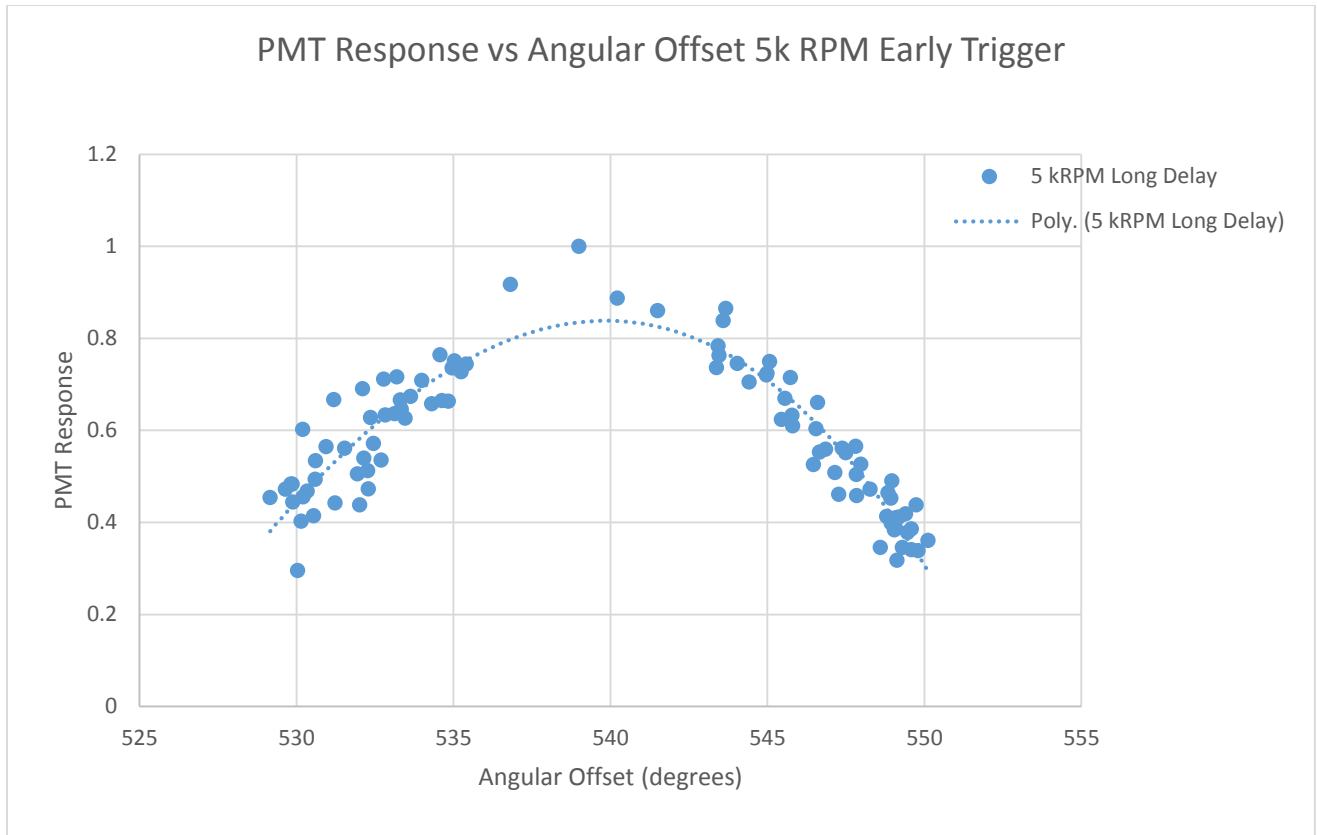


Figure 4-35 Data collected after programming a delay corresponding to an angular offset of 540 degrees, fitted to a third order polynomial to better illustrate the shape of the curve. Each point is an average of 10 measurements at each programmed delay. The angular offset does not take into consideration the jitter in the dye laser firing.

Under closer examination, Figure 4-35 shows that even at delays three times greater than previously demonstrated, the similar asymmetric shape is still observed. The third order polynomial was fit to better illustrate the relationship of the data. The maximum signal is centered around an angular offset of 540°, with a slower decay occurring to the left ($\theta < 540^\circ$) signifying that trapping is occurring. The larger distribution area of the plots is attributed to the fluctuations in the rotational speed over the course of one and a half rotations. As demonstrated earlier there can be large fluctuations observed in the rotational speed. If it was

assumed that the rotational speed would change by 12 RPM, or 0.2 Hz in one rotation, with a programmed delay of 17,500 μ sec or 0.0175 sec, which would result in a shift of 1.2° in the angular offset from the originally calculated angular offset (calculation shown in Equation 4.2 and 4.3).

$$0.2 \text{ Hz} \times 0.0175 \text{ sec} = 0.0035 \text{ rotations} \quad [4.2]$$

$$0.0035 \text{ rotations} \times 360^\circ = 1.3^\circ \text{ shift in angular offset} \quad [4.3]$$

4.3.2.4. Gas-phase Measurements

Gas-phase measurements were made using a calibration tank from Praxair, with a certified concentration of NO₂ in air at 160 ppm. Using a jet, shown in Figure 4-36, NO₂ enters through the bottom of the jet from the calibration tank, across the beam path, and then captured by the funnel which is connected to a vacuum.

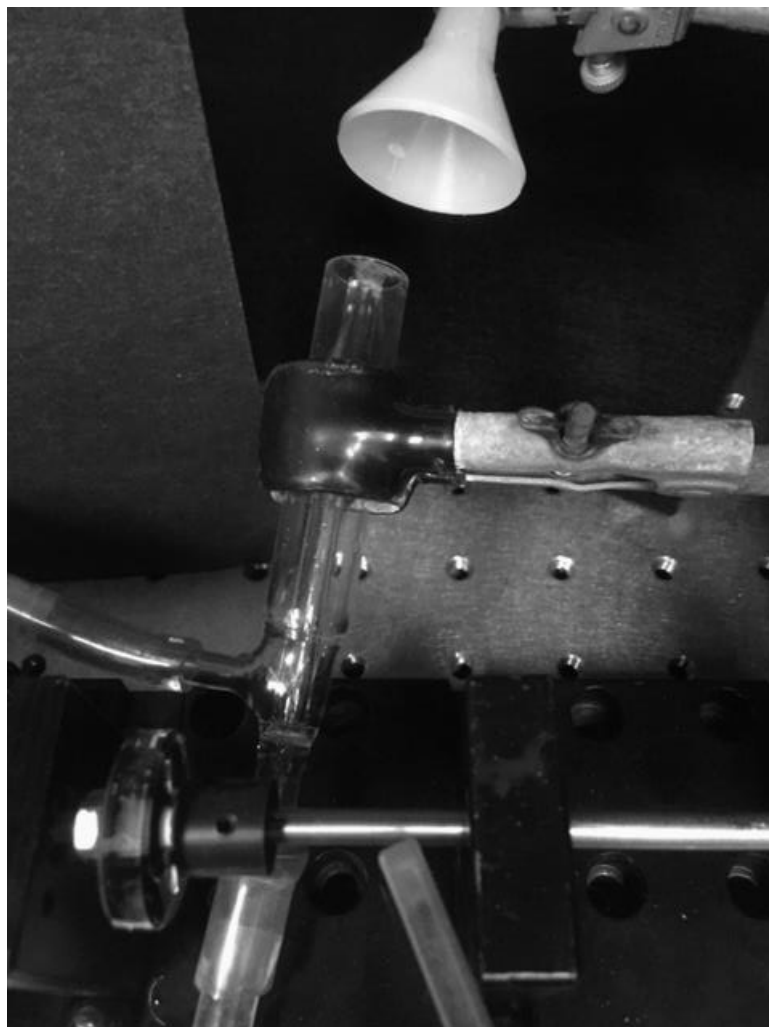


Figure 4-36 Picture of the jet that delivers the NO_2 across the beam path. The NO_2 enters through the back of the jet, while house air is used to prevent the gas from dispersing after leaving the jet nozzle before being collected by the funnel connect to a vacuum line.

Before studying how the response curve at 5 kRPM is affected by the introduction of an absorbing species, the full response was collected first without NO_2 present. The air was still pumped through the outer jacket of the jet and the vacuum was drawing up air to reduce the variability in the two measurements. Figure 4-37 shows the overlaid data comparing the full response curve at 5 kRPM with and without the presence of NO_2 .

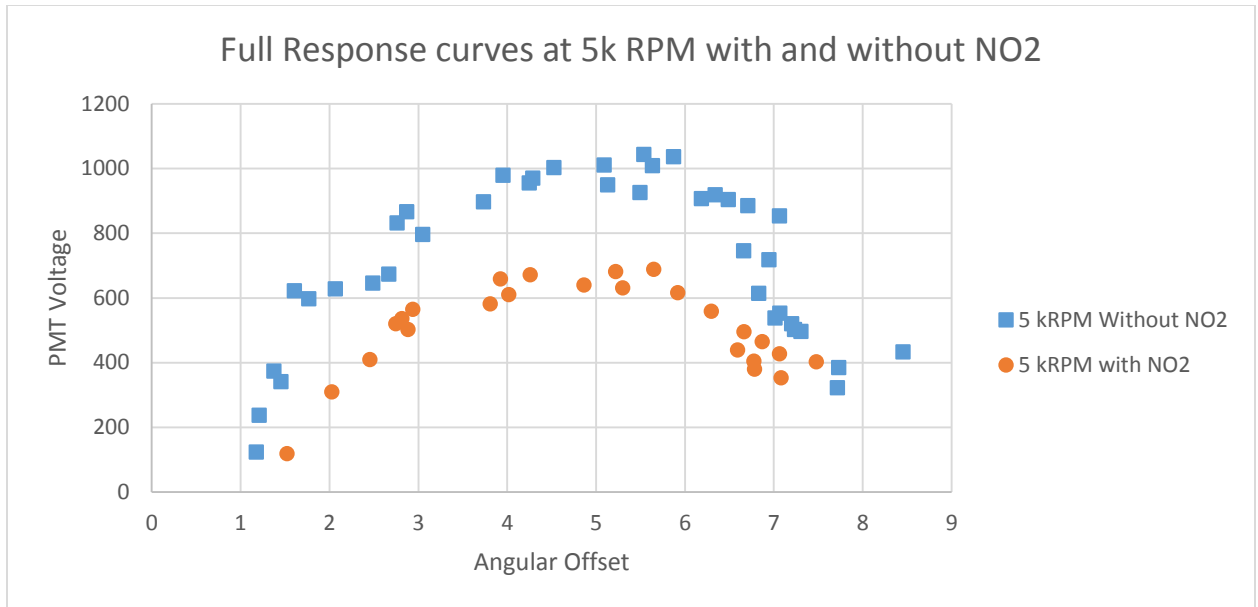


Figure 4-37 The top curve (squares) is the data obtained with no gas present while the lower curve (circles) is with the gas present. The y-axis is the PMT voltage observed for each angular offset, and each point is an average of 10 measurements at the programmed delay. The angular offset does not take into consideration the jitter in the dye laser firing.

The introduction of the 160 ppm_v of NO₂ in air resulted in a reduction in the PMT response on average of 60%. However, whether the NO₂ was present or the cavity was empty, both curves have a calculated maximum number of trips, or enhancement, in the eighties. The empty cavity demonstrated 80 passes through the cavity while when the absorbing species was present the maximum number of trips was 83.

4.3.2.5. Calculation of Cavity Trips

From this data and repeated trials the calculated maximum number of trips the cavity has been measured and these values are displayed in Table 4-3.

Rot. Speed (kRPM)	Max Num Trips
5	83
10	95
15	115
20	127

Table 4-3 Calculated number of maximum trips through the cavity at each rotational speed tested.

The values in Table 4-3 were calculated as follows with example data: first, the difference between the PMT peak timestamp (19.965 μsec) and the Laser PD timestamp (14.392 μsec) was calculated

$$19.965 \mu\text{sec} - 14.392 \mu\text{sec} = 5.5755 \mu\text{sec} \quad [4.4]$$

Originally it was thought that the result of this calculation was the amount of time the light spent trapped in the cavity. After examining data, it was observed that if these values over the full response curve would never approach zero, the values would stay around six microseconds. These values were normalized by locating the point on the response curve with the largest PMT response, corresponding to single pass measurement. The difference in the timestamp for that point is then subtracted from all calculated values.

$$5.5755 \mu\text{sec} - 6.2240 \mu\text{sec} = 0.6485 \mu\text{sec} \text{ trapping time} \quad [4.5]$$

The normalized trapping time is then used to calculate the distance the light travels in that time by first converting to seconds and multiplying by the speed of light in air.

$$0.6485 \mu\text{sec} \times 10^{-6} \text{ sec}/\mu\text{sec} \times 2.997 \times 10^8 \text{ m/sec} = 194.4 \text{ m} \quad [4.6]$$

The distance is then converted to trips in the cavity by dividing the distance traveled by the length of the cavity (1.53 m)

$$193.4 \text{ m} / 1.53 \text{ m} = 127 \text{ trips} \quad [4.7]$$

While the values obtained for number of passes through the cavity are twice that discussed in the work done with P4, the question arises as to why the number of passes are so low for the calculated angular offset. The angular offset that the 127 passes has been calculated to be - 5.5°. The angular offset value is calculated as follows:

$$180 - (\text{Rotation Speed (Hz)} \times \text{Programmed Delay (sec)} \times 360) \quad [4.8]$$

The angular offset is then normalized by subtracting the calculated θ value for the single pass measurement from the calculated angular offsets of each point in the full response. With the new alignment hardware added new optical layouts were tested, and modeling has shown that the addition of a second concave mirror would increase cavity stability. Figure 4-38 is an image from Optics Lab software demonstrating that the introduction of the mirror helps focus the light and reduce the amount of “walk-off”.

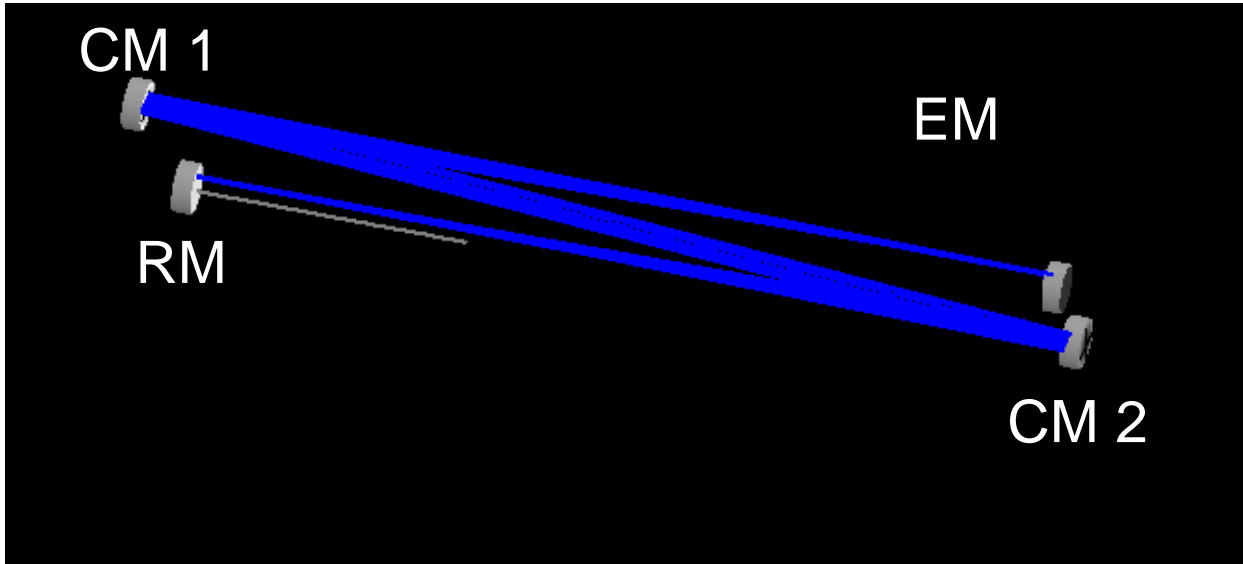


Figure 4-38 Optics lab simulation of the P5 version with the second folding mirror being replaced by a concave mirror. CM 1 (concave mirror 1), EM (entrance mirror), RM (rotating mirror), CM 2 (concave mirror 2)

The optical layout will need to be examined further. The highest reflectivity of the dielectric mirrors is obtained when the incident light strikes the surface of the mirror at 90° . The current optical layout, while may reduce the amount of “walk off” still has limitations that could still be resulting in loss of light. Figure 4-39 shows the angle of incidence of the beam at folding mirrors 1 and 2 are 19° and 21° respectively.

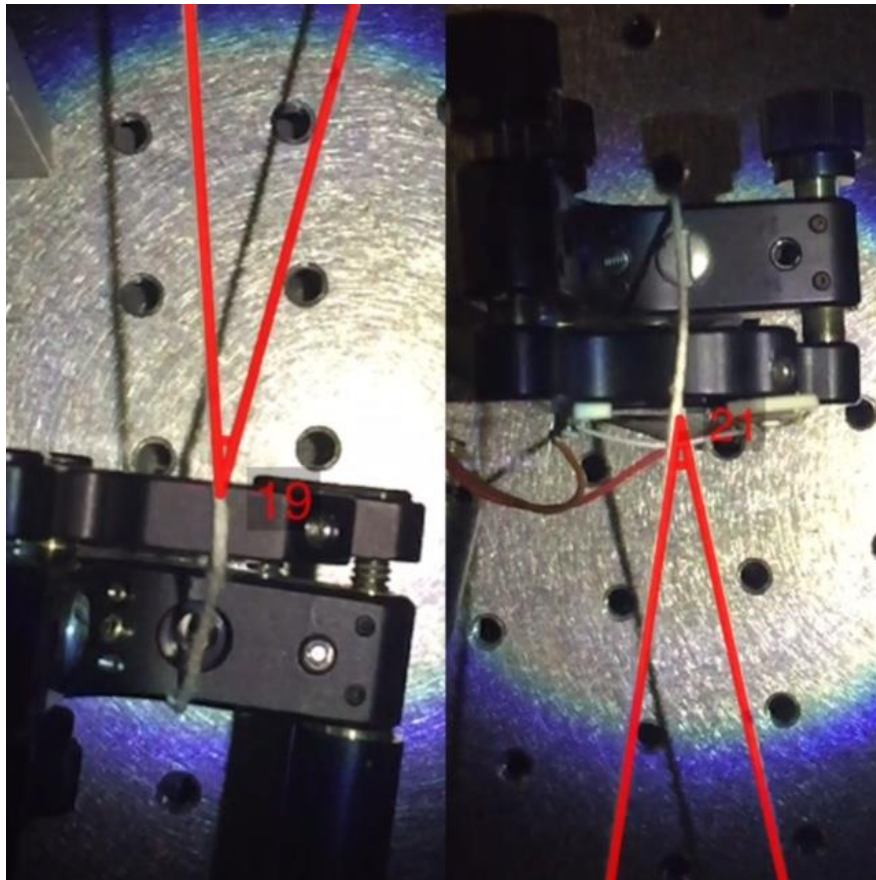


Figure 4-39 Looking at the angle of incidence of folding mirror 1 (left) and folding mirror 2 (right).

Doing basic trigonometry, the layers deposited at $\frac{1}{4}$ thickness of 488 nm, now correspond to a thickness that would have a reflectivity for 516 nm for folding mirror 1 and 523 nm for folding mirror 2.

Figure 4-40 is the data sheet from Los Gatos when the mirrors were purchased.

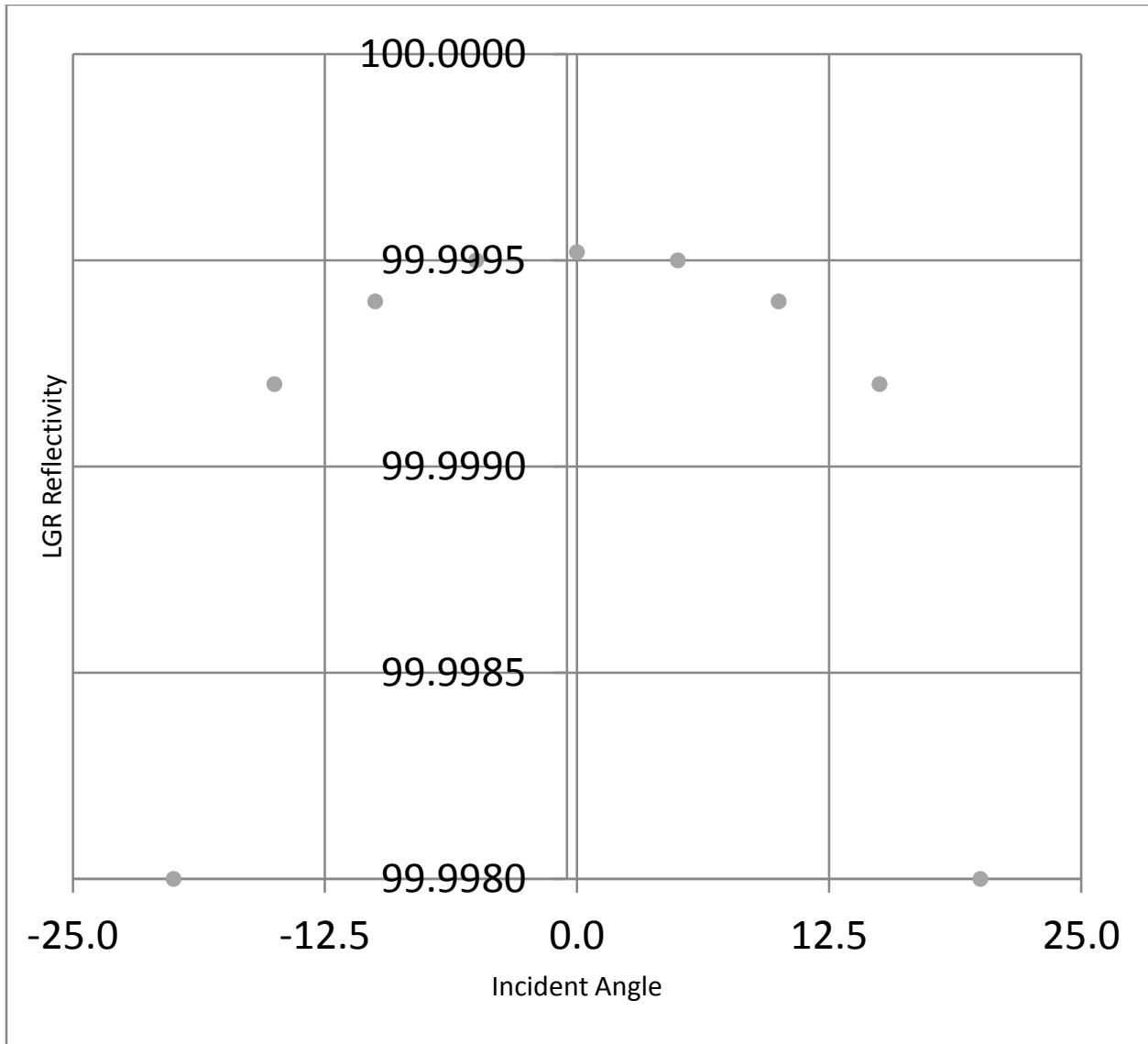


Figure 4-40 Data from LGR showing the relationship between mirror reflectivity and the incident angle of the light. Greater reflectivity corresponds to less light passing through the mirror, resulting in a greater number of theoretical trips through the cavity.

The reflectivity of the mirrors drops from 99.998% to approximately 99.996%, which will have an impact on the number of reflections before the light goes extinct in the cavity.

LITERATURE CITED

1. Frost, J. A. Photon Trapping Spectroscopy: A Novel Extended Pathlength Spectroscopic Technique. University of Wisconsin-Milwaukee, Milwaukee, 2011.
2. National Instruments, PXI: The Industry Standard Platform for Instrumentation. Accessed on March 10, 2014; http://www.ni.com/gate/gb/GB_EVALPXI101EKIT/US
3. National Instruments, FPGA Fundamentals, 2012.

5. Future Work

During the completion of the work, many ideas were considered to improve the VPCS.

Due to the scope of the work, these were not implemented, but are discussed below.

5.1. Alternative VPCS designs

One design of the VPCS was suggested by Dr. Jörg Woehl, simplified the original prototype of the instrument by using one rotating mirror instead of two. As show in Figure 5-1 the entrance and exit mirror of the cavity are one in the same. The light would enter the cavity through the slit on the rotating mirror and then proceed to a delay loop. After entering the cavity the light would then traverse the delay loop constructed by using 2 concave mirrors and flat mirror. The light reflected by the second concave mirror would then travel to the single rotating mirror, instead of a second rotating mirror, striking the mirror 180° to the entrance slit.

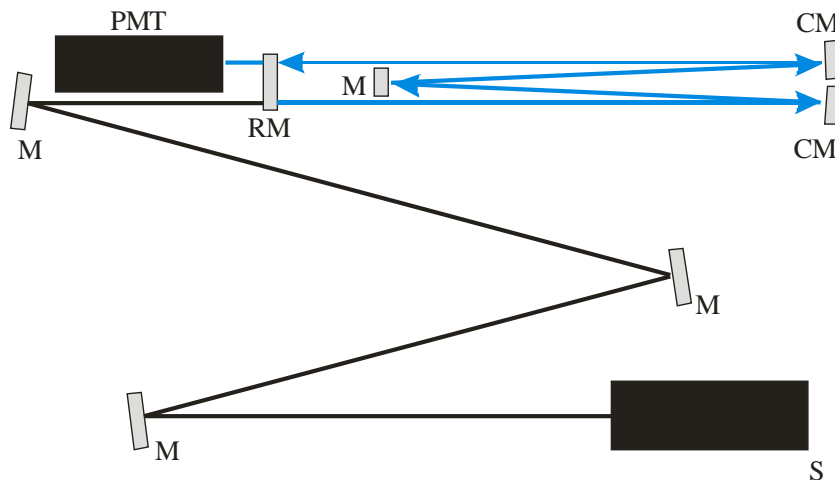


Figure 5-1 VPCS single mirror design. CM (concave mirror), M (flat mirror), RM (rotating mirror), S (source), PMT (photomultiplier tube)

With the beam directed to a different position on the rotating mirror where a slit is not in the beam path at the time of injection, trapping will occur. This technique would have several advantages over the current prototype.

First, the optical layout allows for the optimal angle of incidence for the dielectric mirrors. Due to the construction of the mirrors, the maximum reflectivity is obtained by minimizing the angle of incidence the light is striking the mirrors. By creating an optical layout where the light is striking the surface of the mirror as close to normal as possible, the amount of light reflected at each mirror interaction would be maximized.

The second advantage of this technique is that more light will enter the cavity. With the current P5 version, only a small fraction of the light enters the cavity due to the injection method. While the losses at the mirror interfaces are inherent, the increased amount of light entering the cavity would allow for longer trapping times in the cavity before the amount reaching the detector cannot be measured. This in turn allows for more passes through a sample, creating a larger enhancement factor and lower detection limits.

A third advantage would come from a simplified software implementation to control the instrument. With this technique a CW source can be used. An option for the CW could be a laser diode. This would have advantages onto itself by creating a spatial footprint, lower power efficiency, higher reliability, and increased ruggedness.¹ The implementation of a CW source eliminates the need for the advanced timing required with P5 version to calculate delays for the pulsed laser.

5.2. Hardware Improvements

In order to implement the single mirror design discussed two areas of the instrument hardware would need to be addressed. The first is the mirror slits. This topic was discussed in a previous chapter. The interaction of incident light with the roughly machined edges of the slit in the rotating mirror, as seen in Figure 5-2, caused large amounts of light scatter. .

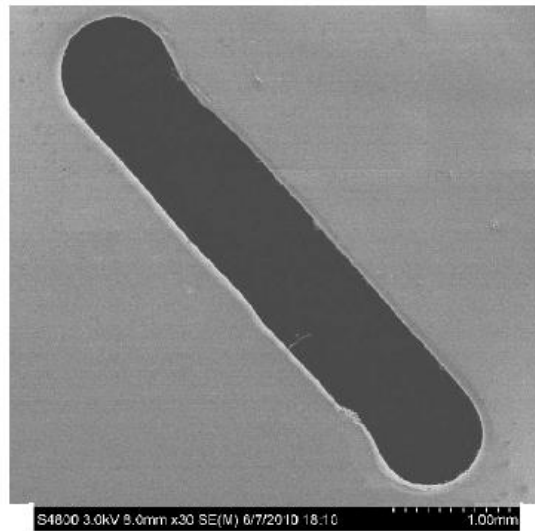


Figure 5-2 Magnified image of a slit in a dielectric mirror (30-fold magnification)

One option method for trying to improve the slit quality would be the use of a masking technique.² The optically transmissive window is created by applying a masking agent or desired shape and size. Once the mask is applied, the substrate then undergoes the process of depositing the dielectric layers. Once the desired number of layers are applied, the mask is then peeled off or chemically removed leaving behind the optical window. One concern with this technique for this application would be the edge that forms and how will that affect the incident light.

A second option for creating mirror slits would involve etching the mirror surface after the dielectric layers have been applied. Etching of the mirrors can be done by two different methods, chemical or focused ion beam methods. While the chemical method would increase the possibility of unwanted damage to the mirror surface, the option of ion beams still have inherent concerns with damaging the mirror surfaces but seem more feasible. A high energy gas ion beam is directed to the portion of the mirror surface that is to be polished or etched. The ions then collide with the surface of the mirror and sputter very small portion off the surface. While this technique is quite useful on nanoscale and for imaging with a tunneling electron microscope (TEM), the amount of surface removed ($\sim\mu\text{m}$ areas) in a single pass and the potential damage to the substrate would need to be thoroughly examined.^{3,4}

A third option to prepare clean slits in the dielectric mirrors is laser ablation, with little to no effect to optically transparent substrates. Work has been done using a pulsed laser. The ablation laser is chosen based on the absorption profiles of the dielectric layers used to construct the mirror. The laser need to emit at a strongly absorbing wavelength of one of the dielectric layers. The non-reflective side of the mirror is then masked to expose the pattern of desired ablation. The work published was able to obtain a clean ablation and remove nearly the whole layer stack (47 total dielectric layers) in one single pulse at 380 mJ/cm^2 with an edge of less than $1 \mu\text{m}$. The result of the ablation can be seen in figure 5-3. This technique produces clean edges and does not deposit debris on to the surface of the mirror.⁵

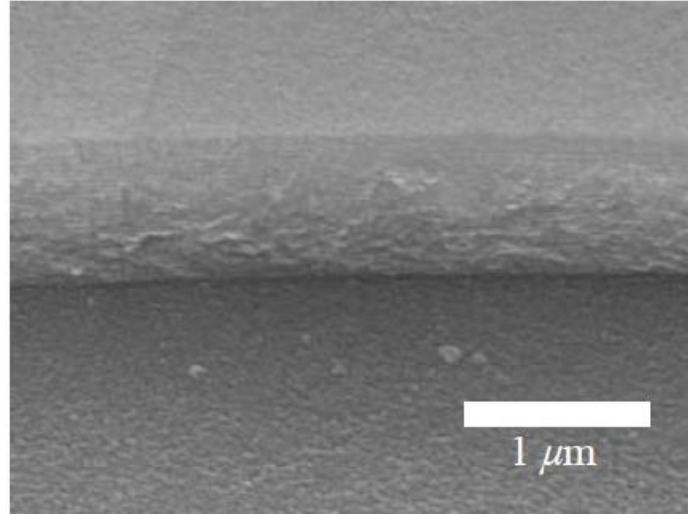


Figure 5-3 SEM micrograph of dielectric mirror following ablation with a single laser pulse. Figure take from Reference 5.

Another required hardware improvement would be in the area of the drive motor. While the current motor has “sweet spots” where the fluctuation in the rotational speed is minimized, greater stability in rotational speed would be required, as well as a larger range of operating speeds. With the single mirror design, the ability to adjust the angular offset is lost. Therefore the only parameter that can affect the trapping time is the rotational speed. To maximize the working range of the VPCS, a motor that can produce a wide range of rotational speed (~60,000 RPM), with minimal fluctuation in the observed rotational speed. This would require research on various drive systems with sufficient power to rotate the axel with a mirror on it, yet have the precise rotational speed selection.

5.3. Liquid-phase Measurements

With the successful demonstration with measuring gas-phase samples the next step would be to move to condensed phases. There are a multitude of ways that CRDS has made the leap from gas-phase to liquid phase-samples. Some of the more widely studied methods include liquid only cavities, fiber loop CRDS, evanescent waves (EW), and specially designed flow cells. Of these, the latter two are candidates for exploring as a possibility for VCPS.

One route for introducing a liquid sample to an optical cavity while minimizing light loss at the interfaces of the sample holder is the use of a Brewster's angle flow cell.⁶ This cell is design to minimize the light loss from scattering at each point there is a change in refractive index. Figure 5-4 shows the cell that was developed for CRDS. One concern with this method is the effect a higher concentrated analyte would have on the refractive index of the mobile phase. CRDS has a narrow working concentration range for measurements, and in that concentration range there are negligible effects of the analyte on the refractive index of the mobile phase. However, with VCPS, the working range is expected to be much larger and the analyte could have an effect on the refractive index of the mobile phase and would cause scattering.

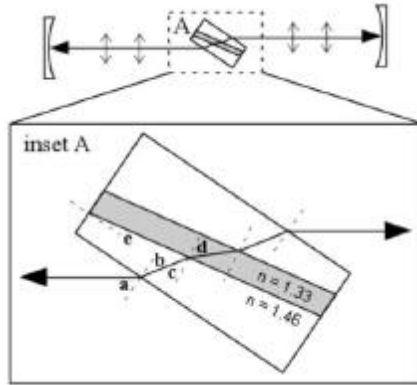


Figure 5-4 Schematic diagram of the Brewster's-angle flow cell. Figure taken from Reference 6.

Evanescent waves, shown in figure 5-5, are the result of the propagation of energy from light that undergoes total internal reflection where the refractive index changes. The energy of the incident light extends beyond the interface that causes total internal reflection and can be used to probe that space. In optical cavities dove prisms have been a common practice to create evanescent waves. The dove prism sides are cut to Brewster's angle to minimize scattering losses. While mobile phase refractive indices would still impact the range the evanescent waves propagate into solution, this technique would not be as confined due to the flow through channel as with the Brewster's angle cell.

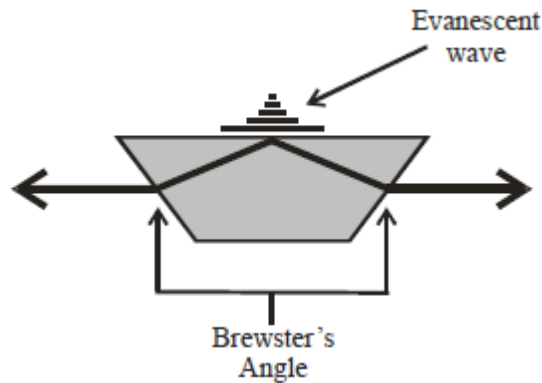


Figure 5-5 Schematic representation of a dove prism. The Evanescent waves propagate out a small distance to probe any sample in contact with the dove prism.

5.4. Potential Applications

VPCS is an incredibly powerful technique that is applicable to UV-VIS-IR ranges. This versatility, as well as the working range of concentrations this instrument is capable of measuring, it opens the door of possibility to problems the VPCS can help address. As shown this is a powerful technique for gas phase measurements. The sample can pass through the beam path at any point within the cavity for a measurement to occur, allowing for versatility in placement and instrument set up. This can be used in exhaust monitoring in labs working with decreasing greenhouse gas production of engine, exhaust monitoring at factories, and even medical applications as CRDS has been used to detect trace gas in human breath, which are markers to various illnesses.⁷

There is a need for the VCPS in condensed-phase measurements as well. Techniques like capillary electrophoresis that have small tube diameters (10 – 100 μm) and other separations techniques like HPLC and UHPLC would greatly benefit from the pathlength

enhancement of the VCPS. An even more defining characteristic for the VCPS that would make this well suited for these separation techniques is the dynamic working range. Samples that undergo these separations can range from concentrations that single pass instruments are capable of detecting to trace analysis. While there are methods that are able to measure those separately, this would be the first inline detector that would be able to cover that concentration range in real time, allowing identification of all analytes in a single run versus multiple runs, saving time and ultimately money.

LITERATURE CITED

1. Skoog, D. A.; Holler, F. J.; Crouch, S. R., In *Principles of Instrumental Analysis*, Sixth ed.; Kiselica, S., Ed. David Harris: Belmont Ca., 2007; pp 188-190.
2. Anderson, T.; Bouzid, A. Process for Forming a Light Beam Path in a Dielectric Mirror. 2011.
3. Dykstra, J. P.; David J. Mount, S.; Skinner, W. J.; Kirkpatrick, A. R. Enhanced etching/smoothing of dielectric surfaces. 1999.
4. Volkert, C. A.; Minor, A. M., Focused Ion Beam Microscopy and Microcaching. *MRS Bulletin* May 2007, 2007, p 10.
5. Schafer, D.; Ihlemann, J.; Marowsky, G.; Herman, P. R., F2-laser ablation patterning of dielectric layers. *Applied Physics A* **2001**, 72 (3), 3.
6. Betchel, K. L.; Zare, R.; Kachanov, A. A.; Sanders, S. S.; Paldus, B. A., Moving Beyond Traditional UV-Vis Absorption Detection: Cavity Ring-Down Spectroscopy for HPLC. *Analytical Chemistry* **2005**, 77 (4), 6.
7. Murtz, M.; Hering, P., Cavity Ring-Down Spectroscopy for Medical Applications. In *Cavity Ring-Down Spectroscopy: Techniques and Applications*, Bergen, G.; Engeln, R., Eds. Blackwell Publishing Ltd.: 2009; p 24.

CURRICULUM VITAE

RYAN A. SCHMELING

Education

Aug 2009- May 2016 University of Wisconsin (Milwaukee, WI)
Candidate for Doctor of Philosophy in Chemistry,
Advisor: Dr. Joseph H. Aldstadt
Major Discipline: Analytical Chemistry
Minor Discipline: Inorganic Chemistry

Aug 2005- May 2009 Troy University (Troy, AL)
Bachelors of Science in Chemistry, 2009

Research Experience

My research experience has been in the areas of analytical and physical chemistry. My primary research projects have included instrument design and method development. I have worked on improving a cavity based laser spectrometer, and applying that to gas-phase samples. I have spent the last three years developing LabVIEW software to fully automate the instrument control, data collection and reduction, as well as alignment. I have also written code for data collection software for a chromatographic system (conductivity and fluorescence detection). I have experience working with LabVIEW Real-Time® as well as LabVIEW Vision. I have taken several training courses through National Instruments including LabVIEW Core 1, 2, and 3; LabVIEW Connectivity; LabVIEW Data Acquisition and Signal Conditioning; LabVIEW Instrument Control; NI FlexRIO; and TestStand 1 and 2.

Honors and Awards

Graduate

2012 SciX Conference (Kansas City, MO) FACCS Student Poster Award
2009-2014 UWM Chancellor's Fellowship

Undergraduate

2005-2009 Chancellor's Scholarship recipient
2005-2009 Troy Athletic Department 3.0 recognition
2005-2009 Sun Belt Conference All-Academic

Leadership

Graduate

2012-2013 President, UWM Student Section, Society for Applied Spectroscopy
2012-2013 Secretary, Triathlon Club at UWM
2011-2012 Vice President, UWM Student Section, Society for Applied Spectroscopy

Undergraduate

2008-2009 President, Chemistry Club, Troy University
2008-2009 President, Student Athlete Advisory Committee, Troy University
2008-2009 Captain, Varsity Track & Field Team, Troy University
2007-2008 Vice-President, Chemistry Club, Troy University
2007-2008 Vice-President, Student Athlete Advisory Committee, Troy University

Poster Presentations

Schmeling, Ryan A, Geissinger, Peter, Aldstadt, Joseph. SciX Conference (Milwaukee, WI.)
“Variable-Pathlength Cavity Spectroscopy: Development of a Real-Time Monitoring System”
(October 2013)

Schmeling, Ryan A, Geissinger, Peter, Aldstadt, Joseph. University of Wisconsin-Milwaukee
Students Awards Day (Milwaukee, WI), "Photon Trapping Spectroscopy: Design, Fabrication,
and Testing of an Automated System of Real-Time Monitoring" poster presentation (May 2013)

Schmeling, Ryan A, Geissinger, Peter, Aldstadt, Joseph. SciX Conference (Kansas City, MO),
"Photon Trapping Spectroscopy: Design, Fabrication, and Testing of an Automated System of
Real-Time Monitoring" poster presentation (October 2012)

Schmeling, Ryan A; Frost, John; Aldstadt, Joseph; Geissinger, Peter. University of Wisconsin-
Milwaukee Students Awards Day (Milwaukee, WI), “Photon Trapping Spectroscopy: Prototype
Design, Optimization and Application” poster presentation (April 2012)

Schmeling, Ryan A; Frost, John; Aldstadt, Joseph; Geissinger, Peter. University of Wisconsin-
Milwaukee Students Awards Day (Milwaukee, WI), “Photon Trapping Spectroscopy: Prototype
Design, Optimization and Application” poster presentation (April 2011)

Schmeling, Ryan A; Frost, John; Aldstadt, Joseph; Geissinger, Peter. Milwaukee ACS Younger
Chemists Committee (Milwaukee, WI), “Photon Trapping Spectroscopy: Prototype Optimization
and Application to air monitoring” poster presentation (April 2010)

Teaching Experience (UWM Dept. of Chemistry & Biochemistry)

2009-2015 Guest Lecturer UWM Dept. of Chemistry
Lectures Given: Reaction Rates to Chemistry for Engineering Students,
Introduction to Spectroscopy, Instrumental Analysis Students

2009-2015 Graduate Teaching Assistant UWM Dept. of Chemistry
& Biochemistry
Courses Taught: Advanced Chemistry Laboratory II, Elementary Quantitative
Analysis, General Chemistry for Engineers, General Chemistry, Preparatory
Chemistry

Additional Education and Training

LabVIEW courses (Core 1-3, Connectivity, FPGA, Real-Time 1 and 2)

Professional Associations

2010-Present American Chemical Society
2010-Present Society for Applied Spectroscopy